Dissertation
submitted to the
Combined Faculties for the Natural Sciences and
for Mathematics
of the Ruperto-Carola University of Heidelberg,
Germany
for the degree of
Doctor of Natural Sciences

Put forward by

Pit Bingen, Master of Science
Born in Luxembourg

Oral examination: July 11, 2012

Parallelised STED nanoscopy

Referees: Prof. Dr. Stefan W. Hell
Prof. Dr. Rainer H. A. Fink

Deen näischt wot, deen näischt wënnt,
deen näischt sicht, deen näischt fënnt.

Abstract

Far-field fluorescence nanoscopy techniques have established themselves as promising tools for molecular biology. These methods are no longer limited by diffraction, and give rise to new challenges and limitations. The use of switching of molecular signalling states makes time-sequential recordings inevitable and leads to increasingly long acquisition times with higher resolution. Parallelisation is essential for reducing the overall acquisition time and enhancing the overall impact of fluorescence nanoscopy on biology. This work discusses the fundamental limits of parallelised coordinate-targeted nanoscopy and demonstrates the first experimental realisation of parallelisation of stimulated emission depletion (STED) nanoscopy. A loss-free fourfold parallelisation is achieved by polarisation-based beam-splitting and chromatic segmented waveplates as beam-shaping devices. A common fibre source offers inherently spatially and temporally aligned laser beams. The time-reducing capabilities of parallelisation are demonstrated.

This work additionally introduces a new detection scheme to targeted nanoscopy, detecting coincident photons per laser cycle on four single photon detectors. Using the quantum phenomenon of photon antibunching, the number of simultaneously excited emitters of an ensemble of molecules can be determined and targeted nanoscopy thus be extended to molecule counting.

Zusammenfassung

Optische Nanoskopie hat sich als wertvolles Instrument für die Molekularbiologe entwickelt. Diese Methoden sind nicht mehr durch die Beugung des Lichtes begrenzt und führen zu neuen Herausforderungen. Das dafür erforderliche Schalten des molekularen Signals macht eine zeitlich sequentielle Signalaufnahme erforderlich und führt zu längeren Aufnahmezeiten mit steigender Auflösung. Um die Gesamtaufnahmezeit des Bildfeldes zu reduzieren und damit die Attraktivität der hochauflösenden optischen Methoden für die Biologie zu erhöhen ist eine Parallelisierung des Bildfeldes essenziell. Diese Arbeit befasst sich mit den fundamentalen Grenzen der parallelisierten Nanoskopie und beinhaltet die erste experimentelle Ausführung von parallelisierter Koordinaten-definierter Nanoskopie mit Fluoreszenzverhinderung durch stimulierte Emission (STED). Eine verlustfreie vierfache Parallelisierung wird durch polarisierende Strahlteiler und ein chromatisches segmentiertes Wellenplättchen, welches als formgestaltendes Element fungiert, ermöglicht. Eine gemeinsame Faserlichtquelle gewährleistet dass alle Laserstrahlen sowohl räumlich als auch zeitlich überlagert sind. Die zeitreduzierende Eigenschaft von Parallelisierung wurde nachgewiesen.

Diese Arbeit führt außerdem eine neue Detektionsmethode in die Nanoskopie ein, welche die koinzidenten Photonen pro Laserzyklus detektiert. Der Effekt des *Photonenantibunching* von fluoreszenten Molekülen ermöglicht es die Anzahl von gleichzeitig angeregten Molekülen aus der Photonenstatistik heraus zu bestimmen. Dies erlaubt es Koordinaten-definierten Nanoskopiemethoden, wie STED, die Anzahl der fluoreszenten Molekülen im Fokus zu zählen.

Contents

List of Figures

Glossary of symbols and acronyms

α	Half-cone aperture angle of the objective lens
$\mathcal{F}$	Fourier transform
$h_{exc}, h_{det}, h_{eff}$	Excitation, detection, or effective point spread function, respectively
I_{max}, I_{sat}	Maximum and saturation switching intensity, respectively
k_{AB}, k_f, k_{STED}	Transition rates between states A and B, of spontaneous fluorescence (f), or stimulated emission (STED), respectively
λ, ν	Wavelength and frequency of light
N	Number of collected photons or number of emitters inside the focal volume
$n_{O,E}$	Refractive index of the medium for ordinary (O) and extraordinary (E) waves
$N_{A,B}$	Occupation probability of states A, B
$P(n; p; i; m)$	Photon probability distribution of detecting i photons emitted by n emitter, for emission probability p and number of detectors m
ρ	Detector or pinhole area
S_0, S_1, T	Ground state, first excited state, and triplet state, respectively
σ	Stimulated emission cross-section
$\tau_f, \tau_{rep}, \tau_{gating}$	Fluorescence lifetime (f), laser repetition rate (rep), and gated time delay, respectively

CCA	Coincidence analysis
FCS	Fluorescence correlation spectroscopy
FOV	Field of View
FWHM	Full width at half maximum
HWP, QWP	Half wave plate and quarter wave plate, respectively

MM	Multifocal microscopy
OTF	Optical transfert function
PAB	Photon antibunching
PnD	Pick & Destroy
PSF	Point spread function
RESOLFT	Reversible saturable optical fluorescence transitions
ROXS	Reducing and oxidising system
(NL-)SIM	(Nonlinear) Structured-illumination microscopy
SLM	Spatial light modulator
SMS	Single molecule switching
S/N	Signal to noise (ratio)
STED	Stimulated Emission Depletion
SWP	Segmented waveplate

1

Introduction

Historical background

Since the beginning, humans were eager to discover what lies beyond the horizon, to understand the unknown and to create tools that help us to achieve new goals. Whether these limits lay in the micro- or macrocosm, they gave the curious minds a reason to doubt them and try to go beyond the previously known. The field of optical microscopy has been continuously developed since the first microscopes at the beginning of the 17th century. Early microscopes led to the creation of the field of microbiology by Antonie van Leeuwenhoek with first observations of individual single-celled organisms [64]. In 1873 Ernst Abbe gave optical microscopy its first theoretical foundation by his description of the resolution limit of a lens [1]. Walther Flemming later pioneered the use of synthetic dyes for staining cells, thereby discovering the cell division process of mitosis [24]. Initially relying on the inherent contrast of cellular features or rather unspecific labelling, the possibilities of microscopy for biological specimens were tremendously enhanced with the introduction of fluorescently labelled antibodies by Coons and Kaplan in the 1940s [15, 16]. Fluorescence microscopy now allowed tagging and discerning of specific cellular components. Ever since, optical microscopy has been continuously improved with development in the field of fluorescent tags, light sources, high-resolution optics and detectors, all aiming at obtaining images with higher temporal and spatial resolution, sensitivity, and specificity. It led to the variety of methods relying on light-matter interactions (multiphoton microscopy, SHG, CARS), new optical arrangements and scanning schemes (phase contrast, DIC, laser scanning confocal microscopy, 4Pi optics), and others [37, 62]. Nevertheless, the diffraction limit, which had been engraved into scientists' minds for over 120 years, had never been questioned and nurtured the study of alternative microscopy methods not relying on far-field optics [10, 20]. Finally, another milestone of fluorescence microscopy made it truly superior to other methods, namely the discovery and development of the green fluorescent protein by Shimomura, Chalfie and Tsien[1] [14, 30, 78]. In 1994, Martin Chalfie first expressed GFP in prokaryotic and eukaryotic cells. This genetically expressed fluorescent protein could now be fused to any given protein, thus enabling the study of living organisms using fluorescence microscopy. At the same time a concept by which the diffraction limit (set by Abbe 120 years before) could be broken, was proposed by Stefan Hell. This ultimately led to the field of super-resolution microscopy or optical nanoscopy [38].

Optical nanoscopy

The field of super-resolution far-field optical microscopy has now been expanding for nearly 20 years and its methodological outcomes have established themselves as promising tools for mainly bio-medical research to gain further insight into molecular processes of living organisms, but also into sub-diffractional manipulation of atoms and molecules using far-field optics. The initial idea proposed in 1994 by Hell and Wichmann was experimentally confirmed in 1999 and ever since the scientific community is looking for the new barrier [38, 48]. Besides the technological aspects the main research focus lies in a better understanding of the interaction between molecules and light, making up the switching of signalling states, which is the basis of optical nanoscopy. Eventually the goal is to define what fundamentally limits spatial and temporal resolution of optical nanoscopy, *i.e.* what information can be extracted and under what (experimental) conditions.

After the first experimental realisation of stimulated emission depletion (STED) nanoscopy, the field of optical nanoscopy has tremendously evolved with different groups worldwide working on approaches of overcoming the diffraction limit by optical switching of fluorescent molecules. Most generally, they can be separated in two groups depending on their switching and readout mode with either a *targeted* or *stochastic* approach [8, 33, 38, 39, 70]. In the targeted approach only molecules residing at specific coordinates, defined with very high precision, are allowed to be in the ON state while all other molecules are actively switched to the OFF state, commonly by a light-driven transition. In the stochastic approach the molecules are switched ON with a very low probability such that a single molecule remains active within a diffraction-limited volume at once. The single molecules are then localised with an accuracy scaling with the square root of the number of collected photons before a next set of molecules

---

[1] Osamu Shimomura, Martin Chalfie and Roger Tsien received the Nobel prize of chemistry in 2008 “for the discovery and development of the green fluorescent protein, GFP”.

is randomly/stochastically activated. Using these methods, resolutions under 6 nm were achieved in nitrogen-vacancy centres in diamond, isotropic three-dimensional resolution of $10-30$ nm was obtained using 4Pi-SMS or isoSTED and video-rate nanoscopy of single synaptic vesicles at 64 nm resolution was achieved [5, 35, 50]. The rapid success of super-resolution microscopy has also led to developments in other field such as photo-induced lithography [23, 54, 77], electron spin manipulation [92], single-particle tracking localisation methods (*e.g.* sptPalm) [58], accompanied with new laser developments in the visible wavelength range [65] .

Photons

It has been shown that diffraction is not hindering microscopy beyond the diffraction limit, but other issues are still unresolved. Due to the particle nature of light, single and mostly uncorrelated photons can be detected when using sensitive detectors. These photons follow a Poissonian distribution with a signal to noise ratio of $\sqrt{N}$, where N is the number of recorded photons. On the other hand the useable excitation laser power is limited by saturation due to the fluorescent lifetime τ_f of fluorophores, *i.e.* one can on average only extract a single photon from a fluorescent molecule in a time interval τ_f. All nanoscopy methods rely on detecting photons, but here is where the two different nanoscopy families strongly diverge: the stochastic single molecule switching (SMS) methods inherently require many photons to increase the optical resolution while the targeted methods do not. Because targeted nanoscopy only permits molecules in a very restricted volume to fluoresce at all, a single photon (above background and detector noise) is theoretically sufficient for identifying if molecules are residing at this coordinate. Collecting more photons is obviously desirable for improving the signal-to-noise and signal-to-background ratios[1].

Recordings processes in optical nanoscopy

The recording processes in all fluorescence far-field nanoscopy methods consists of cyclic alteration between activation, recording and deactivation of subsets of molecules until (ideally) all molecules have been recorded within the field-of-view (FOV)[2].

---

[1] The background signal in SMS is eliminated during the mathematical post-processing process, but a variety of artefacts can arise from the same process, e.g. wrong localisation due to fixed dipole orientation, drift, multiple emitting molecule at distances $< \lambda/2$ [22].

[2] The distribution of this subset of molecules is stochastic in both time and space for SMS, while it is clearly defined (in both time and space) for targeted nanoscopy.

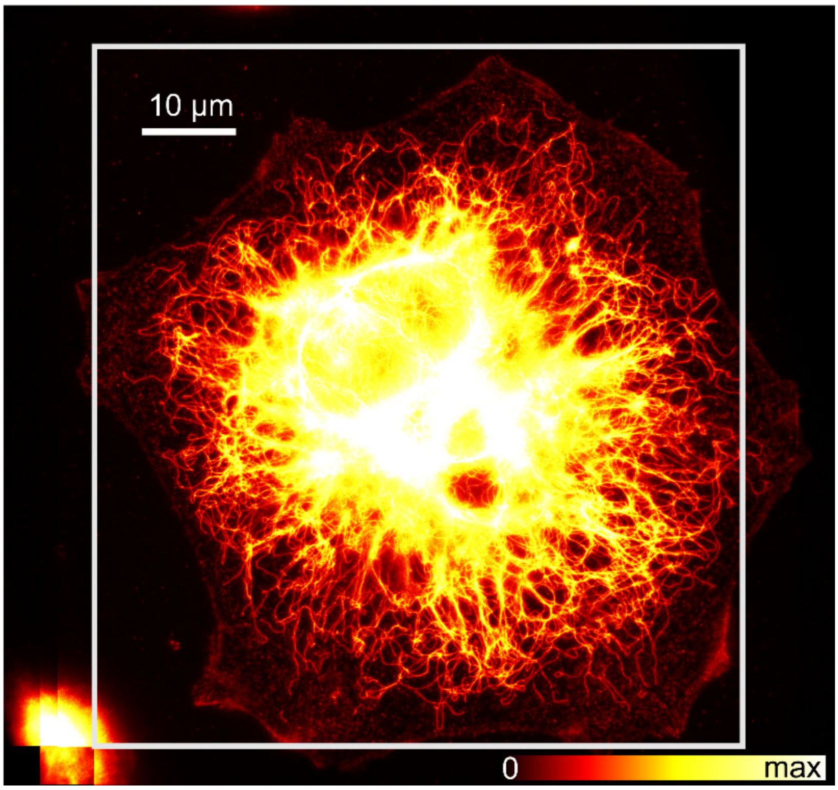

Figure 1.1.: A large scale STED image of KK9445–labelled vimentin in Ptk2 cells recorded with $m = 4$ parallelised and overlaid detection channels at a pixel dwell time of 20 µs, a pixel size of 20 nm, and a FOV of $78.74 \times 78.74\,\mu\text{m}^2$, resulting in an overall acquisition time of 318 seconds. The white square indicates the fully parallelised region, *i.e.* which all four channels have recorded. Accounting for the 17% non-overlapping regions, an effective increase in recording speed of factor 3.32 is obtained with respect to a non-parallelised recording mode, which would require 1056 seconds (17.6 minutes). Note the distinct rhombus-like pattern by which the four channels are displaced in the left bottom corner. The lookup table is saturated for enhancing the signal of the individual vimentin fibres in the outer regions.

In SMS, the resolution linked to the localisation precision, mainly depends on the number of extracted photons per molecule, but higher resolution also requires higher labelling density for recording an image that is adequately representing the underlying structure. This in turn requires a reduced activation probability for guaranteeing single activated molecules inside each diffraction limited volume. All these factors lead to increasingly long recording times for obtaining higher resolution in SMS. Nonetheless, the inherent parallelisation of SMS partially compensates this drawback and has made it a preferred tool for studying large FOVs of fixed biological samples.

In contrast to SMS, the recording process in targeted nanoscopy is deterministic. The overall acquisition time is therefore solely dependent on the switching and fluorescence lifetime timescales. Every collected photon already possesses the sub-diffractional resolution information and a single photon per image pixel is theoretically sufficient for producing an image. This feature has made STED nanoscopy the preferred method for studying fast processes. The switching mechanism in STED nanoscopy is based on the depletion of the fluorescent state by stimulated emission, *i.e.* stimulating photons force the molecule to undergo stimulated emission (OFF) and thereby prevent spontaneous fluorescence (ON). Because the OFF-switching has to occur on a faster timescale than spontaneous fluorescence, STED has initially required high-power laser systems as described in more detail in section 2.3. The development has therefore gone towards slower switching mechanisms for targeted nanoscopy, which require less laser power and should therefore be less phototoxic on living cells[1] [12, 26]. Alternatively, gated CW-STED has enabled similar resolution as pulsed STED with much lower peak power [87]. As a generalisation, all targeted switching methods were regrouped under the acronym RESOLFT (standing for REversible Saturable OpticaL (Fluorescence) Transitions) [33]. STED is the special case of RESOLFT using the switching mechanism of stimulated emission, and both abbreviations will interchangeably be used throughout most of this thesis. Only when comparing the individual switching times and mechanisms, will RESOLFT refer to slower switching mechanisms such as the reversible photo-isomerisation of photoswitchable proteins [26].

---

[1] When talking about phototoxicity and photobleaching, one should carefully distinguish between dye and sample, e.g. STED requires higher powers while slower switching mechanism use very low powers, but often with laser lines in the UV that especially harm living cells.

Parallelisation in optical nanoscopy

Targeted RESOLFT nanoscopy requires a (beam- or stage-)scanning setup for the creation of an image. The acquisition time of single focus beam-scanning RESOLFT thereby scales linearly with each spatial dimension, continuously reducing its advantage of over SMS towards larger field-of-views. Large FOVs can, however, be important for visualising cellular structures in their entirety, *e.g.* the vimentin distribution inside a cell as shown in figure 1.1. Using a single-spot STED microscope the given example would require 17.6 minutes for recording a single frame. Hence, single-spot STED nanoscopy is unable to procure both large FOV and fast acquisition simultaneously, making it inconvenient for live-cell imaging of larger structures. Similar to SMS, RESOLFT allows for parallelisation at larger distances than the diffraction limit ($\sim \lambda/2$), *i.e.* in SMS a second single molecule can be localised at distance $\lambda/2$ whereas in RESOLFT a second modulated switching beam can raster-scan the sample at distance $\lambda/2$. Hence, parallelisation of RESOLFT is ultimately required to obtain both high spatial and temporal resolution in optical nanoscopy. The first experimental realisation of parallelised RESOLFT by STED and a multispot geometry is the focus of this work.

RESOLFT requires complementary light patterns for activating/exciting and silencing of the fluorescent molecules in the ON-OFF switching cycle. One crucial condition in order to implement RESOLFT is a close to perfect zero-intensity at a specific location for the OFF-switching light pattern at which molecules are being excited/activated. Only this zero or *null* ensures that a saturation of the OFF-Switching pattern leaves the remaining molecules at this coordinate in the ON state and thereby enables higher resolution. The most commonly used beam-shaping device for creating this depletion pattern was the helical phase ramp (from 0 to 2π retardation), also known as vortex plate, which creates a doughnut-shaped intensity pattern with a central zero.

Parallelisation of RESOLFT now requires that this OFF-switching pattern is provided for an array of positions in the focal plane, all separated by $\geq \lambda/2$. This can easily be done using polarising beam-splitters, *e.g.* polarising Wollaston or Nomarski prisms, which create two output beams with well-defined splitting angle. The vortex phase plates are, however, not compatible with polarisation based beam-splitting devices without major losses because they critically rely on the correct polarisation of the incident light, *i.e.* fully circularly polarised and the correct handedness of the circular polarisation. Similarly, creating a multispot array based on non-polarisation based beam-splitting (and recombination) could neither be easily implemented without major losses, nor could the power requirements for STED be fulfilled.

Previous work and recent developments

In essence no RESOLFT setup could be thought of that could be both stable and flexible while procuring the same optical properties as a conventional single-spot STED setup even without considering the lack of available laser power. Theoretical work on optimised depletion patterns created using spatial light modulators (SLMs) was done by JAN KELLER. Although providing a flexible way of producing any desired pattern, the feasibility was hindered by theoretical losses of over 85% and the demanding experimental design [46]. As already mentioned, research in the past years strongly focused on the development of dyes, which require less laser intensity. First trials of low-power parallelised RESOLFT and ground state depletion (GSD) by means of striped pattern (often referred to as (nonlinear) structured-illumination, NL-SIM) were performed by SCHWENTKER and others [66,74,75]. They demonstrated 50 nm resolution with the reversible switchable fluorescent proteins (RSFPs) asFP595 and Dronpa, which are still limited to $\sim 10 - 30$ switching cycles before photobleaching. More promising fluorescent proteins are the recently developed rsGFP, allowing for thousands of switching cycles, or Dreiklang, which decouples ON-switching, OFF-switching and excitation of the fluorescence [12, 26]. With these new fluorophores, parallelised RESOLFT microscopy has the potential to become (in the near future) a concept that allows for wide-field, live-cell and three-dimensional super-resolution microscopy. The challenge of producing the desired light patterns together with the limited available laser power or the lack of appropriate RESOLFT dyes have, however, until the work in this thesis, prevented the realisation of true parallelised RESOLFT nanoscopy with comparable resolution and contrast as regular STED nanoscopy. In 2010 REUSS *et al.* developed a novel kind of chromatic beam-shaping device based on polarisation-engineering [68] by which corresponding (single-spot) excitation and depletion pattern can be created using a common beam-shaping device. This so-called easySTED waveplate allows for both laser wavelengths to originate from a single fibre, making the setup inherently more stable than previous solutions. In contrast to the vortex phase plate, the easySTED wave plate produces a central null that is virtually independent of the laser polarisation, allowing for polarising beam-splitters to be used for creating a multispot array. EasySTED paved the way for creating a stable, flexible and low-loss parallelised (multispot) STED setup built in for this thesis.

STED and other fast-switching methods that require strong laser powers will never lose their appeal for fast measurements as discussed in more detail in section 3.1. Regardless of the switching mechanism, however, parallelisation of targeted nanoscopy is essential for reducing the overall acquisition time, and especially important for large FOVs such as illustrated in figure 1.1. The outcomes of this work are therefore important for the further development of the field of optical nanoscopy.

Besides improving resolution and acquisition speed in super-resolution, other difficulties remain equally important for making these methods reliable and useful tools for microbiologists. For obtaining meaningful and reproducible results using optical nanoscopy, biologists require dyes that are resistant to photobleaching, live-cell compatible, bright (for obtaining good S/N ratios), and multiple non-interfering dyes that are optically separable. Last, for the extensive statistical measurements in molecular biology, reliable and stable systems are required that can generate results of comparable quality over long periods of time.

Quantitative measurements in RESOLFT

Despite the increased popularity of high-resolution microscopy, wide-field recordings of fluorescence properties (*e.g.* intensity, spectra, lifetimes, ...) and temporal evolutions thereof have remained popular methods for purely quantitative experiments. They do, however, not resolve the nanoscale distribution of the fluorescent probes. Biosensors that are often based on Förster resonance energy transfer (FRET) or Bimolecular fluorescence complementation (BiFC) can be specially designed to record a large variety of parameters or interactions between molecules [41, 43]. Other quantitative methods, based on fluorescence correlation spectroscopy (FCS), measure the fluctuations in fluorescence intensity of single (or only a few) molecules diffusing through the focal volume. To ensure that only a few molecules are present in the focal volume at once, dilution to nanomolar concentrations is inevitable in diffraction-limited microscopy. The reduced effective volume in STED/RESOLFT nanoscopy can extend FCS to micromolar concentration, required for many biological processes. FCS was successfully adapted to STED nanoscopy in 2005 and recently to TIRF-STED, achieving ever smaller volumes for correlation spectroscopy [45, 53]. FCS and related methods can easily determine quantities such as diffusion, average concentrations and specific brightness distributions. Determining the exact number of single emitters inside a focal volume remains challenging. The local environment of the dye can influence its photophysical properties (*e.g.* fluorescence lifetime, brightness, spectrum, *etc.*)

and make intensity by itself an untrustworthy quantity for counting single molecules.

Counting single molecules

A relatively simple method for counting single fluorescent molecules has been the counting by the stepwise photo-bleaching (BSA: Bleach step analysis), already performed on single GFP molecules [51, 86]. Its destructive and irreversible character, however, make it impractical for many applications in fluorescence microscopy. Another possibility is to exploit the quantum phenomenon of photon antibunching (PAB) for counting fluorescent emitters. This phenomenon was first observed in resonance fluorescence by Kimble *et al.* in 1977, showing that single fluorescence atoms can be identified from their photon distribution exhibiting sub-poissonian statistics when correlating emitted photons in a *Hanbury-Brown-Twiss* like experiment [29, 47, 57]. Photon antibunching of single fluorescent molecules was later observed in solids [7] and on surfaces [2]. Lounis and Moerner then used this effect with pulsed excitation to confirm that detected photons originate from a single emitter by counting the coincident photons on two detectors [55]. Finally the group of Markus Sauer adapted this idea for counting the number of independent emitters in the focal volume [85, 89]. The contrast of the antibunching dip saturates quickly with larger number of emitters so that a two detector setup can in practice only count up to 3 molecules [31]. Ta *et al.* first theoretically outlined the advantages of a four detector arrangement for counting more single emitters [84] and later confirmed this experimentally by counting up to 15 Atto647N fluorophores conjugated to DNA constructs [83]. Nevertheless, even four detectors only allow counting by coincidence analysis (CCA) up to a limited number of fluorophores before saturation. Similarly to STED-FCS, STED-CCA has the potential of extending the counting of single emitters to ever higher concentrations. From a different perspective, STED can actively control the number of molecules inside the effective fluorescent volume and thus eliminate the dependence on low molecular concentrations for CCA.

Coincidence analysis is adapted to STED in this work. Unlike optical setups using one or two detectors, CCA with four detectors offers a quantitative solution for counting ensembles of molecules ($N > 3$) at the nanoscale for RESOLFT nanoscopy[1].

---

[1] CCA will refer to a four detectors optical setup throughout this work.

2

Theory

This chapter is intended to first give an introduction to fluorescence microscopy and how the use of optical switches can break the diffraction barrier by RESOLFT nanoscopy. An accurate mathematical description is given of focusing light at high numerical aperture objectives, important for explaining the challenging beam-shaping task in parallelised (multifocal) microscopy (Section 5.3). The temporal information of fluorescent photons is discussed and how it can provide additional information about the emitting molecules. Finally the concept of coincidence analysis is explained, which is used in this work to provide a quantitative detection scheme for counting emitters in RESOLFT nanoscopy.

2.1 Fluorescence

Fluorescence is the ability of a molecule to absorb a photon of a specific wavelength and (most commonly) reemit one with a lower energy or in wavelength terms one of a red-shifted wavelength. The energy is hereby largely lost to the environment by vibrational relaxation, *i.e.* heat, and the difference between maximal absorption and emission wavelength is known as Stokes shift. By carefully separating the fluorescence from scattered or reflected excitation light, one can reproduce the distribution of the fluorescent molecules using an imaging system. The molecular states of a typical fluorescent molecule can be described semi-classically using the Jablonski diagram (see Fig. 2.1). A molecule residing in its ground state S_0 is excited instantaneously by a photon of energy $E = h\nu$, with Plank constant h and frequency ν, into an excited S_1 state whose energy gap to the ground state matches the energy of the absorbed photon. From this state it relaxes (within < picosecond) to the lowest S_1 state. The molecule then typically decays back into the S_0 state by spontaneous decay emitting a (fluorescent) photon after a fluorescence lifetime τ_f (on the order of nanoseconds). Besides fluorescence, any other molecular transitions that allows for a measurable interaction between matter and light

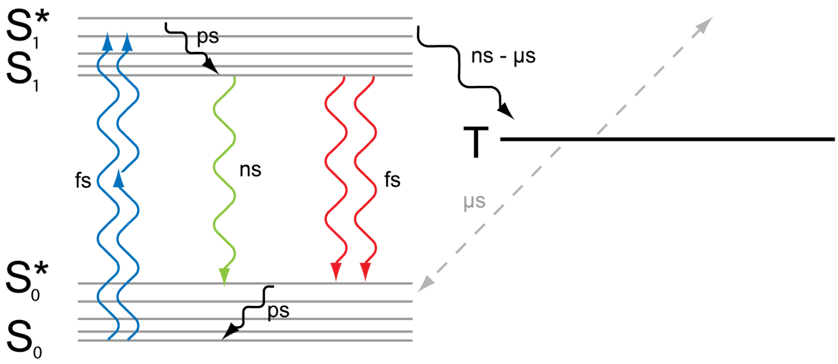

Figure 2.1.: Jablonski diagram describing semi-classically the processes present in a fluorescent molecule and their respective time scales. A fluorescent molecule is excited by one- or multi-photon absorption (blue arrows) to an excited S_1^* state and relaxed vibrationally to S_1 from which all further transitions occur. This property is known as Kasha's rule. From here it can cross non-radiatively to the spin-forbidden triplet state T, fluoresce by spontaneous emission (green arrows) or undergo stimulated emission by emitting a photon of identical frequency and phase of the stimulating photon (red arrows). After fluorescence or stimulated emission the molecule relaxes back into the lowest S_0 state. T is often involved in photobleaching processes but can also act as an optical switch due to its long lifetime.

enables optical microscopy, *e.g.* multi-photon processes or scattering (involving virtual energy states). Molecular transitions can be either spontaneous, as in the case of (spontaneous) fluorescence, or be light-driven, as the competing stimulated emission. The different time scales and competition between light-driven and spontaneous processes enable the creation of so-called optical switches, essential for breaking the diffraction limit.

2.2 Image formation

The goal of microscopy is to form an image from an object by means of an optical imaging system. The image is a visual representation of an original object made with a detector depicting a certain feature, *e.g.* a photograph collecting the visible light reflected or emitted by an object, focused onto a colour-sensitive CCD chip. An imaging system can, however, never fully replicate the original distribution of an object of atomic scale due to the wave nature of light. In simple terms one can think of light interfering on the scale of the wavelength of light and thus not being able to assemble to much smaller distributions due to interference or diffraction. Ernst Abbe first described the diffraction limit for far-field microscopes in 1873. He essentially derived that light emitted from a point source can only be focused down to a volume of lateral and axial full width at half maximum (FWHM) [1, 11]

$$d_{x,y} = \frac{\lambda}{2n\sin(\alpha)}, \tag{2.1a}$$

$$d_z = \frac{\lambda}{2n\sin(\alpha/2)^2}, \tag{2.1b}$$

where λ is the wavelength of light, n the refractive index of the medium, and α the half-cone opening angle. The product $n\sin\alpha$ is known as the numerical aperture of a lens, NA and can reach up to 1.51 for high numerical aperture objective lenses with oil immersion.

In the Fourier optics description of a linear imaging systems [72] (App. B), the response of the system can be described either by the impulse transfer function (or point spread function) or by its transfer function. The point spread function (PSF) describes how the signal from an impulse or point source is transmitted from object to image plane while the optical transfer function (OTF) describes the transmission of spatial harmonic functions. PSF and OTF are related by Fourier transforms and are both valuable descriptions of an optical system. The PSF $h_{det}(r)$ of a focused imaging system with a circular aperture is given by the distinct Airy pattern with dimensions given by equations 2.1. The corresponding OTF is limiting the transmitted spatial frequencies to frequencies below the spectral bandwidth of the imaging system. Because the transfer function of free space tends to zero for spatial frequencies above the cutoff frequency $1/\lambda$, the spectral bandwidth can never exceed this frequency in far-field microscopy and features smaller than the wavelength will not be transmitted, *i.e.* free space acts as a low-pass filter at distances larger than the wavelength of light. Near-field optical microscopy methods have therefore emerged, such as NSOM/SNOM and superlenses using metamaterials, where spatial frequencies above the free space cut-off frequencies are sufficiently sustained at very small distances [20, 63, 97]. Alternatively electron microscopy, where electrons of mass m_e are accelerate to kinetic energies E_e in order to reduce their De Broglie wavelength $\lambda_e = 19.65\,\mathrm{nm}\,/\sqrt{m_e E_e(\mathrm{eV})}$, was developed and has achieved resolutions down to the single-digit nanometre range [94]. For far-field fluorescence microscopy, which has tremendous advantages over scanning probe techniques for biological studies of intact cells, Abbe's diffraction limit is still a constraint for imaging at the molecular level.

In order to improve the lateral resolution and optical sectioning depth, excitation of the object can be performed with a point-like excitation also governed by diffraction. The distribution by which the specimen is excited, called excitation point-spread function h_{exc}, is likewise given by a distribution governed by equations 2.1, which is the closest distribution to a point-like distribution to which a laser beam can be focused down to. Combining point-like excitation and detection is the concept of confocal microscopy because both excitation and detection PSFs are covering the same (con-)focal volume. A pinhole thereby assures that only light originating from the excitation volume is collected and out-of-focus signal discarded. As a compromise between signal and resolution a pinhole size with diameter equal to the airy disc (of the detection PSF) is usually chosen. The combined three-dimensional sectioning strength of a (confocal) microscope can then be described by the effective PSF

$$h_{eff}(r) = h_{exc}(r) \cdot (h_{det}(r) \otimes \rho(r)) \tag{2.2}$$

where $\rho(r)$ is the detector area located in the conjugated image plane. Equation 2.2 is now valid for all imaging systems. In a parallelised imaging system the effective detection point-spread function $h_{det}(r) \otimes \rho(r)$ is crucial for avoiding cross-talk between parallelised channels, *e.g.* when h_{exc} of beam #1 and $h_{det}(r) \otimes \rho(r)$ of pinhole #2 are overlapping. In a wide-field microsope $\rho(r)$ is the pixel size of the CCD camera[1]. Since h_{exc} is constant across all spatial dimensions, resolution and sectioning depth depend on the effective detection PSF $h_{det} \otimes \rho(r)$. To summarise, in order to increase the resolution of an imaging system one has to reduce the size of the effective point spread function. While the detection PSF cannot be altered because it represents the extension of the photon flux emitted by a single emitter, the key to breaking the diffraction limit in RESOLFT nanoscopy is to control which molecules are allowed to emit by controlling their molecular states and thus the effective excitation PSF. The next section will discuss on how switching leads to breaking of the diffraction barrier.

2.3 STED and RESOLFT-type nanoscopy

RESOLFT-type microscopes break the diffraction limit by forcing (fluorescent) molecules into two distinct states, depending on their coordinate in the object plane. One state is thereby confined to $< \lambda/2$ dimensions around a zero light intensity position. Molecules residing in this signalling (fluorescent) state can therefore be separated from the remaining ones

---

[1] The optimal detector size can be derived from the Nyquist sampling criterion

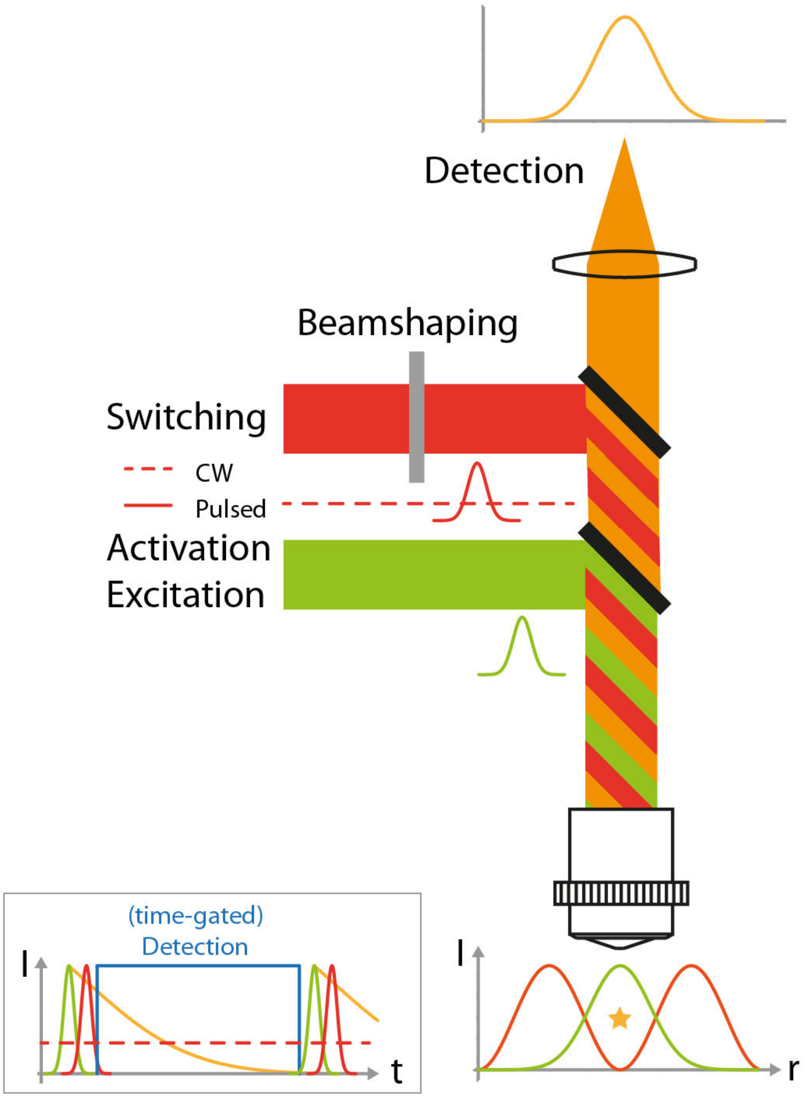

Figure 2.2.: A typical optical setup required for RESOLFT nanoscopy: Excitation (and activation) wavelengths turn the fluorescent dye into an emitting state. The switching wavelengths, responsible for silencing the peripheral molecules are modulated by a beam-shaping device such that fluorescence is only allowed from a well-defined zero intensity position. The dye (orange star) residing at this zero intensity position emits fluorescence which is collected by the objective lens and imaged onto a detector. Both illumination and detection of a single emitting molecule are limited by diffraction. All laser beams can be used in either pulsed or continuous wave (CW) modes for RESOLFT. Depending on the switching mechanism an additional activation wavelength might be necessary. When using pulsed lasers for excitation and switching, switching is quasi-instantaneous and all detected photons should contain the same super-resolution information. For CW switching, the process is dynamical and resolution can be increased by time-gating the detection with respect to the excitation pulse. CW for both excitation (not shown) and switching is feasible but offers no possibility of increasing the resolution by time-gating.

and are confined to a sub-diffractional volume, *i.e.* the effective excitation point-spread-function. By scanning the illumination field(s) over the sample, an image of the molecular distribution can be reconstructed, similarly to other scanning microscopes. A typical setup is based on a confocal laser scanning microscope as illustrated in figure 2.2. Please note again that a confocal setup is not a requirement for RESOLFT. The typical setup includes an point-like illumination for activating and exciting the central molecules, a modulated beam for depleting the peripheral molecules and appropriate filters for decoupling the fluorescence from the remaining wavelengths[1]. Different laser operation and timing modes (pulsed/CW) are illustrated for completeness in the same figure and will be described in more detail in section 2.5. But how can optical transitions produce switches of molecular states that will eventually lead to the breaking of the diffraction barrier?

Let's consider a fluorescent molecule with two distinct states A and B and a transition from A to B that can be optically driven at a rate $k_{AB} = \sigma I$, where σ is the cross-section and I the intensity ($^{\mathrm{Photons}}/_{\mathrm{Area} \cdot h\nu}$). Additionally consider a reverse transition k_{BA} independent of I. The kinetics of state A can hence be described by $\mathrm{d}N_A/\mathrm{d}t = k_{BA}N_B - k_{AB}N_A$. After a time $t \gg 1/(k_{AB} + k_{BA})$ the system has settled with an occupation of state A of $N_A^{\infty} = k_{BA}/(k_{AB} + k_{BA})$. In the case of I being equal to the saturation intensity $I_{sat} = {}^{k_{BA}}/_{\sigma}$ (or $k_{BA} = k_{AB}$), states A and B are both occupied with a probability of 50%. For intensities of $I \ll I_{sat}$ or $I \gg I_{sat}$, N_A tends to 1 or 0 respectively. This saturable transition can thus be considered an optical switch. The most simple saturable transition is the depopulation of the ground state because excitation from the S_0 to the S_1 is instantaneous, and the reverse transition evolving with the fluorescent lifetime τ_f. This saturation effect can be utilised directly, involving extensive post-processing (SSIM, SPEM) [28,32], or indirectly by shelving the molecules into a long-lived dark state (*e.g.* triplet) which in turn increases the probability of irreversible photobleaching (GSD) [34].

The first molecular transition successfully used for RESOLFT microscopy was stimulated emission by which the excited state is immediately depopulated after excitation by a second beam, stimulating the molecule to emitting a second photon of identical properties, *i.e.* wavelength, polarisation and phase. This depletion mechanism is the base of stimulated emission depletion or STED nanoscopy. The stimulated emission rate k_{STED} competes with spontaneous (fluorescent) emission. At high enough intensities k_{STED} exceeds the spontaneous transition k_f and acts as optical switch. This can be reexpressed as $k_{STED} = {}^{\sigma I}/_{h\nu} \gg k_f = 1/\tau_f$ and thus

---

[1] Activation and excitation are essentially the same in STED nanoscopy but can be decoupled in other RESOLFT methods.

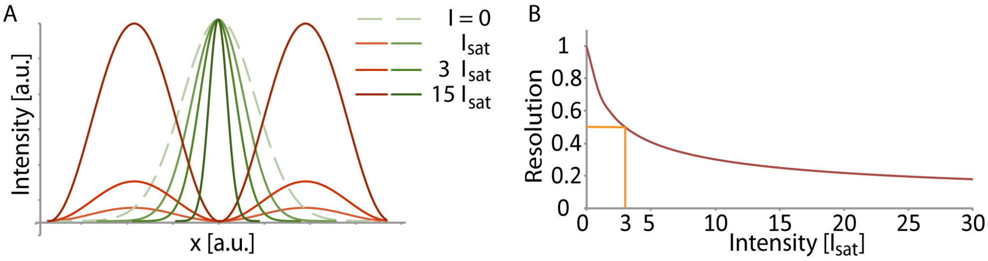

Figure 2.3.: Resolution increase in RESOLFT nanoscopy illustrated for different switching intensities. (A) The effective excitation PSF (green) as given by equation 2.3 for intensities of the modulated switching beam (red) $I=I_{sat}$, $3I_{sat}$ and $15I_{sat}$, resulting in a $\sqrt{2}$−, 2− and 4−fold increase in resolution with respect to the diffraction-limited resolution (I=0). (B) FWHM of the effective excitation PSF against the switching intensity I.

$I_{sat} = {}^{1}\!/_{\sigma\tau_f}$, where σ is the stimulated emission cross-section. The wavelength of the stimulating beam is carefully chosen as not to interfere with the main fluorescence detection band. It is most commonly located in the far-red tail of the emission and thereby allows for spectral separation of the two states. A temporal distinction, *e.g.* by time gating, can further improve the contrast between the states as will be discussed further in section 2.5.

2.3.1 Resolution

An optical switch can be used to reduce the effective point-spread function to a sub-diffractional volume by carefully shaping the stimulated emission beam into a pattern with one or multiple zero intensity positions that confine fluorescence to the regions around these nulls. By increasing the power of the STED beam the depletion pattern is saturated and positions progressively closer to the zero intensity positions exceed the threshold intensity I_{sat} as illustrated in figure 2.3. For short pulses the probability of remaining in the excited state after the STED pulse is approximately $e^{-I/I_{sat}}$. To include this depopulating term as well as the interactions between dipole orientations of the fluorescent probes and the individual excitation and depletion fields equation 2.2 needs be modified for deriving the effective fluorescent volume h_{STED} [46]. For the most simple depletion pattern, a 1D standing wave $I(x) = \cos^2(2\pi nx/\lambda)$, Hell *et al.* derived a modified Abbe formula for the new diffraction-unlimited resolution of a

RESOLFT-type microscope [90],

$$d_{x,y} = \frac{\lambda}{2n\sin(\alpha)\sqrt{1 + I_{max}/I_{sat}}}, \tag{2.3}$$

where I_{max} is the maximum intensity of the doughnut-shaped STED beam in the focal plane surrounding a diffraction limited spot[1]. A close to perfect zero intensity is crucial for achieving high resolutions because saturation of the depletion pattern will eventually silence any molecules residing at a position with remaining STED field. Due to the high numerical aperture of modern objective lenses, it is important to apply a vectorial theory of light when calculating the best depletion patterns for RESOLFT. One should neither forget that most fixed fluorophores have a dipole moment and thereby a preferred orientation of being excited and depleted. The next chapter will elaborate on the mathematical theory of focusing light at high numerical apertures, which will be used in the further course of this work for calculating the limiting parameters of parallelised easySTED / easyRESOLFT nanoscopy.

2.4 Mathematical theory of focusing light at high numerical apertures

As described in the previous section targeted switching and readout nanoscopy critically relies on beam-shaping for obtaining a resolution beyond the diffraction limit. For this purpose a mathematical model is here described and used to compute the focal field distribution for arbitrary input field.

It is well-known that under certain conditions the electric field distribution in the focal plane can be directly described by the Fourier transform of the corresponding Fourier plane or backfocal plane. The action of a lens can be explained by the focusing of a plane wave onto the focal plane. Depending on the angle of incident (spatial frequency), each plane wave is focused onto a different position $x = \tan\theta \cdot f$ on the output screen similar to a grating with a distinct angle of constructive interference set by the grating frequency.

When focusing light with high numerical aperture objectives, however, this rough approximation is insufficient. The Debye integrals give a more accurate solution for calculating the light distribution near the focal region in case of the Debye approximations. It approximates the lensing action by the projection of the incident plane wave onto a spherical cap

---

[1] I_{sat} actually accounts for additional factors such as the shape of the depletion pattern or the molecular orientation and therefore deviates from $^1/_{\sigma\tau_f}$

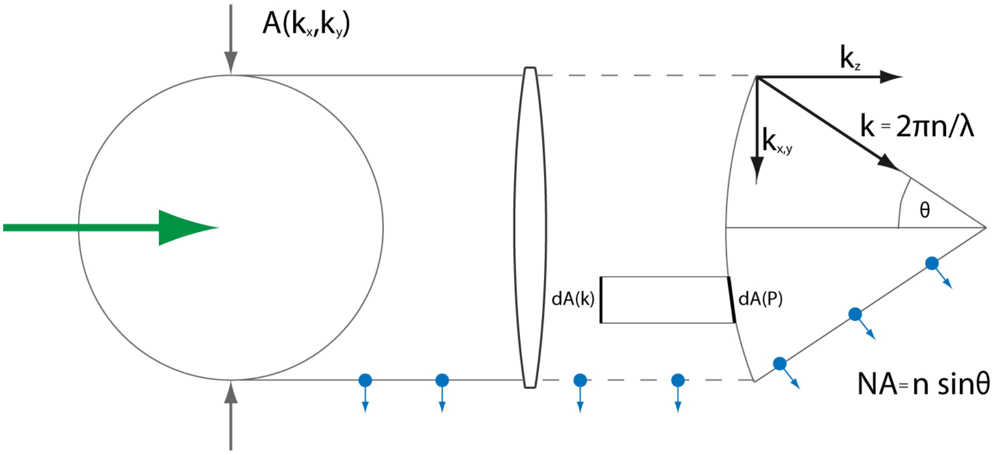

Figure 2.4.: The complex wavefront at the pupil plane A(k) is focused by the objective lens. This action can mathematically be as the projection of the plane wave onto a spherical cap centred around the geometrical focus. The focal field distribution is well approximated by the superposition of plane waves of wavevector $k_{x,y}$ with complex amplitude $A(k_x,k_y)$. Wavevectors larger than $k = 2\pi n/\lambda$ can not be transmitted because they represent evanescent waves. For energy conservation an apodisation factor is required for converting $A(k_x,k_y)$ to A(P). High numerical aperture (NA) objective lenses also need to include the deflection of the polarisation vector (blue arrows) upon focusing. This depolarisation is most pronounced at large focusing angles.

centred on the geometrical focus. Wolf and Li further discussed that for $kf \gg \pi/\sin^2(\alpha)$, aperture $a \gg \lambda$, and $\alpha < 30°$, this approximation is in good agreement with the actual field distribution [95]. For higher numerical apertures, however, depolarisation and apodisation effects have to be taken into account. This is described in more detail by Gu [27].

The Debye integral states that the focal field at position r from the focal origin is

$$E(r) = \frac{i}{\lambda}\int A(P)e^{ikr}\mathrm{d}\Omega \tag{2.4}$$

where λ is the wavelength of light, $A(P)$ the complex aperture at point P on the spherical wavefront and Ω the solid angle of the wavefront. The spherical focal sphere is described by $k_x^2 + k_y^2 + k_z^2 = k^2$ and k_z therefore given by $k_z(k_x,k_y) = \sqrt{k^2 - k_x^2 - k_y^2}$. The variable of integration $\mathrm{d}\Omega$ can then be reexpressed in terms of k_x and k_y, as $\mathrm{d}\Omega = (\mathrm{d}k_x\mathrm{d}k_y)\cdot(k/k_z)$ with

$k_z = \cos\theta \cdot k$ and $\theta = \arcsin\left(\sqrt{(k_x^2 + k_y^2)/k}\right)$. Additionally for a lens obeying Abbe's sine condition, $A(P)$ can be related to the complex pupil function $A(k)$ located before the objective lens by $A(P) = A(k)\sqrt{\cos\theta}$ [27]. Equation 2.4 can now be rewritten as

$$E(r) = \frac{i}{\lambda}\int \frac{A(k)}{\sqrt{\cos\theta}} e^{-i(k_x x + k_y y)} e^{-ik_z(k_x,k_y)z} \mathrm{dk_x dk_y}. \tag{2.5}$$

Equation 2.5 is now similar to a Fourier transform of $A(k)$ which can be reexpressed as

$$\begin{aligned} \mathcal{F}(A(k)) &= (2\pi)^{-3/2} \int A(k) \exp(-ikr) d^3k \\ &= (2\pi)^{-3/2} \int A(k)\, e^{-i(k_x x + k_y y)} e^{-ik_z(k_x,k_y)z} \mathrm{dk_x dk_y} \\ &= (2\pi)^{-1/2}\, \mathcal{F}\left(A(k)\, e^{-ik_z z}\right). \end{aligned} \tag{2.6}$$

As stated above, the lensing action alters both the wavefront as well as the polarisation depending on the aperture position as illustrated in figure 2.4. Especially the polarisation vectors at large angle θ, *i.e.* high $k_{x,y}$, can be strongly twisted and lead to depolarisation. This requires the introduction of a depolarisation factor $P(k)$, which arises from geometrical considerations and expresses how much an incident polarisation at position k in the aperture leads to x,y and z-polarisation after focusing [59]. Hence, for focusing light with high numerical aperture objectives the field near the focal plane be reexpressed as

$$E(r) = \frac{ik}{\sqrt{2\pi}} \mathcal{F}\left(P(k)A(k)\frac{1}{\sqrt{\cos\theta}} \exp(-ik_z z)\right), \tag{2.7}$$

where the factor $(\sqrt{\cos\theta})^{-1}$ arises from the product of apodisation factor and $(\cos\theta)^{-1}$ factor (originating from the change of integration variables). Using equation 2.7 the focal field distribution can be accurately calculated for any given beam-shaping device from knowing $A(k)$, *i.e.* amplitude, phase and polarisation in the aperture plane. As an example the action of an easySTED birefringent segmented waveplate is calculated in figure 2.5. Each polarisation direction can be calculated independently. This is especially important when considering the resolution increasing capabilities and dependencies on molecular orientation of these doughnut beams in STED nanoscopy [68]. The MATLAB routine used for the simulations computed in this thesis was kindly provided by MATTHIAS REUSS and further adapted. A more complete description of the above derivation can be found in his work [67]. Using equation 2.7 one can also easily calculate the three-dimensional field distribution of the segmented waveplate important when considering 3D resolution and out-of-focus interference as calculated in figure B.4.

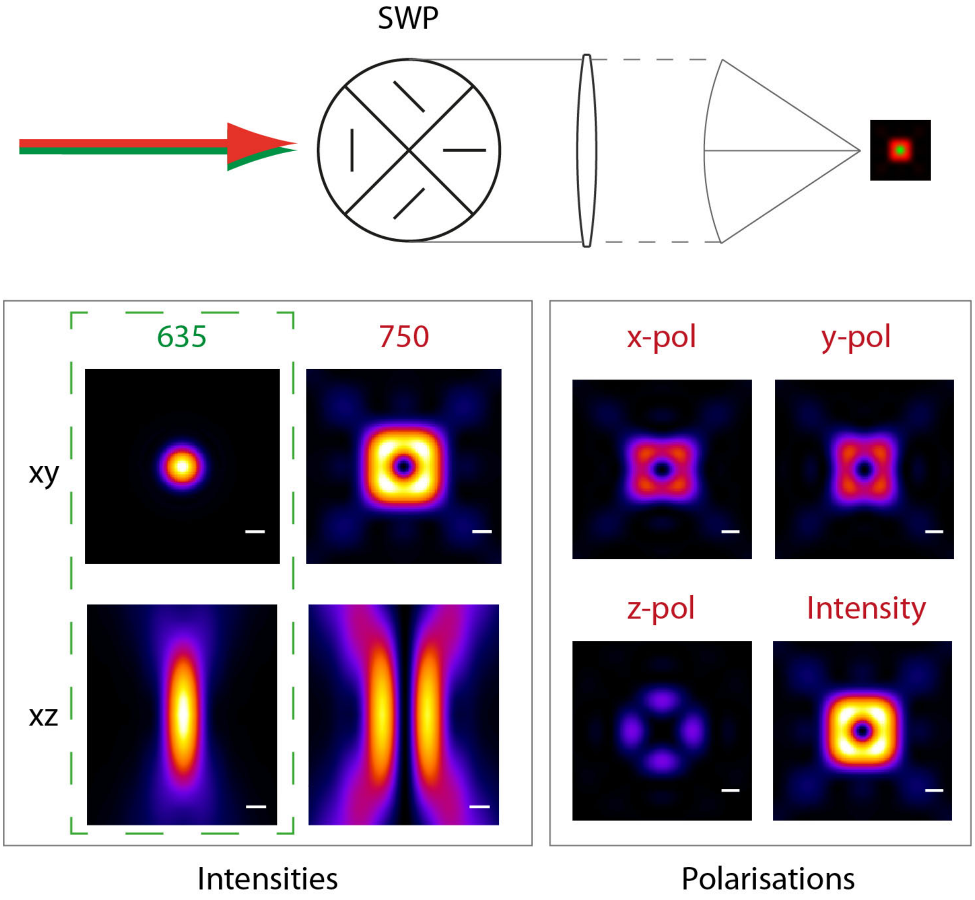

Figure 2.5.: The chromatic segmented waveplate (SWP) is used as chromatic beam-shaping device for generating a doughnut-like field distribution with a central zero intensity at 750 nm and a point-like distribution for 635 nm. The individual three-dimensional polarisation field-components, crucial for determining the response of a fluorophore with fixed dipole orientation to external fields, are calculated for $\lambda = 750$ nm from equation 2.7. Scale bars: 200 nm.

2.5 Temporal information of fluorescence in STED

The modified Abbe formula given in equation 2.3 was first derived for extremely short pulses, by which the molecules residing in the S_1 state are depleted by stimulated emission within a very short time window and before most spontaneous emission can occur. The probability of remaining in the S_1 state scales with $e^{-I/I_{sat}}$. Short pulses represent the most effective way of converting laser power to resolution in STED nanoscopy, but they can also lead to increased photobleaching, phototoxicity and the appearance of multi-photon absorption processes [17]. In recent years continuous-wave (CW) lasers have been increasingly used for STED because of their relatively small cost per available power and wider choice of wavelengths in the visible range. They also allow for inherently simpler setups because laser synchronisation is obsolete. Equation 2.3 was confirmed for STED with CW lasers requiring approximately τ_{rep}/τ_f times more average powers than the pulsed counterpart of repetition period τ_{rep} [93]. The depletion of the excited state by stimulated emission using CW-STED or long STED pulses is a dynamical process, *i.e.* both stimulated and spontaneous emission are competing processes. LEUTENEGGER *et al.* derived a detailed description of the depletion efficiencies depending on STED pulse lengths, inter-pulse durations, and the possible influences of CW excitation and excitation by the STED beam [52]. For long STED pulses or CW-STED the probability of undergoing stimulated emission increases with time and depends on the total number of incident stimulating photons per unit area. In other words the lifetime of the fluorophores undergoing stimulated emission is essentially quenched to an effective lifetime $1/(k_{STED} + k_f)$. Using a modulated STED pattern, the effective lifetime is thus position-dependent and only the molecules residing in the doughnut null retain their full fluorescent lifetime of τ_f. In 2008 the group of PAUL FRENCH pointed out that in FLIM-STED the initial photons were associated with the diffraction-limited confocal signal [6]. Discarding the first photons emitted prior a gating delay τ_{gating} can thus eliminate the confocal socket associated with CW-STED and restore the full resolution known from pulsed STED. Recently two groups theoretically derived and experimentally verified that time-gating with pulsed excitation can enhance the resolution of CW-STED [61, 87]. While increasing the resolution of CW-STED, time-gating inevitably also reduces the overall signal of the STED image and a compromise between resolution and signal-to-noise ratio is necessary.

Being limited by diffraction, various variants of diffraction-limited fluorescence microscopy have emerged to gain more information from the signal by analysing the brightness or spectral properties of the fluorescence and their temporal evolution, *e.g.* FRET, BiFC, FRAP, FLIP, FLIM [41,43,62]. Fluorescent lifetime microscopy (FLIM) can retrieve information that allows the distinction of multiple species of fluorophores with similar spectrum and has been successfully adapted to STED [13]. Other techniques are using photon statistics to extract measurable quantities from the signal. The most prominent ones are fluorescence correlation spectroscopy (FCS) and variants thereof from which diffusion coefficients of molecules in living cells can be calculated [18,56,76]. FCS could already be successfully adapted to STED, because inside the reduced fluorescent volume h_{STED}, STED leaves the molecular properties and thus the photon statistics mostly unaltered [45]. In fact all of the above-mentioned techniques could theoretically be applied to RESOLFT and extent the information gained from the sub-diffractional signal, making RESOLFT more versatile than SMS. Because RESOLFT records ensembles instead of single molecules, it has been criticised for not providing truly quantitative results about the number of fluorescent probes in contrast to SMS, where each localisation event is associated with a single emitter. Estimating the number of emitters in ensemble techniques is challenging due to varying brightnesses. The signal intensity in RESOLFT is dependent on many properties such as activation / excitation / switching laser shapes and intensities, the local environment of the dyes, their orientation and dynamics. A simple way of counting the number of emitters on a surface has recently been achieved by stepwise photobleaching of single GFP molecules [51, 86], which relies on irreversible and complete photobleaching of the sample and has little future in fluorescent recordings involving live-cell or 3D recordings. Here is introduce to STED a new technique borrowed from diffraction-limited fluorescence microscopy: coincidence analysis (CCA), which has already been successfully employed in standard confocal microscopy [83, 85, 89]. CCA performs a statistical analysis of the number of recorded coincident photons per laser cycle onto four single-photon counting detectors and mathematically estimates the number of single-photon emitters (fluorescent molecules) inside the focal volume. It relies solely on the quantum mechanical effect of photon antibunching (PAB) first observed for resonance fluorescence by KIMBLE *et al.* in 1977 [47].

2.5.1 Coincidence analysis

Fluorescent molecules are single-photon emitters, *i.e.* they represent two-level systems that can only emit one photon at a time. Hence, the probability of detecting two photons simultaneously originating from a single emitter goes to zero, known as photon antibunching (PAB). Analogously using continuous wave excitation the fluorescence autocorrelation of a single fluorescent molecule thus drops to zero for $\tau = 0$, called the photon antibunching dip. Due to dead times of single-photon counting

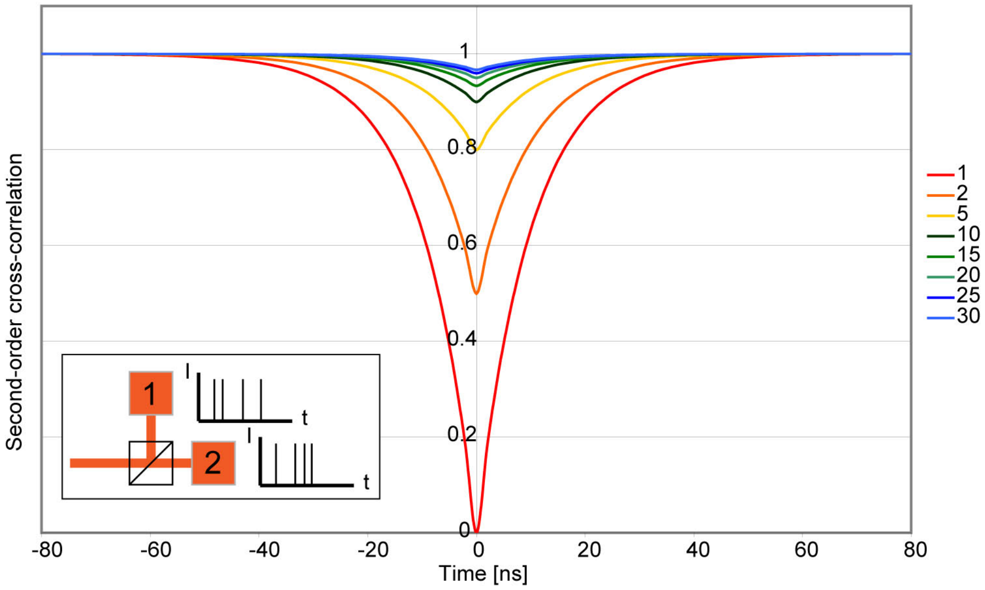

Figure 2.6.: Second-order intensity correlation simulation of the signal recorded by two single-photon counting detectors (inset) in a *Hanbury-Brown–Twiss* optical setup for different number of emitters N and T = 10 ns (N indicated in legend). The calculation presumes that diffusion and shelving to the triplet state occur on much slower timescales than the fluorescence lifetime.

detectors[1], detection of this effect usually requires a *Hanbury-Brown–Twiss* like experiment, consisting of a neutral 50/50 beamsplitter and two detectors [29, 47, 57]. Auto-correlation is hereby replaced by cross-correlation between the detectors or measuring the inter-photon time. If more than one emitter is now contributing to the detected photon flux signal, the PAB dip will become less pronounced. Assuming that diffusion and triplet shelving occur on much longer timescales than photon antibunching, the second-order intensity correlation of these two single-photon detectors can be approximated by $g^{(2)}(t) = (N-1)/N + (1/N)(1-e^{-|t/T|})$, where N represents the number of emitters and $T = 1/(k_1 + k_2)$ with effective excitation pump rate k_1 and spontaneous emission k_2 [40]. $g^{(2)}(t)$ is calculated with for $T = 10$ ns and different N in figure 2.6. It shows that for higher number of emitters, the PAB dip gets increasingly smeared out.

---

[1] The dead time is the time after the detection of a photon in which the detector is non-responsive to a second photon.

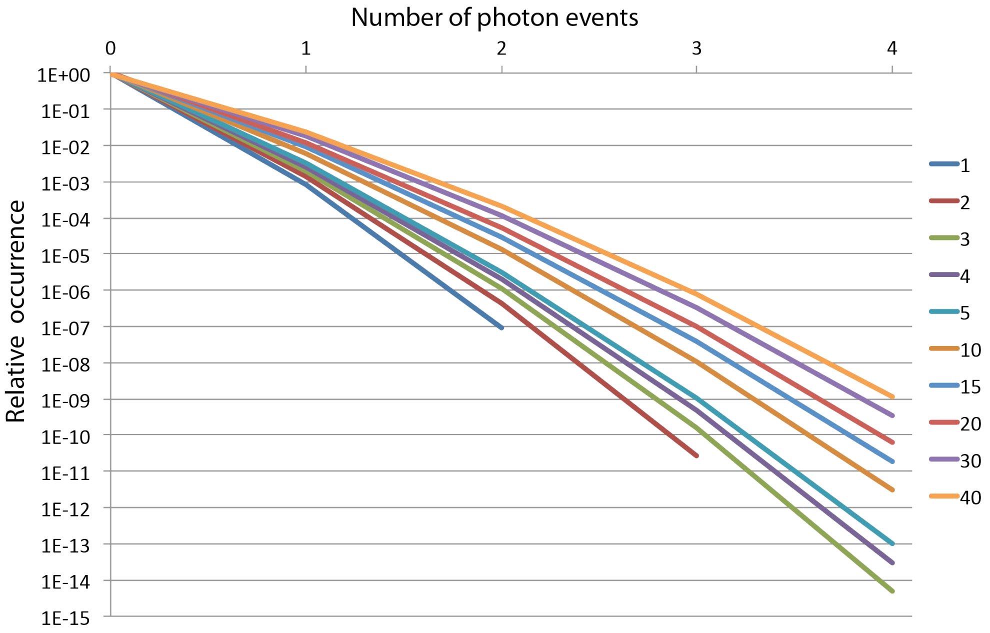

Figure 2.7.: Simulated normalised probability distribution (with respect to 1-photon probability) given by equation 2.8 of detecting 1–4 coincident photons per laser cycle for N molecules located in the focal volume (N indicated in legend), each emitting a photon with a probability $p = 0.0006$ and a background detection probability $p_b = 0.0002$

Another approach of analysing the PAB dip is to used pulsed excitation [55]. The second-order intensity correlation is replaced by a statistical analysis of coincident photons (CCA: coincidence analysis) [82, 85, 89]. The analogy to the PAB dip is that only one photon can be emitted per molecule and laser cycle, *i.e.* allowing for no coincident photon pair for single emitters. Unfortunately correlations noise and detector dead times make emitter counting by correlation or coincidence analysis by two detectors unreliable for counting larger number of molecules than $N = 3$ [31]. Ta *et al.* recently experimentally demonstrated that by splitting the fluorescence onto four single-photon counting detectors instead of two, they could determine up to $N = 15$ emitting molecules from the combined photon statistics of the four detectors without prior calibration [83]. The number of recorded photon events in each laser cycle is here compared with the multi-photon probability distribution. For including background photons and dark current in the statistical analysis, Ta treated the background as an additional fluorophores with low molecular brightness and event probability p_b. Furthermore, the detection of only one photon per detector was allowed, which is a reasonable assumption due to the $\sim$ 30 ns dead time of commonly used avalanche photodiodes (APDs). Using m detectors, the multi-photon probability distribution $P(n;p;i)$ can then be modelled as [83]

$$P(n;p;i) = \binom{m}{i} \begin{bmatrix} (i\frac{p}{m} + 1 - p)^b (i\frac{p_b}{m} + 1 - p_b) \\ -\sum_{k=0}^{i-1} \frac{\binom{i}{k}}{\binom{m}{k}} P(n;p;k) \end{bmatrix}, \tag{2.8}$$

where n is the number of molecules in the focal volume and i is the number of detection events in one laser cycle. The emission probability p is to be estimated computationally but is essentially the molecular brightness b normalised by the repetition rate r_{exc} of the pulsed laser used for excitation. $b = P_{exc}\alpha\sigma_{abs}\varphi_f$ is the product of the excitation power P_{exc}, the detection efficiency α of the setup, the absorption cross-section σ_{abs} and the fluorescence quantum yield φ_f of the fluorophore. Most importantly this method estimates the number of emitters independently from the molecular brightness. A high detection efficiency α is, however, important for recording the necessary multi-photon events and fitting the distribution to equation 2.8. For $m = 4$, Ta *et al.* used these model functions in a Levenberg–Marquardt algorithm to estimate the number of molecules n and the normalised molecular brightness p from multi-photon distributions. These multi-photon events were recorded by time-correlated single-photon counting (TCSPC) with a confocal fluorescence microscope equipped with four avalanche diodes (APD) for single-photon detection. For reasonable values of $p = 0.0006$ and $p_b = 0.0002$, the probability distribution of the multi-photon detection probabilities are calculated from equations 2.8 for a range of emitting molecules N in figure 2.7. In contrast to second-order intensity correlation by two detectors as displayed in figure 2.6, CCA only needs a distribution of four values to be fitted by varying n and p, and can count up to higher values before saturation [83]. A high accuracy of the method obviously depends on large photon statistics and high collection efficiencies.

In 1995, photon statistics were first used to increase optical resolution by multi-photon detection [36] and ten years later to enhance STED nanoscopy in FCS-STED [45], as mentioned before. Ta proposed that CCA can also be extended to STED [83]. Collaborating on this work with Anton Kurz from the Herten group, similar and extended algorithms for applying CCA to super-resolution microscopy have been used[1]. This work shows the first combination of coincidence analysis with $m = 4$ detectors and STED nanoscopy.

---

[1] Modifications included a bootstrapping method for determination of statistical variance inside the sample set.

3

Parallelisation of STED/RESOLFT type nanoscopy

The next chapter is first giving an introduction to parallelisation and what fundamental limits determine the minimal acquisition time to recorded an image in stochastic and targeted nanoscopy. A new parallelisation easySTED design is introduced and evaluated. Finally the possibility of parallelised multicolour imaging is demonstrated and the various chromatic properties of beam-splitting and -shaping discussed.

3.1 Introduction

The optical fluorescence nanoscopy methods can, as described in the introduction, be divided in the two categories: stochastic and targeted methods. While the stochastic methods are inherently parallelised because the field of view (FOV) is identical to the parallelised area, the targeted switching and readout methods historically rely on point-scanning and often confocal arrangements because they offer the highest lateral resolution among the diffraction-limited microscopy methods. Analogously, nanoscopy methods aiming at achieving the best axial resolution are commonly based on a 4-Pi optical setup.

The main disadvantage of the single-point scanning microscope is that the maximal 2D recording speed quadratically depends on the pixel size (or cubicly on the voxel dimensions for 3D) and consequently increases with the microscope's resolution if the Nyquist criterion is to be fulfilled. Additionally higher resolution leads to fewer fluorescent molecules in the fluorescent volume, emitting fewer photons. In order to provide the same signal intensity and S/N ratio as for conventional confocal microscopy, single-point scanning super-resolution microscopes thus require substantially longer acquisition times.

STED relies on targeted switching and readout and therefore cannot circumvent a scanning approach. While the volume, from which fluorescence is allowed, exhibits sub-diffractional dimensions due to the STED beam, the fluorescence itself always undergoes diffraction in far-field microscopy. The requirement for scanning and thereby time-sequential recording is only necessary inside a diffraction-limited volume. A signal originating from a molecule located at a coordinate r_2 can just about be distinguished from a molecule residing at r_1 given that $|r_2 - r_1| > \lambda/2n \sim 250$ nm in a typical imaging system as given by the Rayleigh criterion. One can therefore build an imaging system where an array of detectors each record the signal originating from a different location in the focal plane (and in theory also originating from a different plane) given that the coordinates fulfil the above condition. In order to minimise cross-talk between the detectors one should consider, if possible, using larger separations. Furthermore the second illumination field present in RESOLFT, responsible for switching the molecules, is also diffraction-limited. Parallelised RESOLFT is therefore also limited by the minimal separation of the neighbouring zero intensities, *i.e.* $\lambda/2n$[1].

Placing several optically identical point-scanning beams in the focal plane and operating them in parallel is commonly known as parallelisation. For RESOLFT, the pattern of the switching beam hereby determined the geometry of the detection. If an array of doughnut-shaped switching beams is chosen, the detection should cover an identical arrangement of point detectors. If quenching and resolution enhancement is only provided in one direction (*e.g.* stripes), an area or line detector (*e.g.* CCD) is required. The limiting factor for scanning in one lateral direction is given by the time required to scan the $\sim$ 250 nm set by diffraction. As an example, typical STED recording use pixel dwell times of $10 - 100$ µs at pixel sizes of $10 - 20$ nm and thus require a frame time of $2 - 60$ ms for a 250×250 nm^2 FOV. The frame rates thereafter simply scale with area and inversely with degree of parallelisation. The achievable frame rates for STED can then be of similar magnitude as for commercial 512×512 EMCCD cameras with a framerate of 35 fps (frames per second, $\sim$ 30 ms). Using a resonant beam scanner for the fast axis, STED has indeed reached 28 fps with 62 nm resolution (30 nm pixel size) and a FOV of 1.8×2.5 µm^2 (60×83 pixel^2) with an average pixel dwell time of 7 µs. The exact geometry of excitation and depletion fields, *e.g.* distance between parallelised beams, then allows for different scanning schemes as described in more detail in the following section 3.2 and illustrated in figure 3.3. If a slower switching mechanism is used that has advantages over STED regarding required switching power and hence phototoxicity, the same frame rates

---

[1] This limit obviously only holds in the direction where an increase in resolution is desired, e.g. for striped switching pattern (structured illumination) in the perpendicular direction to the stripes

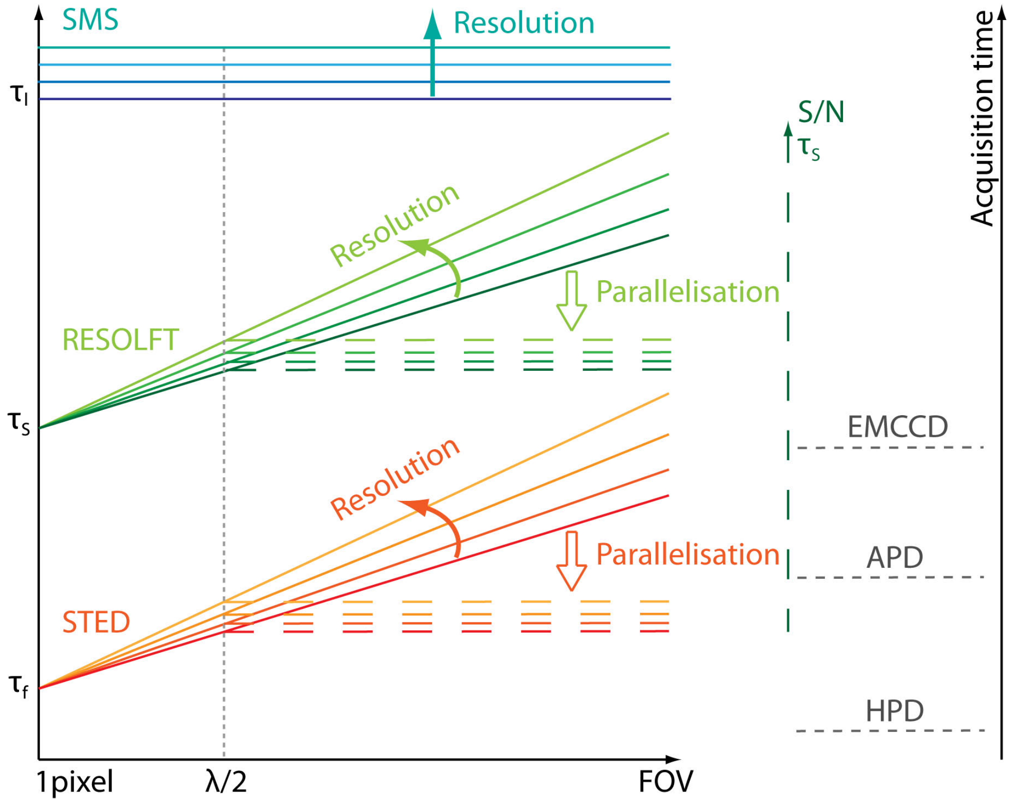

Figure 3.1.: Fundamental recording time limits in optical nanoscopy are illustrated including parallelisation. On the right side the recording speeds of the different commercially available detectors are shown for comparison. The time to record a single pixel in targeted RESOLFT nanoscopy is limited by the time to switch the state of molecules between a signalling and non-signalling state, given by τ_s, and by the fluorescence lifetime τ_f (which sets the lower limit of collecting a single photo per pixel). STED is a special case with the switching rate being identical to the fluorescence lifetime and thus represents the fastest possible switching mechanism. Up to a FOV of $\sim \lambda/2$ the recording time of targeted nanoscopy scales with the number of required pixels and thus the resolution. For larger FOVs, parallelisation can counteract the longer acquisition time required in scanning microscopy. SMS is inherently parallelised and the localisation time scale τ_l as well as the resolution are inherently coupled to τ_f (by requiring N photons for a $\sqrt{N}$ increase in resolution as well as sufficient localisation events for generating a homogeneous image). Because SMS allows for no tuning of the resolution (as it depends on the number of photons that come out), the labelling density has to match the resolution. For STED/RESOLFT, in contrast, tuning of the resolution is possible. The SMS recording time relies extensively on precise understanding of the underlying (stochastic) photophysics and post-processing algorithms. The signal-to-noise ratio (S/N) increases with acquisition time in targeted nanoscopy.

might, however, never be reached. An alternative to an array of doughnuts is the above-mentioned structured-illumination or striped approach in which a pattern of parallel stripes is scanned over the sample at different angles [66]. The acquisition time of this approach would only linearly depend on the resolution and the number of scanning angles, but requires more post-processing. Altogether there is a close relationship between signal, contrast, resolution, light pattern, scanning speed and field of view and parallelisation is crucial for achieving the best output in optical targeted nanoscopy as summarised in figure 3.1.

From a physical point of view the temporal limit of RESOLFT depends (i) on the rate for switching the signalling state of molecules OFF or ON and (ii) the fluorescence lifetime for collecting theoretically at least a single photon for identifying the molecule residing at the null. While these two rates are coupled in STED nanoscopy, *i.e.* the switching rate is limited by the fluorescence lifetime and only a single photon can be emitted per switching cycle, they are decoupled in other switching mechanisms, *e.g.* photoswitching by photo-isomerisation. If switching and readout (excitation/emission) are decoupled, once an ensemble of molecule is switched OFF, the remaining ones can emit as many photons as allowed by their fluorescence emission rate, *i.e.* lifetime. Targeted nanoscopy by STED is often limited by the laser intensities required for obtaining the highest resolution, both technically (high power commercial laser systems are complex, expensive and often unavailable) and for imaging biological samples (bleaching, phototoxicity, multi-photon absorption, autofluorescence). Because the laser intensity required for switching has to outperform the competing process (STED: Spontaneous fluorescence, RESOLFT: Spontaneous “Switching Back”), the ideal RESOLFT dye would have a slow switching mechanism combined with a fast fluorescent lifetime.

A switching cycle needs to be completed before a next pixel can be addressed. For this reason pulsed laser sources in combination with STED nanoscopy allow for the fastest possible recording in fluorescence far-field nanoscopy with a minimal pixel dwell time of $\sim$ 5 ns (and 5 ns $\times$ 25 $\times$ 25 pixel^2 = 3 µs for a 250 $\times$ 250 nm^2 FOV at 10 nm pixel size)[1]. This said, it is believed that STED or other fast switching mechanisms will always play an important role for obtaining the fastest possible image recordings despite the higher laser powers required. Regardless of the switching mechanism used for RESOLFT, parallelisation will be required to reduce

---

[1] Usually 80 MHz laser systems are employed corresponding to an inter-pulse time of 12.5 ns whereas 5 ns correspond to a 200 MHz system. Longer inter-pulse times increase the probability of all molecules relaxing back to the ground state. $<$1 MHz systems (1000 ns) were used to further allow relaxation from long-lived triplet/dark states and reduce photobleaching [19].

scanning times for FOVs. The reduction in scanning time is linearly proportional to the degree of parallelisation. The fundamental limits of the different optical nanoscopy methods are illustrated in figure 3.1 in order to demonstrate how and up to what limit parallelisation can restore the disadvantages of beam-scanning for reducing the acquisition time or increase the FOV.

Although optical setups are approaching these fundamental limits, parallelisation is still struggling with mainly technical problems. Among these are the generation of the desired illumination fields and the requirement of commercially unavailable lasers, detectors, optical components or dyes. Our research group is focusing on all of these topics as well as novel applications for sub-diffractional far-field optics [92]. The work in this thesis concentrates on parallelisation of STED nanoscopy by $m = 4$ multispot generation, consisting of four identical point-like excitation beams overlaid with four depletion beams of the commonly known doughnut shape. Based on STED, this work should nevertheless be recognised as a first experimental realisation of parallelised RESOLFT while preserving resolution and scanning properties of conventional single-spot RESOLFT microscopes[1].

3.2 Setup

Using a single fibre output the defendant of this thesis constructed an auto-aligned four-spot multispot STED setup including Wollaston prisms for multispot generation, a chromatic segmented waveplate (SWP) to shape the focal spots and four single-photon detection units for detection as described in figure 3.2. Excitation was either used from a 510 nm pulsed laser diode (LDH-D-C-510, PicoQuant, Germany) or selected from a supercontinuum source (with the most regular operation at 633 nm) (SC450-20-2, Fianium, Southhampton, United Kingdom), which also procured the STED wavelength at 745 nm from a second exit port. All laser wavelength were coupled into a common fibre for procuring spatially self-aligned beams. At the exit of the single-mode polarisation maintaining NA=0.12 fibre (PM630-HP, Thorlabs, USA) all wavelengths were essentially unpolarised because their polarisations at the fibre input were already either unpolarised (Fianium) or circular polarised (using a $\lambda/4$ waveplate) and the fibre itself led to additional depolarisation. The wavelengths originating from the fibre output were collimated using a $f = 20$ mm lens and separated into four sub-beams using a stack of two 20” ($1/3°$) Wollaston prisms (Jenoptik, Germany) rotated by 45° with respect to each other

---

[1] Previous work by Miriam Schwentker relied on wide-field illumination and detection and therefore reduced optical sectioning capabilities [75].

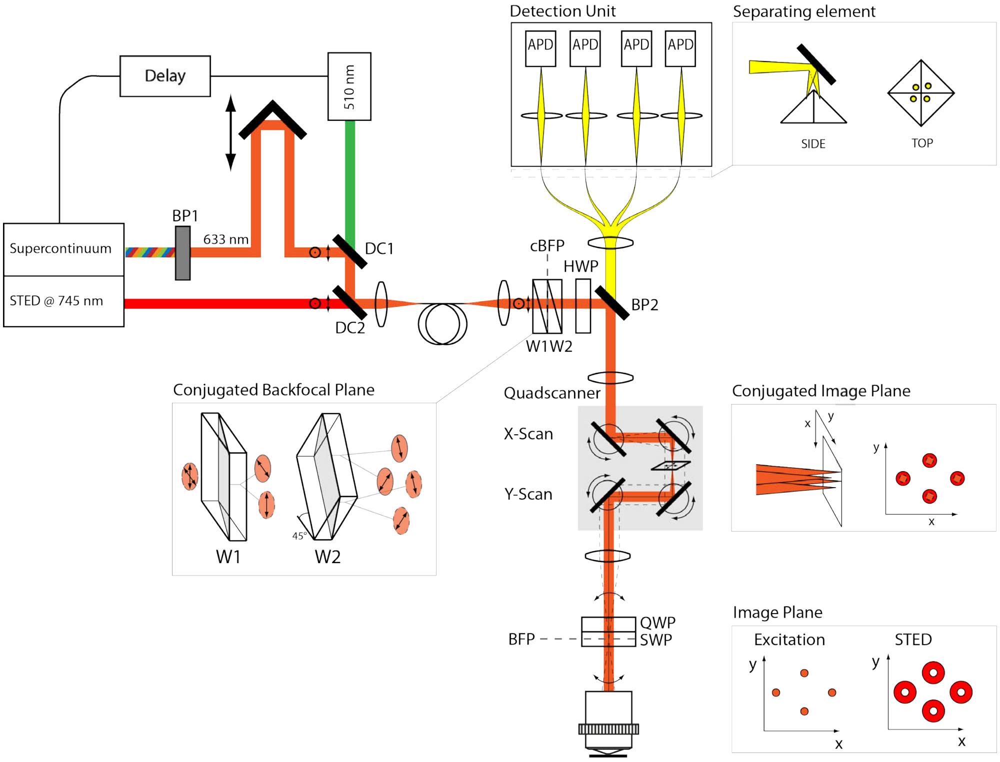

Figure 3.2.: Schematic setup of a parallelised STED microscope: A stack of Wollaston prisms (W1,W2) are used for generating the multiple foci and a segmented waveplate (SWP) for shaping the individual wavelengths to either focused excitation spots or doughnut-shaped STED beams (Inset: Image Plane). For standard operation unpolarised excitation (633 nm, selected using a bandpass filter BP1) and STED (745 nm) originating from laser outputs pumped by a common pump laser are combined using a dichroic mirror (DC2) and coupled into a common single-mode-fibre after adjusting timing by inserting an optical delay. Additionally a 510 nm diode laser was circularised (not shown), combined with the other wavelengths using a dichroid mirror (DC1), and coupled into the fibre for allowing multicolour imaging. All unpolarised or circular polarised output wavelengths are split into four polarised beamlets in the conjugated backfocal plane (Inset: Conjugated Backfocal Plane; arrows indicate linear polarisation orientations of the individual beamlets). A half-wave plate (HWP) is introduced for reducing depolarisation at the subsequent reflection surfaces. All beamlets are then reflected by a bandpass filter (BP2) and focused into a home-built so-called Quadscanner, consisting of four motorised mirrors, placed in the conjugated image plane (Inset: Conjugated Image Plane). The first pair of mirrors induces a lateral displacement in one direction (X-Scan) while the second pair displaces the beams in the perpendicular direction (Y-Scan). All beamlets are circularised using a quarter-wave plate (QWP) to avoid a bias on STED induced by molecular orientation before passing through the SWP, which acts as beam-shaping device. The fluorescence passes back through the scanner and bandpass filter before being focused onto a mirrored pyramid, which splits the fluorescence originating from the four focal volumes (Inset: Separating element). Each fluorescent signal is focused onto a single-photon counting module (APD). Photographs of the setup are shown in appendix B.2

to generate four uniform beams in a rhombus-like pattern in the objective plane (Fig 3.2 inset). The beam diameter was adjusted with an iris to match the pupil size of the selected objective lens. Wollaston prisms separate light beams into two orthogonally polarised sub-beams that exit the device at an angle $\Delta\delta$ given by

$$\sin\left(\frac{\Delta\delta}{2}\right) = b\tan(\gamma), \tag{3.1}$$

where $b = n_E - n_O$ represents the birefringence between ordinary and extraordinary polarisations and γ the cutting angle of the prism's wedges. Hence, from an initially unpolarised or circular input polarisation the stack of two Wollaston prisms produces four linearly polarised beamlets of which two are polarised orthogonally with respect to the other two. Both laser wavelengths that are required for STED nanoscopy can now originate from a single fibre while remaining perfectly co-aligned, which makes alignment of the multispot beam generation redundant. The consequence of dispersion, which actually affects birefringence $b(\lambda) = n_E(\lambda) - n_O(\lambda)$ and thus the splitting angle, will be discussed in further detail in section 3.3.3.

In order to guarantee a central position of all the beamlets in the backfocal plane the Wollaston prisms are placed near the conjugated backfocal plane (cBFP). An important consideration is that beam-splitting and -shaping elements should not interfere with the fluorescence in the detection path. In a beam-scanning setup with point detectors this requires that the fluorescence is decoupled preferably at a location in between scan lens and beam-splitting element, where the fluorescence is immobile and collimated. The Wollaston prisms are placed on a removable mount in order to flexibly switch between multispot and single-spot configurations.

After being split into four beamlets, the laser beams are reflected by the bandpass filter (z625-745 rpc, Custom-Made, AHF, Germany) and focused into a custom-made beam-scanner (QuadScanner), consisting of four galvanometric mirrors (Cambridge Technology, USA), placed next to a commercial microscope (DMI 3000B, Leica Microsystems, Germany). The beam-scanner effectively displaces the focused beams laterally in the conjugated image plane and consequently also in the image plane by a 100–fold smaller displacement due to the 100× magnification of the objective lens. Its geometry is described in more detail elsewhere (Patent number: WO2010069987). The magnification of the QuadScanner was calibrated by scanning and recording the scattered light of a silicon wafer with well-defined dimensions. The four individually programmable mirrors further allowed for careful calibration such that the beams rotate near the backfocal plane. This ensures that the beam-scanning plane of rotation coincides with the location of the beam-shaping device. In most common objective lenses the pupil plane lies inside the objective lens, which makes it inaccessible for the the SWP. Simulations made in this group predict that placing the SWP and plane of rotation just below the objective lens should give sufficiently good results for our purpose. Alternatively the beam-shaping element could also be placed in the conjugated backfocal plane together with the beam-splitting element. Ideally both elements are placed in exactly conjugated planes and should therefore not occupy the same location. The bandpass filter used in reflection can also induce unwanted polarisation effects, which encourages placing the beam-shaping element in the backfocal plane.

The segmented waveplate (SWP), used as beam-shaping device (B. Halle, Germany), consists of four segments of crystal quartz cut from a single block and assembled with the fast axes oriented as illustrated in figure 2.5 (Patent number: WO2010133678). The thickness was manufactured such that a birefringent retardation of 2.5λ is achieved for 750 nm, 3λ for 633 nm and $\sim$ 3.8λ for 510 nm between the slow and fast axis of the crystal (see Fig. 3.10). Matthias Reuss calculated in his work that the SWP can be used within ± 5 nm of its design wavelength without mayor drawbacks [67]. Initially designed for a Ti:Sapphire laser line at 750 nm, the same SWP could therefore be used for $\lambda = 745$ nm of the Fianium laser. The SWP was placed just before the 1.46 numerical aperture 100× oil objective lens (Leica Microsystems, Germany). Most importantly, regardless of the input polarisation, the SWP shapes the STED beam into a doughnut-shaped beam with a central zero intensity in the focal plane (as required for RESOLFT nanoscopy) while leaving the excitation wavelengths largely unaltered, *i.e.* forms a diffraction limited spot-like distribution known as an Airy pattern.

In order to avoid non-uniformly distributed polarisation directions of excitation and STED wavelengths, which could lead to artefacts due to the dipole orientation of fixed fluorescent molecules, the polarisations of all beamlets are circularised before the SWP using an achromatic $\lambda/4$ waveplate. This requires that incident beams are linearly polarised and either perfectly parallel or orthogonal with respect to each other. To eliminate spurious depolarisation effects, the polarisations originating from the Wollaston prisms are immediately rotated using a $\lambda/2$ waveplate, such that the individual beamlets are either *s*- or *p*–polarised with respect to the plane of reflection at the bandpass filter and beam-scanning mirrors.

The focused beamlets create four spatially separated excitation volumes whose fluorescence is again collected by the objective lens and transmitted across SWP, tube lens, QuadScanner, and Scan lens. The SWP only marginally influences the beam profile because the fluorescence spectrum lies in between excitation and STED wavelengths. It is therefore only slightly broadened by the SWP after focusing, compared to the undisturbed case [67]. After passing the scan lens, the fluorescent beams are decoupled from the excitation path by crossing the bandpass filter, previously used in reflection. The maximal detection band is therefore limited by the bandpass filter to $\sim 650 - 720$ nm. At this position the fluorescence is both collimated and descanned, meaning it does not move while scanning and is quasi-non-divergent. The fluorescence originating from each of the four non-interacting fluorescent volumes is emitted at the same angle previously set by the Wollaston prisms and can be decoupled from the other signals by focusing the fluorescence, creating four distinct (fluorescent) foci. Both the distance and size of the foci linearly scale with the focal length of the refocusing lens. This obviously makes detection by point-detectors challenging because the beams have to be first spatially separated before being focused individually on different detectors, *i.e.* multispot microscopy requires an optical cross-section converter. As shown in appendix B.2 and illustrated in figure 3.2 (inset), a custom-made silver-coated pyramid was here used as cross-section converter and placed in the second conjugated image plane (the first one lying inside the scanner). Alternatively a specially designed fibre bundle was considered, allowing detection of even higher degrees of parallelisation (appendix B.6). After focusing with a $f = 300$ mm lens onto the tip of the pyramid, the four independent fluorescence signals are separated and four $f = 50$ mm lenses used to refocus the fluorescence onto four single-photon counting modules (SPCM-AQR-13/14, Perkin-Elmer, USA). The signal recorded from each of the detectors will from here on forth be referred to as (detection) channel. The focal length of the focusing lens ($f = 300$ mm) was chosen such as to match the airy diameter of the focused fluorescence (162.9 µm) to the detection area of the avalanche photo diodes of 180×180 µm^2, which are thereby acting as quasi-confocal pinholes[1]. Finally additional shortpass (SP750, Semrock, USA) and bandpass (675/50, Semrock, USA or HQ690/60x, Chroma, USA) interference filters were placed in the detection path to further isolate the fluorescence from reflected excitation and STED light.

For scanning a fluorescent sample in axial direction and reducing thermal drifts, the sample was clamped directly to the objective lens by a home-build sample holder with an integrated linear piezo-electrical actuator (PI, Karlsruhe, Germany) for controlling the axial position of the sample. (Photographs of the setup are shown in appendix B.2.) Scanning as well as data processing of the collected signal was controlled using a FPGA board

---

[1] The refocusing by the $f = 50$ mm lenses were place as to provide a $1 : 1$ magnification and thereby did not change the Airy disk size.

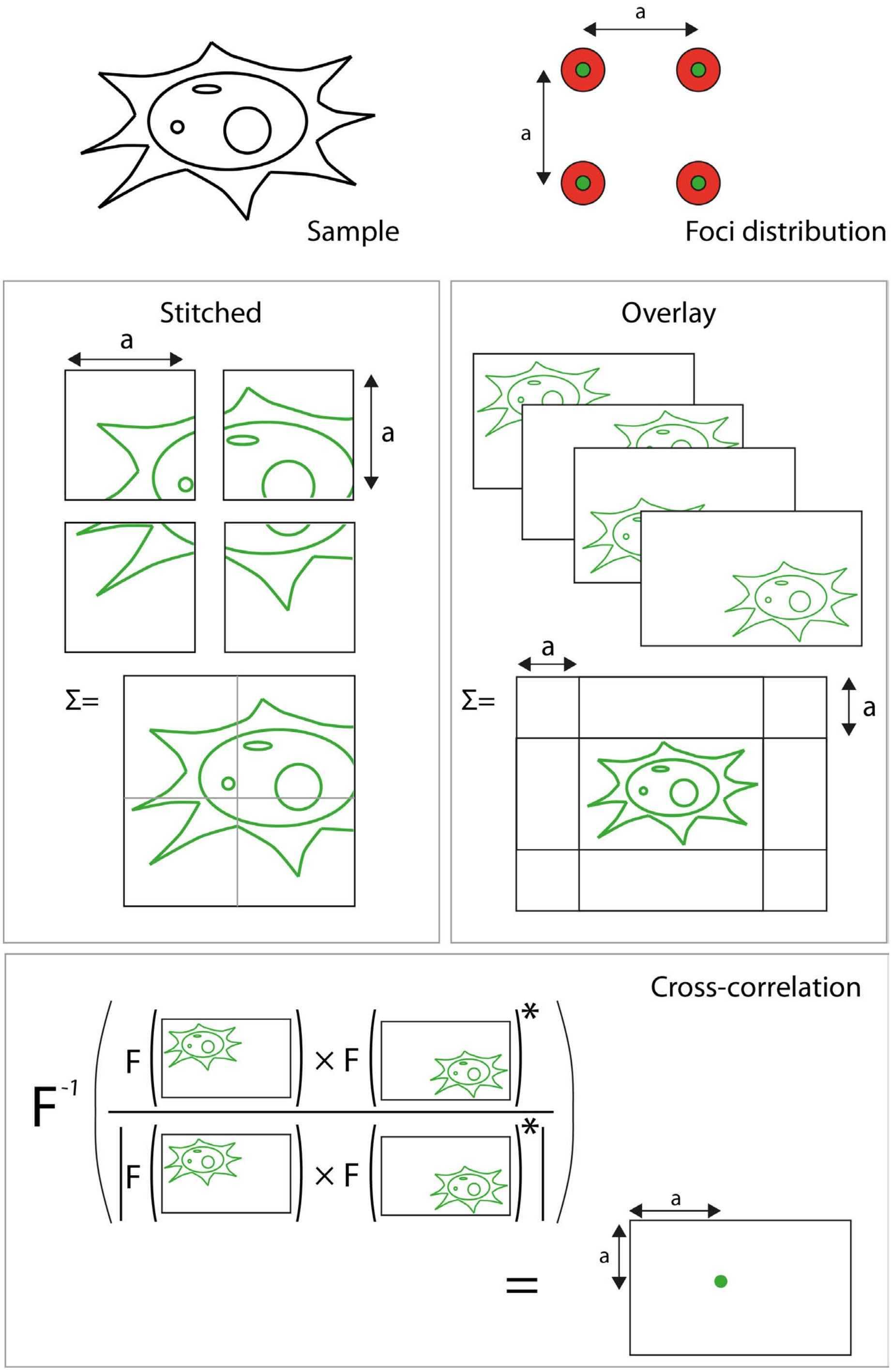

Figure 3.3.: Illustration of possible scanning schemes for a descanned multifocal microscopy setup such as used in this work. The sample is laser-scanned by four excitation spots separated by distances *a*. In the stitching scheme FOVs of $a \times a$ are scanned and recombined in a mosaic-like pattern whereas in the overlay schemes the individual images are added including an offset set by the foci geometry. The offset required in both schemes for recombining the images can be calculated from the cross-correlation between two large FOV images, explained in more detail in appendix B.3. F, F^{-1}, and * represent Fourier transform, inverse Fourier transform and complex conjugates.

(PCI-7833R, National Instruments, USA) and self-built scanning software (LabVIEW, National Instruments, USA) written by Johann Engelhardt. Different imaging approaches were taken regarding scanning and recombination of the different channels to obtain faster acquisition due to parallelisation (see Fig. 3.3). The first approach is to scan four non-overlapping areas and to recombine the individual frames by stitching them together in a mosaic-like pattern. For larger FOVs an array of scanning positions was addressed in order to avoid multiple scanning of the same positions (see appendix B.7). The second approach consists of scanning four large area images simultaneously at a four-times shorter pixel dwell time and adding the overlapping regions of the full-scale frames. The recombination of the individual overlapping was done by first calculating the six differing cross-correlations, as illustrated in figure 3.3 (Cross-correlation), between the four images as

$$\text{Cross-correlation} = \mathcal{F}^{-1}\left(\frac{\mathcal{F}(\mathit{Image}\ 1)\times\mathcal{F}(\mathit{Image}\ 2)^*}{|\mathcal{F}(\mathit{Image}\ 1)\times\mathcal{F}(\mathit{Image}\ 2)^*|}\right), \tag{3.2}$$

using a custom MATLAB software routine. $\mathcal{F}$, $\mathcal{F}^{-1}$ and * represent Fourier transform, inverse Fourier transform and complex conjugates. The offsets between the individual frames were determined by fitting a Gaussian onto each cross-correlation using a maximum-likelihood algorithm. In order to minimise the error in determining the three offsets of channels 2–4 with respect to channel 1, *e.g.* different image contrast due to detection misalignment or bleaching, the three offsets were determined by selective averaging between of the six offsets gained from the gaussian fits (appendix B.3). Furthermore the images could be resampled before recombination to minimise sampling errors. Other intermediate scanning schemes or different multispot arrangement (*e.g.* arranged in a line) are also possible but are not further pursued in this work.

To further simplify the setup, a custom laser system (SC450-20-2, Fianium, United Kingdom) was used with a single laser pump operating at a repetition rate of 18.45 MHz and generating two unpolarised outputs: a supercontinuum spectrum ranging from 490 nm to 720 nm and a high power output used for STED at 745 ± 5 nm. The excitation band (Z633/10 X, Chroma, USA) is selected from the supercontinuum spectrum. Excitation was recombined with the STED line using a dichroic mirror (SP750, AHF, Germany), after an optical delay maximising STED. Initially another band at 495 nm was selected from the supercontinuum band requiring an additional optical delay due to temporal dispersion in the fibre. A 510 nm diode laser later replaced this configuration because the supercontinuum spectrum proved to be very unstable towards the blue edge. Using a second dichroid mirror (540 LP, AHF, Germany), the 510 nm diode laser was combined with the 633 nm laser band selected from the supercontinuum spectrum. Once coupled into a single fibre, excitation originating from the supercontinuum and STED laser beams no longer required any spatial or temporal alignment (due to the common laser pump). The 510 nm diode laser was triggered by the output synchronisation port from the STED laser using a home-built electronic delay box. Excitation and STED were performed with a total time-averaged optical power per focal spot of $0.5 - 2$ μW and $2.5 - 30$ mW at the back aperture of the objective lens. Pulse lengths were ~ 110 ps (FWHM, 633 ± 10 nm, supercontinuum), < 150 ps or < 600 ps (FWHM, 510 nm diode laser, variations depend on power level and pulsing mode) and ~ 77 ps (FWHM, 745 ± 5 nm band at the common fibre output. The Wollaston prisms introduced minor reflection losses. Samples were prepared as described in appendix A.

3.3 Results

3.3.1 Parallelisation of STED

Using the setup described in figure 3.2, STED and excitation multispots were generated in a rhombus-like distribution in the focal plane due to the stacked arrangement of the two Wollaston prisms (Fig. 3.4). For one beam pair, the excitation (green) and STED (red) focal light distributions were obtained by scanning an 80 nm gold bead (BBInternational, UK) across the focal region. Four-leaf-shaped doughnuts were obtained for the STED beam at a wavelength of 745 nm due to the fourfold segmentation, while the excitation spots at 633 nm remained largely unaltered. The central intensity of the doughnut resides below signal background, which should guarantee for good resolution improvement and fluorescence signal. The measured excitation spots (633 nm) were separated on average by 5.75 ± 0.07 μm in the long axis at an angle of 45°, but one Wollaston orientation exhibited a slightly larger splitting angle (Fig. 3.12).

First to be investigated was whether the Wollaston prisms did provide a real loss-free solution for parallelising STED. The increase in resolution of the system was tested by imaging 20 nm fluorescent beads (Invitrogen, USA) filled with Crimson fluorophores (625/645) in both confocal and STED microscopy modes as well as with and without stack of two Wollaston prisms (Fig. 3.5). When including the prisms, fourfold total laser intensities (four all beams combined) were employed to compensate for the fourfold parallelisation. Although the FWHM values measured across one crimson bead varied slightly when comparing measurements with and without Wollaston prism, the increase in resolution is similar in both

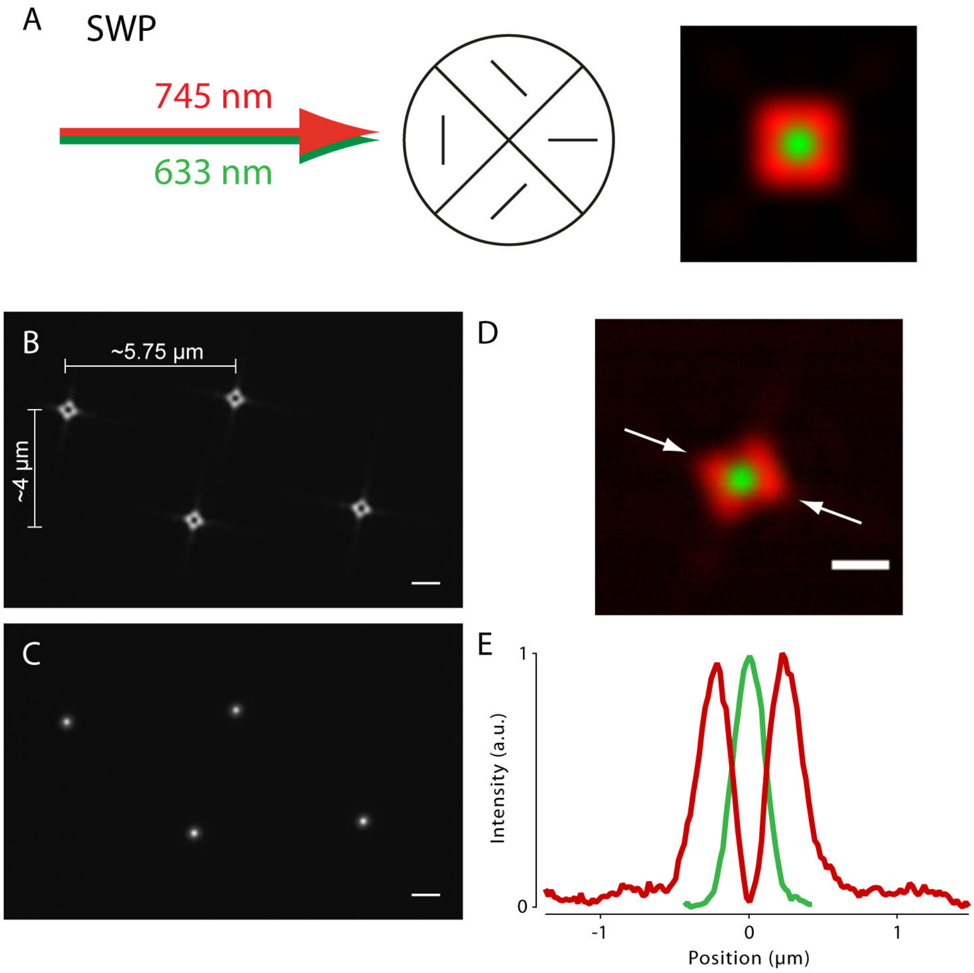

Figure 3.4.: *Top*: (A) Simulated beam-shaping action of a segmented waveplate for 635 nm and 750 nm resulting in a doughnut-shaped STED beam (red) and a gaussian-shaped excitation beam (green). *Left*: STED (B) and excitation (C) spots are arranged in the Rhombus-like pattern when focusing the light after the SWP directly onto a CCD camera (Scale bar: 1 µm). *Right*: (D) Exemplary focal intensity distributions of one of the four parallelised excitation (green) and STED (red) beam pairs obtained by scanning a 80 nm gold bead across the focal region and collecting the scattered light using a photomultiplier tube. After having passed the segmented wave plate the 745 nm STED beam becomes a doughnut, while the 633 nm excitation beam is focused to a regular spot (Scale bar: 500 nm). (E) Line profiles of excitation (green) and STED (red) focal spots along the direction indicated by the arrows on the top image.

cases. The similar increase in resolution demonstrates the scalability of parallelisation and in particular our parallelisation design without major losses.

Figure 3.5 further shows the focal light distributions of parallelised and regular recordings by again scanning 80 nm gold beads across the focal light pattern. In the parallelised image two nearby gold beads are visible that are fourfold multiplied in the expected Rhombus-like pattern with no evident change in shape compared to the single-spot recording. The parallelised light pattern scan exhibits a large and noisy background, which originates from strong backscattering of the light at the various optical elements (QWP, SWP) and the large pinhole in front of the PMT detector required for collecting the scattered light from all four beamlets. This in turn makes the simultaneous and exact measurement of the individual central null positions difficult and unreliable.

Figure 3.5 demonstrates the increase in resolution of only one of the four detection channels. The images obtained in the subsequent figure 3.6 is a proof of having a sufficiently good central zero intensity in all four channels. The resolution increment in all four detection channels was again imaged on a sparse layer of crimson beads using the four separate detection channels. The recombination of the four images was done using either mosaic-like stitching or large-scale addition of overlapping frames as previously illustrated in figure 3.3. Notice the distinct rhombus-shaped stitching pattern of the first scanning scheme. In the four detection channels a fivefold resolution improvement was generally obtained with the features imaged on the scale of 35 nm full width at half maximum (FWHM). The powers used were not optimised for best resolution but rather for good resolution while limiting the induced bleaching. The second scanning scheme, which was performed with a four times smaller pixel dwell time, provided similar resolution and signal. It is, however, exposed to the risk of compromising the resolution gain due to drift or residual errors in the offsets. Averaged cross-correlation of the detection channels minimised the recombination errors. Using this approach offset values that vary by less than 5 nm (when scanning with a pixel size of 20 nm) in one hour were obtained (appendix B.3). As expected, no asymmetries, which could be attributed to molecular orientation effects or polarised excitation, were observed and all detection channels displayed similar detection count rates.

These observations give confidence in the alignment of the system regarding SWP position, beam quality, polarisations, stability, and detection. In figure 3.7 the resolution improvement was tested in all four channels over the entire field of view (FOV) of approximately $80 \times 80\ \mu m^2$, by taking images using STED and confocal microscopy of tubulin in mam-

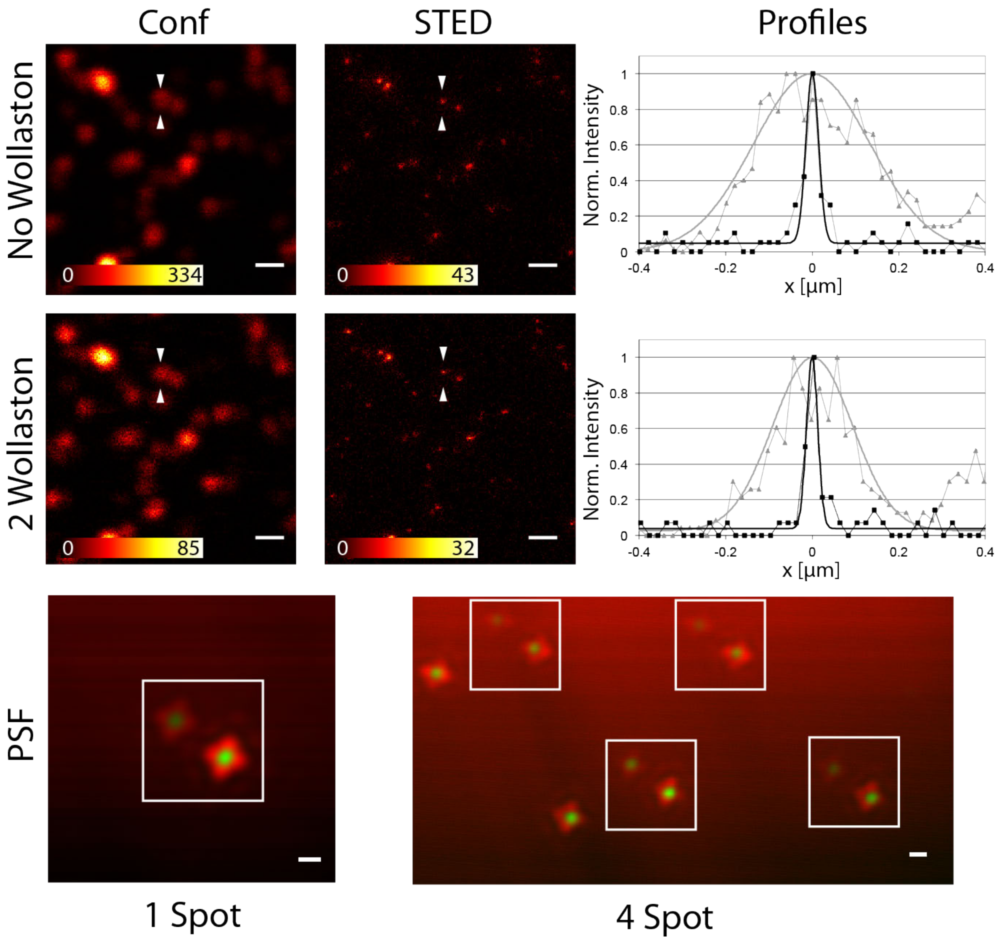

Figure 3.5.: Comparison between signal with (centre row) and without stack (top row) of two Wollaston prisms. The signal including the Wollaston stack was selected from one of the four detection channels. The same fluorescent beads were measured using confocal (left) and STED (centre) microscopy. Right: Line profiles through the same bead, indicated by white arrows, are given for confocal (black squares) and STED (white squares) recordings. Gaussian fits for confocal measurements give FWHM values of 316 ± 11 nm (no Wollaston) and 217 ± 10 nm (2 Wollaston). Gaussian fits of STED measurements give 35 ± 2 nm (no Wollaston) and 30 ± 2 nm (2 Wollaston). Bottom row: The illumination fields were scanned over the same surface of gold beads and the scattered scattered light collected for single-spot and $m = 4$ parallelisation. The same two nearby gold beads are fourfold multiplied in the expected Rhombus-like pattern with no evident change in shape. For the fluorescence recordings approximately fourfold laser intensities were used for both wavelengths and the recordings were taken at 200 µs pixel dwell time and 20 nm pixel size. STED and single-spot recordings were taken first. Varying brightnesses between single-spot and parallelised scans can result from bleaching in individual scans as well as misalignment after changing between single- and multispot modes. Single-spot scans were recorded first. Scale bars: 500 nm.

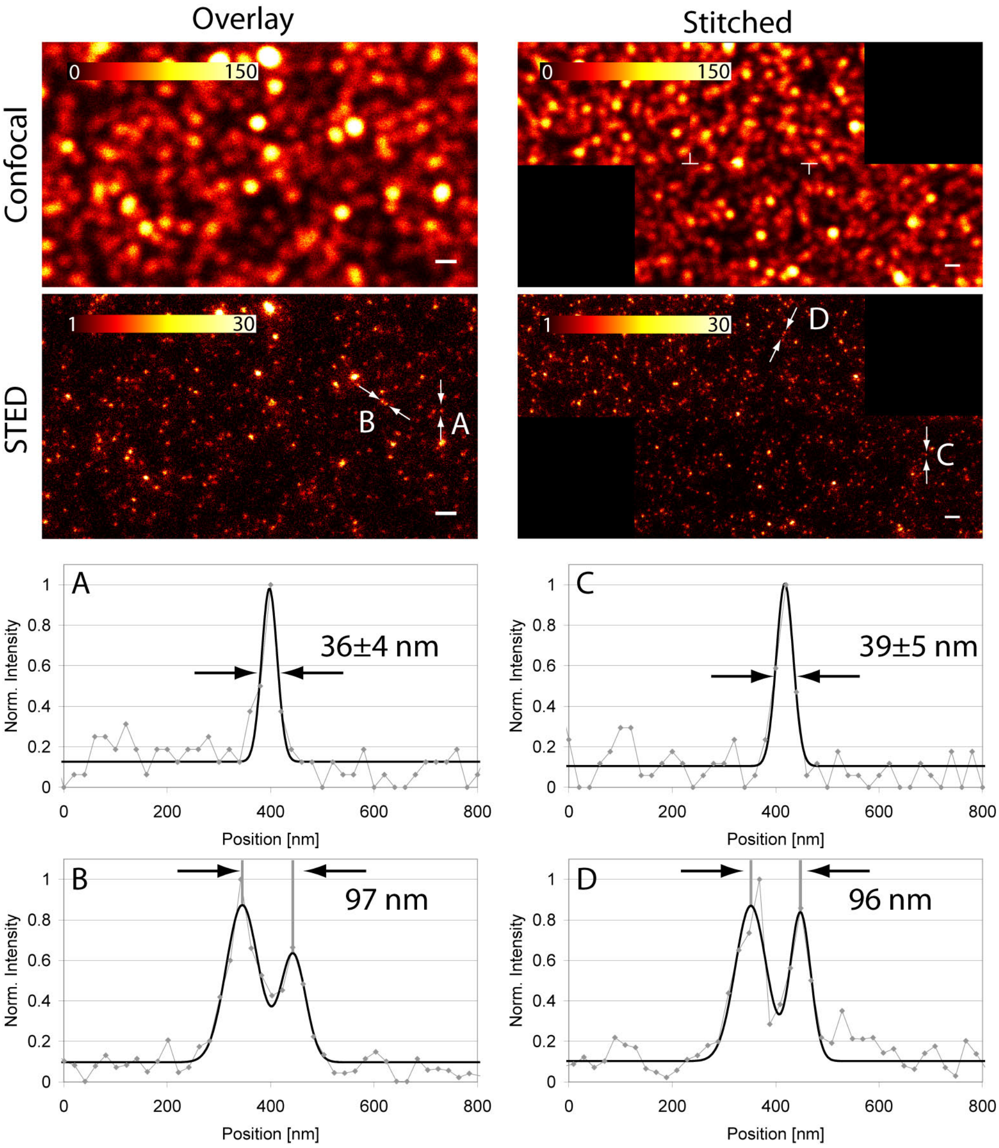

Figure 3.6.: Fluorescent beads measured using parallelised confocal (top) and STED (second row) by either adding overlapping frames (left) or stitching non-overlapping frames together (right). Scale bars: 500 nm. Both scanning schemes offer a fourfold faster acquisition of super-resolving STED microscopy. Bottom: Line profiles and gaussian fits across the beads indicated by the white arrows above. Profiles A and C show profile across single 20 nm beads with similar resolution. Profiles B and C show profile across two beads separated by $\sim$ 100 nm. All images represent raw data and were obtained using pixel dwell times of 50/200 µs (overlay/stitched) and a pixel size of 20 nm.

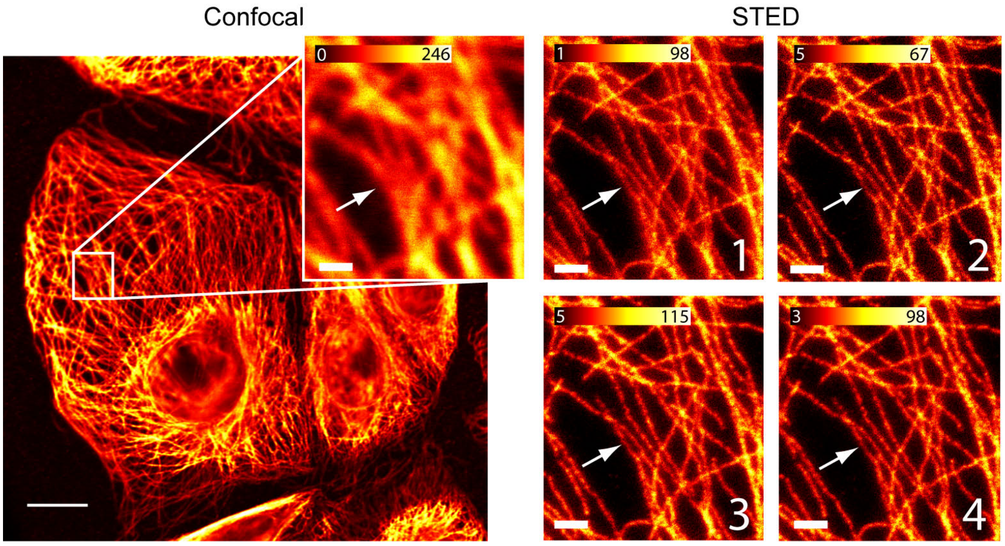

Figure 3.7.: Left: Confocal overview and magnified region (inset) of KK114-labelled tubulin strands in a fixed mammalian (PtK2) cell. Right: Magnified STED images of the four parallelised detection channels 1-4, each corresponding to the confocal region. Note that all STED channels show identical features and that four parallel tubulin fibres (arrows) can be observed using STED which cannot be resolved using confocal microscopy. The confocal images have been recorded using one of the detection channels. The other three channels provide similar images (not shown). All images represent raw data and were obtained using a pixel dwell time of 100 µs and pixel size of 20 nm. Scale bars: 1 µm / 10 µm (Magnifications/Overview).

malian (PtK2) cells. A significant reduction in signal or resolution was not observed towards the image border. The different channels show very similar images and resolution and are shifted laterally in the rhombus-like shape as expected. This can be seen more obviously in figure 1.1, shown in the introduction section. Four parallel tubulin filaments can be clearly distinguished in the four STED images but cannot be resolved using confocal microscopy. Minor variations are always expected due to the multiple scanning and potential bleaching of each recording and differing detection efficiencies.

3.3.2 Speed increase through parallelisation

To test the speed-increasing capabilities of the setup compared to a conventional single-spot STED, an area of $5.8 \times 4\ \mu m^2$ of vimentin in PtK2 cells, immunolabelled with the organic dye KK114 [49], was scanned using STED and stitching the four channels together (Fig. 3.8). The individual frames ($5.8 \times 4\ \mu m^2$) were then recombined by stitching, resulting in an effective scanning area of $11.6 \times 8 \mu m^2$. A second single large scan was done using only a single beam and the same region identified. The same features were detected with similar resolution as in the stitched image. Minor discrepancies were most probably due to previous bleaching. Overlapping of individual channels can be minimised by carefully controlling scanning angle and area, but small errors may still occur in the border regions if stitching offsets are not carefully calibrated and stability guaranteed (see appendix B.5). Multiple scanning in the bordering region can also increase bleaching and lead to (bleaching) artefacts in this region.

Scanning speed increase was also achieved using the second scanning approach by overlaying four large frames of fixed PtK2 cells with Atto647N-labelled tubulin after adding an offset in each of the channels at a dwell time of 50 µs and compared it to a single image taken at 200 µs (Fig. 3.9). The images gave comparable resolution and signal as a single frame at four times longer dwell time. The difference of this approach is that recombination errors are spread across the entire image and no longer restrained to the stitching borders. The offsets can then be directly determined by the images themselves as shown in appendix B.3 (Fig. B.4) given that sufficient photons are collected. For recombining channels using predetermined offsets, the stability of the system needs to be guaranteed. In figure B.5 the offsets between the individual channels were measured with respect to time. It can be clearly seen that the offsets Ch1–Ch2 (offset between channel 1 and channel 2) and Ch3–Ch4 are more stable than Ch1–Ch3 or Ch1–Ch4, clearly indicating that the stability depends on the time interval required for two foci scanning the same point in the focal plane. Nevertheless, the offset deviated by less than the pixel size of the measurement (20 nm). Offsets are, however, never exactly integer multiples of the pixel size which encourages a finer resampling before recombination. Beside the requirement of either sufficient photons or a high stability, another disadvantage of the overlay scheme is that depending on the scanning area, the non-overlapping region can represent a major proportion of the image, which reduces the parallelised area and thus the gain in recording speed. Figure 1.1 is also recorded using this scheme and obtained a decrease in acquisition time of factor 3.32 (instead of 4) due to non-overlapping bordering regions. As previously mentioned, larger FOVs can also be recorded and compiled using the stitching approach by addressing an array of scanning

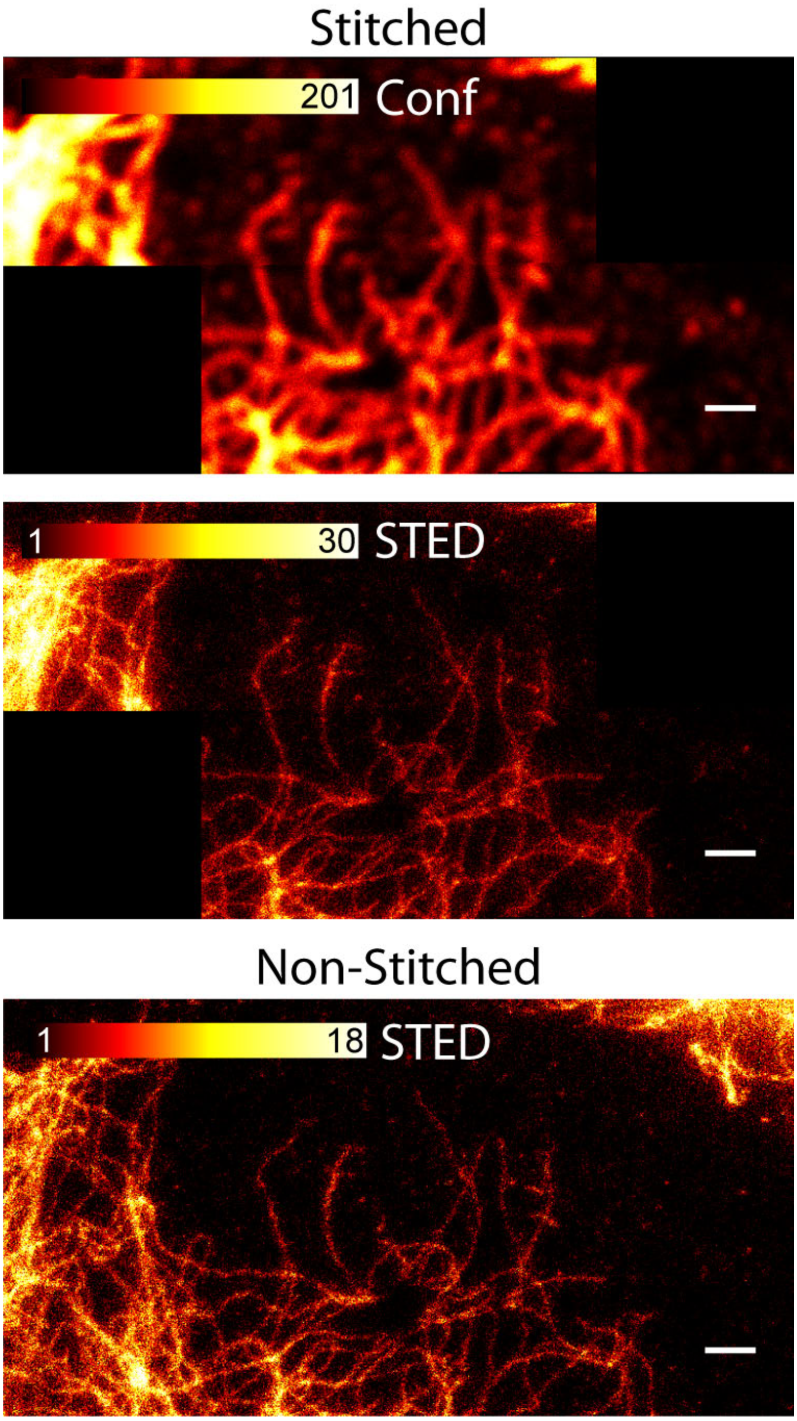

Figure 3.8.: Confocal (top) and STED (centre) images of KK114-labelled vimentin fibres in mammalian (PtK2) cells using a stitched scanning scheme. Note the Rhombus-like stitching pattern. To avoid overlapping of frames, overlapped regions were considered only once. Bottom: A large single channel STED image recorded after STED and confocal stitched images is shown for comparison. The other detection channels show similar images (not shown). No significant disparities between stitched and single frames images can be observed when following individual vimentin fibres along multiple frames. All images represent raw data and were obtained using a pixel dwell time of 20 µs and pixel size of 20 nm. Scale bar: 1 µm.

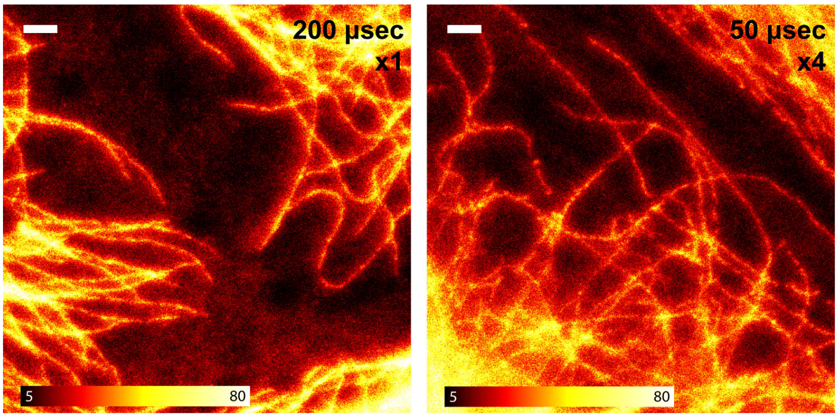

Figure 3.9.: Comparison of single STED image (left) at 200 µs pixel dwell time of the first spot passing the sample (to avoid comparing a bleached image) and by adding the four detection channels at a pixel dwell time of 50 µs (right) of Atto647N-labelled tubulin in PtK2 cells. Scale bars: 1 µm. All images represent raw data and were obtained using a pixel size of 20 nm.

positions as demonstrated in appendix B.7.

In brief, four times faster scanning capabilities of STED were demonstrated with respect to single-beam scanning and acquisition. Importantly, using this configuration, parallelisation can be scaled up to more than four excitation and STED beams and the acquisition rate can be increased accordingly using the scanning schemes demonstrated here.

3.3.3 Multicolour and chromatic aberrations

It was demonstrated that the proposed parallelised STED scheme works for a single excitation/STED wavelength combination. It relies on the birefringence dispersion of the crystal used in the segmented waveplate. Birefringence dispersion of the Wollaston prisms has so far been neglected. The proposed STED design decouples fluorescence using a single band bandpass filter in reflection and potentially allows for multicolour STED nanoscopy by either excitation multiplexing (and mega-Stokes shift dyes), temporal distinction, *e.g.* lifetime [13], or using photochromic molecules [26]. In order to extend parallelised easySTED to multiple colours the recursive feature of segmented waveplates of full and half-wave retardations is exploited, leading to doughnut and point-like focal diffraction pattern depending on the wavelength as shown in figure 3.10. It was decided to choose the second wavelength at 510 nm, which still provides reason-

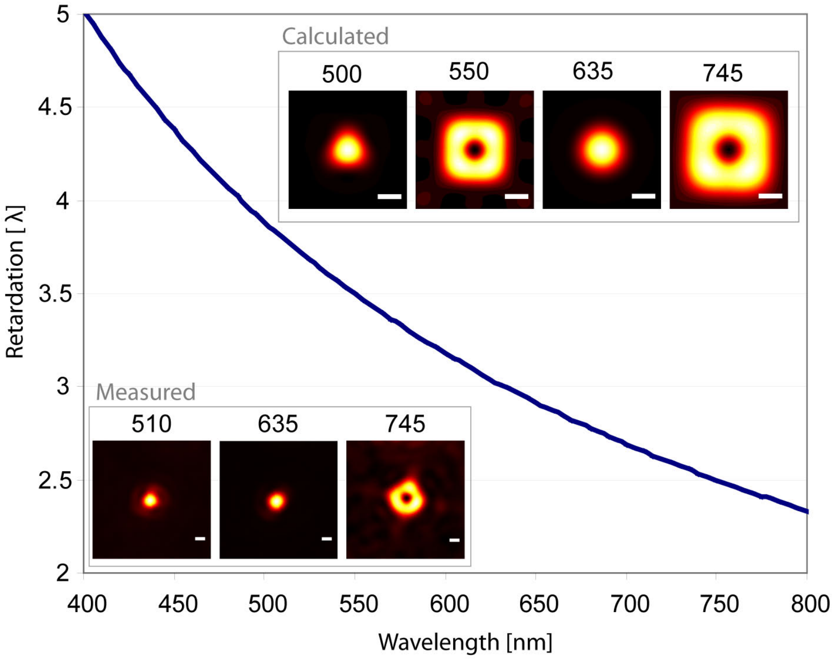

Figure 3.10.: Retardation in wavelength between ordinary and extraordinary polarisation for a quartz crystal manufactured to have a retardation of 2.5λ at $\lambda = 750$ nm. *Insets*: Calculated and measured PSFs for different wavelength demonstrating the recursive feature of the SWP of producing point-like and doughnut-shaped beams.

able point-like excitation while being a good excitation wavelength for the Mega-Stokes Shift dye Dyomics521XL. The dye spectra, laser lines and detection bands of the optical setup are shown in figure 3.11. The potentiometric dye Di-8-anepps was also successfully tested for STED by exciting with a 495/20 band selected from the supercontinuum (not shown).

For quartz the birefringence $b(\lambda) = n_E(\lambda) - n_O(\lambda)$ between the wavelengths 633 nm and 745 nm differs by $\sim$ 1.18% (appendix B.1), which directly translates to the splitting angle. Using 20" Wollaston prisms in combination with a 100 mm scanning lens, a 200 mm tube lens and a 100× objective lens in the given case leads to multispots nominally separated by 5.81 µm. The birefringence dispersion of 1.18% thus should translate to a difference in splitting distance of 69 nm per Wollaston prism. Each excitation spot should therefore be effectively separated from its corresponding STED beam by approximately 35 nm. A detailed description of the splitting action of a Wollaston prism is given by SIMON [79] accounting for

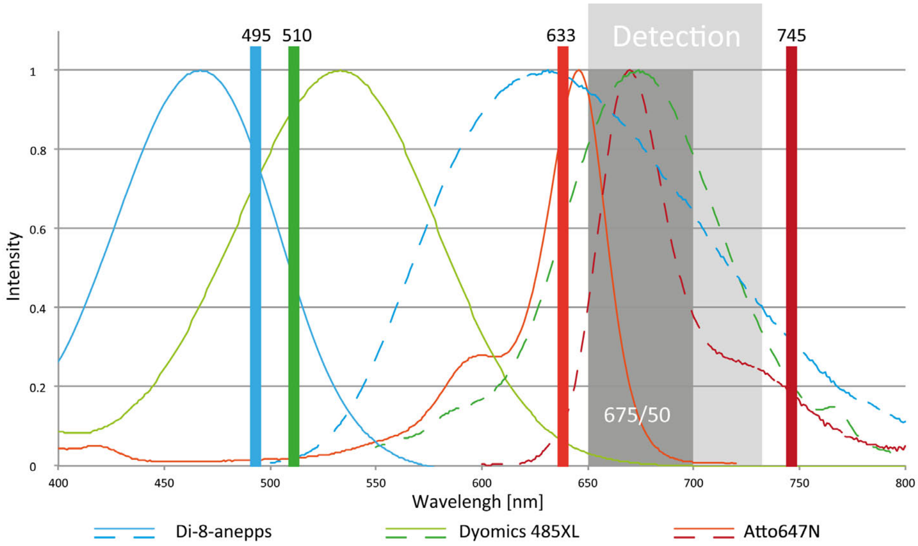

Figure 3.11.: Excitation and emission spectra of Di-8-anepps (blue), Dyomics521XL (green) and Atto 647N (red), including the wavelengths of the designed setup at 495 nm, 510 nm, 633 nm, 745 nm, and the detection filter (675/50) most commonly used in this thesis. The detectable emission spectrum is limited by the custom-made bandpass filter used in reflection (see setup in figure 3.2).

angles of incidence and various aberrations induced for a non-collimated beam and could explain the observed and unexpected non-symmetrical splitting by the Wollaston prisms (not shown).

As seen from the STED images in the previous section, birefringence dispersion can be neglected for a four-spot STED setup operating at a wavelength combination of 633 nm for excitation and 745 nm for STED and using quartz based Wollaston prisms even after two splitting actions at an angle of 45°. For green excitation at 510 nm and STED at 745 nm, however, the birefringence dispersion of $\sim$ 3.33 % can also no longer be neglected for the same splitting angle (appendix B.1). As expected, for 20" Wollaston prisms made of quartz and used in this setup, an effective difference in the splitting angle was observed between excitation wavelengths and STED (745 nm) of 193 and 201 nm for $\lambda_{exc} = 510$ nm, compared to 69 and 76 nm for $\lambda_{exc} = 633$ nm in figure 3.12 for the two different Wollaston prisms[1]. In order to extend parallelised multispot STED to multicolour by excitation multiplexing a combination of prisms is thus required

---

[1] The difference in splitting angle is most likely caused by different prism angles at manufacturing

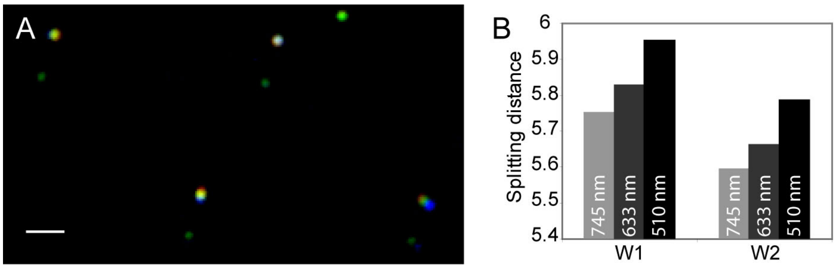

Figure 3.12.: Left: Gold beads scanned with a $m = 4$ parallelised multispot illumination field using a stack of two 20" Wollaston prism and wavelengths at 510 nm (blue), 633 nm (green) and 745 nm (red). Right: The induced averaged splitting distance in the focal plane for 510 nm, 633 nm and 745 nm is plotted for horizontal (Wollaston 1) and diagonal splitting at 45°(Wollaston 2). The splitting distance increases for 633 and 510 nm with respect to 745 nm by 76 nm and 201 nm respectively for prism 1. Prism 2 induces a difference of 69 nm and 193 nm for 633 nm and 510 nm respectively. Overall the observations are in good agreement with the predicted values of equation equation B.1. Scale bar: 500 nm.

that effectively acts as an achromatic prism as shown in figure B.2 (Patent number: DE19611037a). In addition to the birefringence of the Wollaston prisms, the given setup and tube lens / objective lens / microscope stand combination was subdued to a 0.43% lateral chromatic aberration for 510 nm with respect to the 745 nm STED wavelength (Fig. 3.13), most probably due to insufficient correction over this spectral range. Allowing for a 50 nm offset tolerance between the individual beams, beam-scanning with a single spot at $\lambda_{exc} = 510$ nm and $\lambda_{STED} = 745$ nm is only possible up to an area of 22×22 µm^2. Analogously, the lateral chromatic aberration at 633 nm with respect to 745 nm is only 0.1% which translates to a maximum scanning area of 102×102 µm^2, which is largely sufficient and beyond the maximal scannable area of a beam scanner.

This chromatic aberration can be reduced with specially designed microbjectives and beam-scanning microscope stands and does not represent a fundamental issue. Because a reduction in signal could not be observed for the 633/745 combination, the lateral chromatic aberrations are believed to be sufficiently corrected for at these laser wavelengths. The axial alignment of the beams solely depends on the micro objectives used. For the objectives used in the present system they are shifted by $100 - 200$ nm (Fig. 3.13 E–F), which is well within the $400 - 500$ nm axial resolution and can hence be neglected. When using three-dimensional beam-shaping devices [67], however, the inability of the single-fibre system to accurately co-align the different wavelength axially may reduce the signal

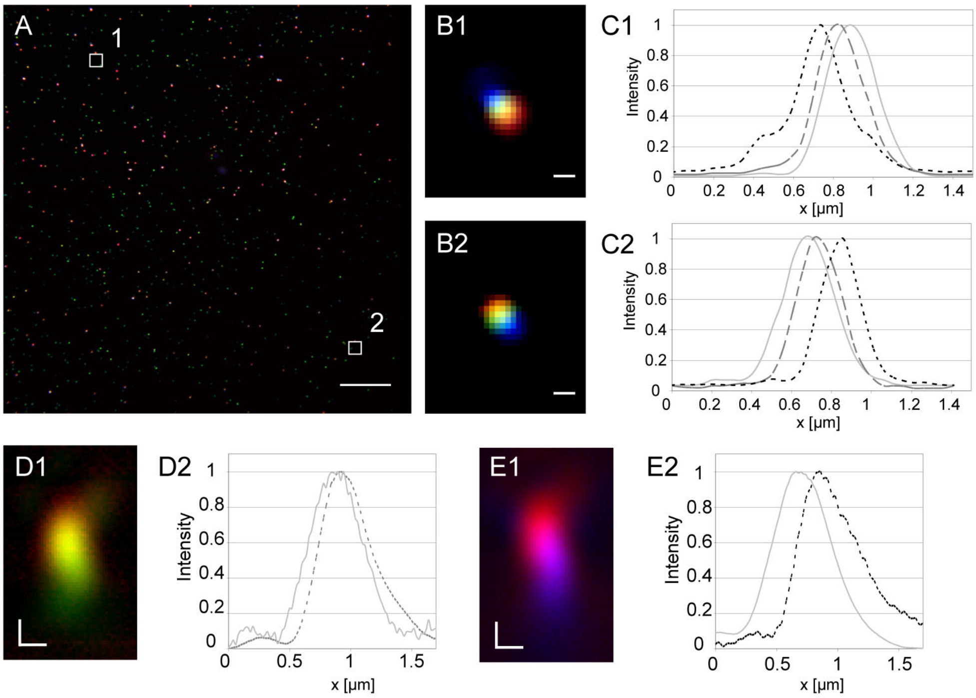

Figure 3.13.: (A) Scanning gold beads without SWP and without Wollaston prisms with $\lambda = 745$ nm (red), 633 nm (green) and 510 nm (blue) over a $\sim 80 \times 80$ µm^2 region. Zooms of two selected regions 1 (B1) and 2 (B2). Smaller wavelengths clearly display a lateral offset. The regions are separated in the focal plane by 76.01 µm. (C1,2) Diagonal line profiles from top left to bottom right of regions 1 and 2 of 510 nm (striped black), 633 nm (striped dark grey) and 745 nm (light grey). Combining the separation of the regions with the dispersion obtained from the line profiles results in a lateral chromatic aberration of 0.43% for 510 nm and 0.1% for 633 nm with respect to 745 nm. (D1) Scanning gold beads in *xz* direction for 745 nm (red) and 633 nm (green) and the corresponding line profile in axial direction (D2). (E1) Scanning gold beads in *xz* direction for 745 nm (red) and 510 nm (blue) and the corresponding line profile in axial direction (E2). The peak intensities of the 510 nm and 633 nm wavelengths are axially displaced by $\sim$ 175 nm ($\lambda = 500$ nm) and $\sim$ 80 nm ($\lambda = 633$ nm) with respect to the STED wavelength ($\lambda = 745$ nm). Scale bars correspond to 10 µm (A) and 200 nm (B,D,E).

and increase bleaching of the system.

Multicolour Imaging

The above-described multicolour scheme has the potential of producing multicolour STED images in combination with achromatic Wollaston prisms. The various dispersion effects at large wavelength differences make parallelised multicolour easySTED more challenging to implement. Before implementing the novel type of achromatic Wollaston prisms mentioned above, multicolour easySTED using a single spot is first demonstrated. Mega-Stokes shift dyes compatible with STED are relied upon in order to perform multicolour imaging by excitation multiplexing. The requirement are a low cross-talk between the individual dyes and bleaching-resistance to the strong STED laser field. Imaging Dyomics521XL labelled tubulin strands together with KK9445 (spectrally similar to Atto647N) labelled vimentin, produces clearly distinguishable fibrous structures when imaging without STED laser (Fig. 3.14). By STED nanoscopy, however, only KK9445 shows a nice increase in resolution (Fig. 3.14 E–F), while the increase in resolution of Dyomics521XL is difficult to spot although a good "STED-effect", *i.e.* decrease in fluorescence signal due to the reduction of the fluorescent volume, is observable (Fig. 3.14 C,D,G,H). Furthermore, the observed cross-talk in STED reduces the contrast of the Dyomics signal (Fig. 3.14 D). In order to demonstrate that indeed an increase in resolution is obtained, two line profiles across tubulin fibres were plotted in figure 3.14 (I1) and (I2). FWMH values of 292 ± 18 nm (profile 1) and 234 ± 7 nm (profile 2) were obtained by gaussian fits in confocal images. These values were reduced to 98 ± 14 nm (profile 1) and 148 ± 14 nm (profile 2) in STED recordings. Although providing obviously lower resolution improvements for Dyomics than for Atto647N and similar dyes, these multicolour images demonstrate that (provided the right fluorescent dyes) multicolour parallelised (multispot) STED is feasible. It furthermore is a first demonstration of multicolour (single fibre) easySTED. To summarise, the following dyes were successfully tested with the designed setup and available wavelengths: Atto647N (633/745), KK9445 (633/745), KK114 (633/745) and Dyomics521XL (510/745) (all coupled through primary and secondary antibodies to either vimentin or tubulin in PtK2 cells), the potentiometric dye Di-8-anepps (495/745) in the living skeleton muscle cells and the intercalating DNA dye TOTO-1 (633/745) in nuclei of rat embryonic fibroblast cells.

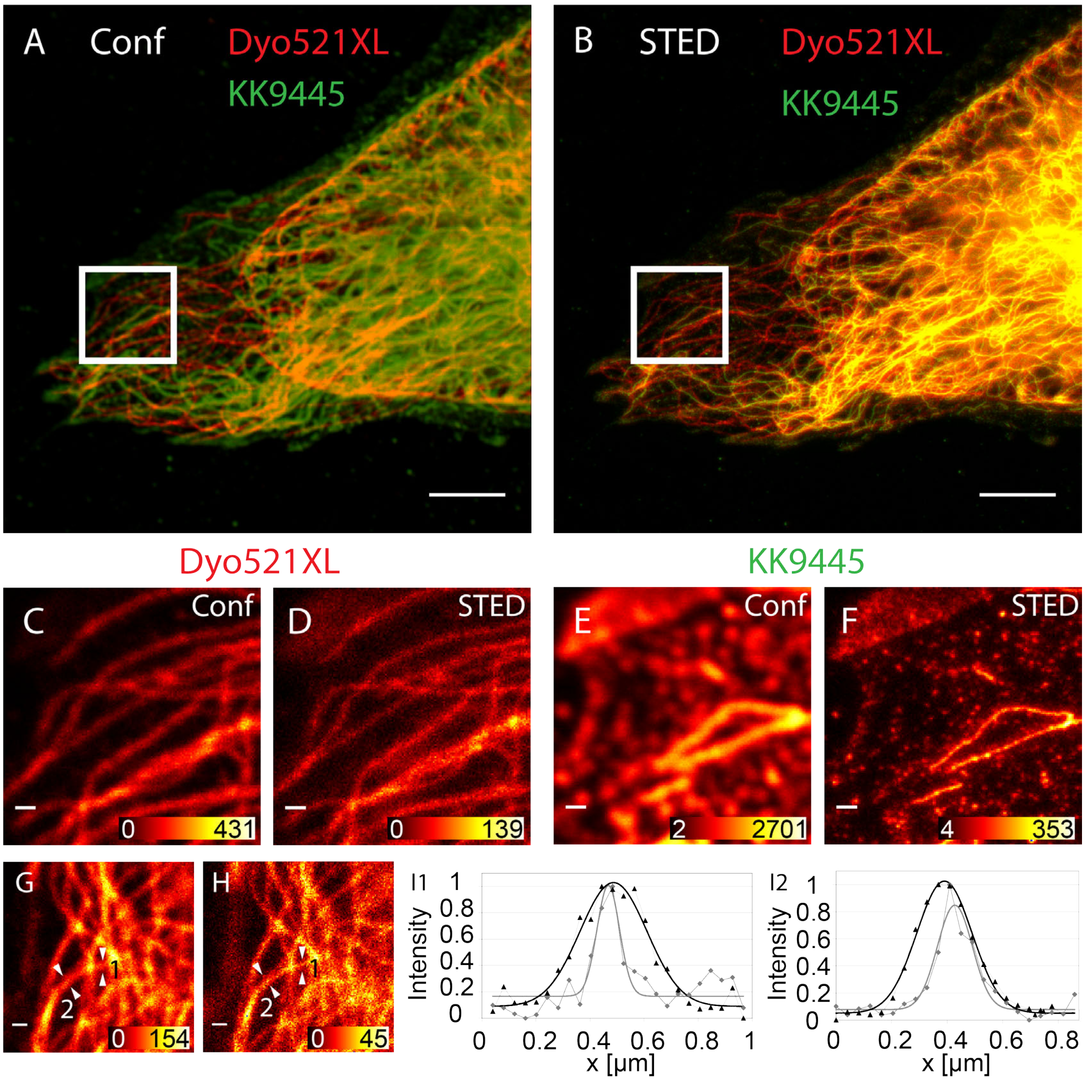

Figure 3.14.: Multicolour imaging by excitation multiplexing of Dyomics521XL (red) and KK9445 (green) using confocal (A) and STED (B) microscopy. Zooms of the individual recordings of Dyomics521XL (C-D, G-H) and KK9445 (E-F) are shown for both confocal (C,E,G) and STED (D,F,H) modes. (C–F) represent the zooms of images (A–B). Line profiles from (G–H) at positions 1–2 are shown for confocal (black) and STED (grey) recordings and their corresponding gaussian fits with FWHM values of 292 ± 18 nm (confocal) and 98 ± 14 nm (STED) in profile (I1) and 234 ± 7 nm (confocal) and 148 ± 14 nm (STED) in profile (I2). Scale bars: 5 µm (A-B) and 500 nm (C-H).

4

STED - Coincidence Analysis (CCA)

So far multiple detectors have been used to address different positions in the focal plane, *i.e.* parallelisation, which offers a solution for reducing the long recording times for large FOVs in targeted nanoscopy. As mentioned earlier, RESOLFT/STED is an ensemble technique that can resolve structures with diffraction-unlimited resolution, but cannot directly count the number of emitters from the recorded signal. The following chapter is introducing a new detection concept to STED that is based on the counting of coincident (fluorescence) photons. A four-detector detection setup is presented and the feasibility for counting emitters in STED is demonstrated.

4.1 Introduction

It is well-known that besides the recorded intensity (number of photons), the temporal information (time of arrival) can be crucial in STED nanoscopy, especially for CW-STED where the time-information is directly linked to resolution [87] (as briefly explained in section 2.5). In STED-FCS the signature of the intensity-fluctuations yields information about the diffusion of molecules through the effective fluorescent STED volume [45]. In a different experiment cross-correlation of the signal of overlapping detection PSFs by at least three separate point detectors arranged in close proximity was used to record diffusion traces inside a sub-diffractional volume [71]. Here the fluorescence is collected from a single excitation and detection volume and split onto four single-photon counting detectors. Due to the quantum phenomenon of photon antibunching exhibited by single-photon emitters such as fluorescent dyes, a single molecule cannot emit more than one photon per laser cycle for a short-pulsed laser source. By statistically analysing the number of recorded coincident photons per laser cycle, one can deduce the number of emitting molecules by

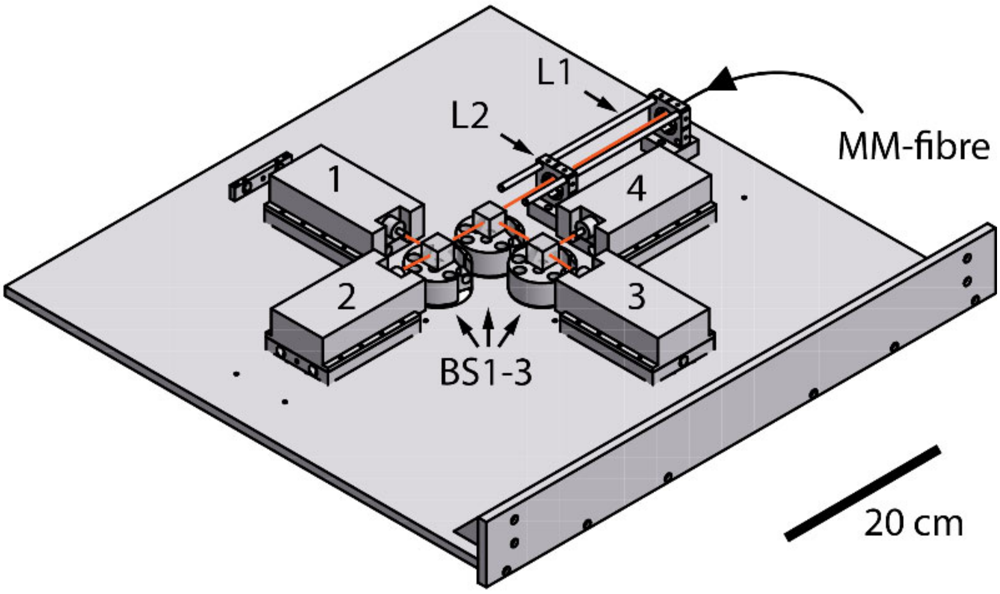

Figure 4.1.: Detection unit with $m = 4$ detectors for coincidence analysis: the fluorescence originating from the multimode fibre (MM-fibre) is expanded using an $f = 20$ mm lens (L1), refocused using a $f = 200$ mm lens (L2) and split equally into four beams by three neutral 50% beam splitting cubes (BS1–3). Each beam is focused onto a different single-photon counting avalanche photodiode (1–4). The beam paths are indicated by orange lines. The APDs can be displaced in the direction of the incident beam path and the individual beam splitting cubes can be tilted and rotated in all spatial direction. The fibre output, collimating lens and focusing lens can all be displaced in direction of the optical path. The focusing lens is additionally mounted in a *xy* adapter for controlling the undeflected beam.

fitting the model probability distribution given by equation 2.8 in section 2.5.1 onto the photon distribution. Nonetheless, even this so-called coincidence analysis (CCA) by four detector will eventually reach saturation at high numbers of emitters (where estimation of the number of emitters is no longer possible). CCA and STED therefore complete one another because the effective volume, from which fluorescence is allowed, can be gradually reduced (by varying the switching power). This in turn reduces the number of molecules in focus and allows CCA of denser samples.

The following sections demonstrate that CCA has the potential of counting single molecules in ensembles and sub-diffractional RESOLFT volumes without prior calibration and only based on the temporal photon distribution.

4.2 Setup

By removing the stack of Wollaston prisms the parallelised STED setup in figure 3.2 can be easily converted into a regular easySTED setup [68]. Instead of being focused onto an APD the fluorescence was focused into a multimode fiber (NA: 0.275, Core Ø: 62.5 µm, M31L01, Thorlabs, USA) and transmitted to the coincidence analysis (CCA) detection unit (Fig. 4.1). Inside the CCA detection unit the collected fluorescence is first collimated using a $f = 20$ mm lens and then refocused using a $f = 200$ mm lens onto 4 single-photon counting modules (SPCM-AQRH-13/15, Perkin-Elmer, USA). Using three conventional 50/50 beam-splitting cubes the light is evenly split into four separate beams and focused onto four detectors as illustrated by the red beam paths in figure 4.1. All optical paths have similar length to prevent wrong identification of coincident photon events[1]. For temporal alignment purposes all detectors can be displaced in the direction of the optical path. The individual beam-splitter cubes can be rotated in all spatial direction and the focusing lens can additionally be displaced laterally. The fluorescence signal was processed by a four-channel USB-controlled TCSPC module (HydraHarp 400, PicoQuant, Germany) and correlated using the output synchronisation port of the excitation source. The signal of one of the four detections ports was additionally used for imaging purposes and to guide the excitation beam to the feature of interest. Additional synchronisation signals (line start/stop clocks and frame clock) from the FPGA board (also controlling the beam-scanner) were necessary for direct two-dimensional (2D) image acquisition with the commercial SymPhoTime software (PicoQuant, Germany). Data evaluation with a home-build MATLAB routine written by ANTON

---

[1] In the present $\sim$ 18 MHz laser system consecutive pulses are separated by $>$ 10 meters.

Kurz[1]. The bootstrapping method was employed for analysing the homogeneity of the statistical distribution and to remove outliers. Only 75% of the laser cycles of a given time interval are thereby fitted to the model. By iteratively selecting different 75% of the total distribution, the robustness of the method can be assessed[2]. Samples were prepared as described in sections 4.3.1 and 4.3.2.

Different recording approaches can now be taken: (i) a *pick* & *destroy* (PnD) approach in which the non-scanning illumination beams are placed directly onto a feature of interest, *e.g.* DNA origami, or (ii) a scanning approach for position-depended coincidence analysis. The scanning approach could also be used to create a time- and space-averaged CCA recording of a surface or volume and is useful for studying fixed quasi-2D fluorescent films which may otherwise bleach.

The PnD approach was first employed for collecting a maximum number of coincident photon events. Two-dimensional overview scans of a sparse distribution of fluorescent probes are scanned with appropriate pixel sizes ($\sim 0.5\times$ STED resolution) in order to accurately localise the positions of the probes. These positions are then addressed (*pick*) and the signal recorded using the TCSPC module until the probe bleaches down to background level (*destroy*). Bleach steps thereby help to act as controls for the results gained from CCA [51,86]. For circumventing photobleaching, problematic for CCA, photon statistics were next recorded for dyes in solution with an immobile beam, which ensures a continuous exchange of dye inside the effective fluorescent volume. Finally photon statistics of 2D recordings were collected and integrated over hundreds of scanning cycles of the same sparse layer of fluorescent probes. Multi-photon statistics are thereby recorded in each pixel and the increase in resolution can be directly visualised[3]. The STED laser powers employed for studying surface-bound probes were adjusted to obtain a resolution improvement of factor 2, with FWHM values corresponding to the dimensions of the DNA origami used in these experiments. In solution the STED powers could be increased due to effective absence of photobleaching. The following sections show preliminary data recorded by the setup described above (Fig. 4.1).

---

[1] Single-molecule spectroscopy (Herten group), BioQuant, Im Neuenheimer Feld 267, Ruprecht-Karls-Universität, 69120 Heidelberg, Germany

[2] The error bars in figures 4.3,4.4 and 4.5 represent the regions in which 75% of the fits reside.

[3] The PnD method requires that the resolution of the imaging system is determined separately.

4.3 Results

4.3.1 Pick & Destroy

We first imaged and recorded photon statistics of individual 20 nm large polystyrene microspheres filled with crimson fluorophores because of their bright signal (not shown). The unknown number and distribution of encapsulated molecules (which could leads to self-quenching effects due to Förster resonance energy transfer (FRET)), however, encouraged the use of more controllable samples. These were DNA origami conjugated with 36 ATTO647N labels, kindly provided by the Tinnefeld group[1] [69, 80]. The molecules were arranged on the DNA origami such that individual molecules were located > 12 nm apart (in order to prevent FRET) and arranged in three rows separated by ~ 45 nm, effectively spanning over an area of $\sim 90 \times 140\,\text{nm}^2$ (see illustration in Fig. 4.2 inset). For some sample preparations the appearance of bright fluorescently active debris was observed (within tens of seconds) at even relatively low powers (for STED). It was suspected that photochemical reactions were induced by the accumulated energy of the immobile STED beam[2]. Eventually, the DNA origami was prepared on poly-L-lysine (PLL)-coated coverslip, which showed no such effects. The origami solution was deposited on the PLL surface for 10 minutes, rinsed for 10 seconds with distilled water and blown-dried. The origami surface was embedded in reducing and oxidising system (ROXS) for photobleaching reduction [44,88] and sealed with nail polish. Furthermore, the STED beam average power was kept low, 1.8 mW at 18.45 MHz in the backfocal plane. At this power an approximately twofold increase in resolution is obtained as shown in figure 4.2, while possible photobleaching due to the STED beam (which would reduce the collected photon statistics) is kept at a minimum. The excitation power was adapted for best tradeoff between signal and bleaching.

In Figure 4.3 PnD of a DNA origami was first done using excitation only, showing both the overall signal of the bleaching sample as well as the corresponding estimated number of emitters by CCA for time bins of 0.54 seconds. The estimated number of molecules is only dependent on the multi-photon distribution (shown exemplarily for five different times in figure 4.3). The estimated number of emitters by CCA agrees remarkably well with the evolution of the overall signal, and values of up to 20 molecules were obtained at an acceptable error. Some values were still not

---

[1] Tinnefeld Lab, NanoBioSciences, Institute for Physical and Theoretical Chemistry, Technical University Braunschweig, Germany

[2] By recording the PnD signal in intervals (e.g. 10 seconds on, 10 seconds off), the recording time without these artefacts could be increased (data not shown).

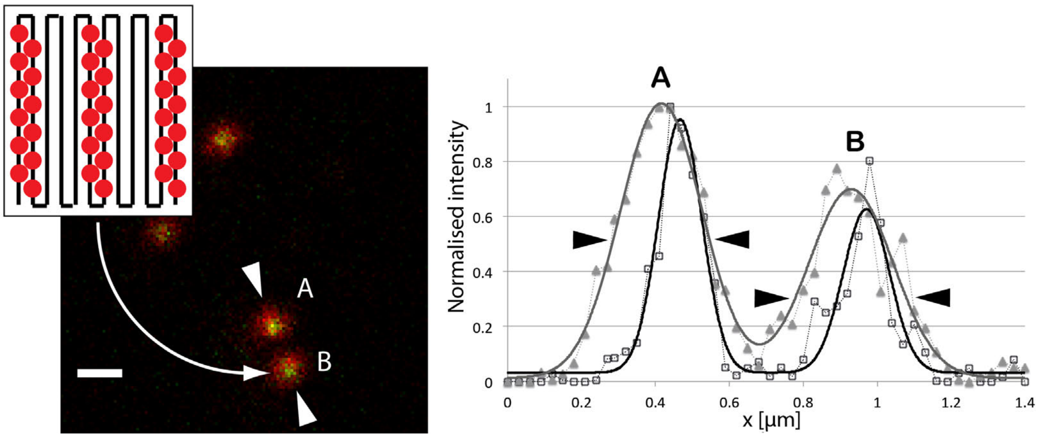

Figure 4.2.: Left: DNA-Origami with 36 Atto647N fluorophores imaged by conventional diffraction-limited point-scanning microscopy (red) and STED nanoscopy (green). Right: Line profiles and corresponding gaussian fits across two DNA origamis (profile across origamis A and B indicated by white arrows) for confocal (grey line/triangles) and STED (black line/squares). The gaussian fits give FWHM values of 262 ± 12 nm (confocal) and 139 ± 9 nm (STED) for origami A and 269 ± 18 nm (confocal) and 149 ± 15 nm (STED) for origami B. Approximately twofold resolution increment is recorded with 1.8 mW average STED laser power in the back focal plane. Inset: Illustration of the DNA origami including three rows of 12 Atto647N fluorphores covering a ∼ 90 × 140 nm area. Scale bar: 500 nm.

correctly fitted by the present algorithm (*e.g.* spike at $t = 6.5$ seconds). When looking at the zoomed region, three distinct intensity levels can be distinguished by bleach (and blinking) steps. The estimated values follow the same step-wise trend, counting one, two or three emitters. When extrapolating the intensity of a single bleach step (background: 2.52 ± 0.81 kHz, first bleach step intensity: 18.91 ± 2.22 kHz (region: 31 − 35 seconds) and peak intensity: 695.8 ± 17.5 kHz), the initial signal would correspond to 42 ± 6 molecules and agree with the maximum of 36 emitters ideally present in the DNA origami. Unfortunately, the multi-photon distribution of the initial (unbleached) origami could not be accurately fitted by the model. Interestingly the molecules coupled to the DNA seem to have varying molecular brightnesses as can be observed by comparing the regions 25 − 30 seconds and 31 − 35 seconds. Ta measured that the variation in molecular brightness of Atto647N molecules is on average ∼ 14.5%, but simulated that this only leads to a small negative bias and no significant change in the estimation error [83]. This variation was not yet accounted for in the present model. Additionally, the estimated normalised molecular brightness p of $(8.4 \pm 0.4) \cdot 10^{-4}$ (not shown) was inferior to the previously estimated $(1.35 \pm 0.1) \cdot 10^{-3}$ measured by Ta using a non-fibre coupled detection. Improving bleaching, detection efficiency and the model will eventually increase the maximal number of detectable emitters and reduce the estimation errors.

Next, the same experiment was repeated with STED in figure 4.4 employing the same power settings as used in figure 4.2. The recorded signal now originates from fluorescent emitters that are confined to sub-diffractional volume. The 36 molecules, conjugated to the $\sim$ 90×140 nm² DNA origami, are suspected to all be confined inside the effective (sub-diffractional) fluorescent volume provided by STED. Longer intervals were chosen to accumulate the necessary photon statistics and compensate for the sightly lower intensity observed in STED. Up to 9 molecules could be estimated by the used algorithm and the estimation values follow a similar trend as the overall intensity. Again, extrapolating of the single bleach step was done (background: 2.32 ± 0.71 kHz, first bleach step intensity: 7.56 ± 1.79 and peak intensity: 209.4 ± 22.3 kHz), and a value of 54 ± 13 molecules derived for the molecules contributing to the initial signal, which overestimates the 36 molecules. The fast bleaching of the DNA unfortunately did not allow an accurate fit to the model distribution for the initial (unbleached) origami. The average normalised molecular brightness $(5.5 \pm 0.2) \cdot 10^{-4}$ gave a lower value than in the diffraction-limited recording and a decreasing trend during acquisition (not shown). Non-perfect zero intensity, or wrong positioning of the laser beam (with respect to the DNA origami) are possible explanations for the inferior brightness, while drift and estimation errors could explain its decrease.

A longer acquisition increases the overall photon statistics and thereby decreases the estimation error. Acquiring photon statistics of a bleaching sample, however, obviously falsifies the results obtained by CCA because the number of emitters is changing over the recording time. Especially for realising scanning STED-CCA, where one wants to extract the number of emitting molecules for each scanning position without bleaching, a tradeoff between sufficient photon statistics and bleaching is therefore necessary. Ta *et al.* simulated that approximately 10000 photons are necessary per molecule for a $20-30\%$ estimation error [83]. Hence, a recording time of 0.542 seconds is necessary (for recording 10000 photons), assuming $p = 0.001$ and a laser repetition rate of 18.45 MHz. The errors ranges of the diffraction-limited recording in figure 4.3 agree with this simula-

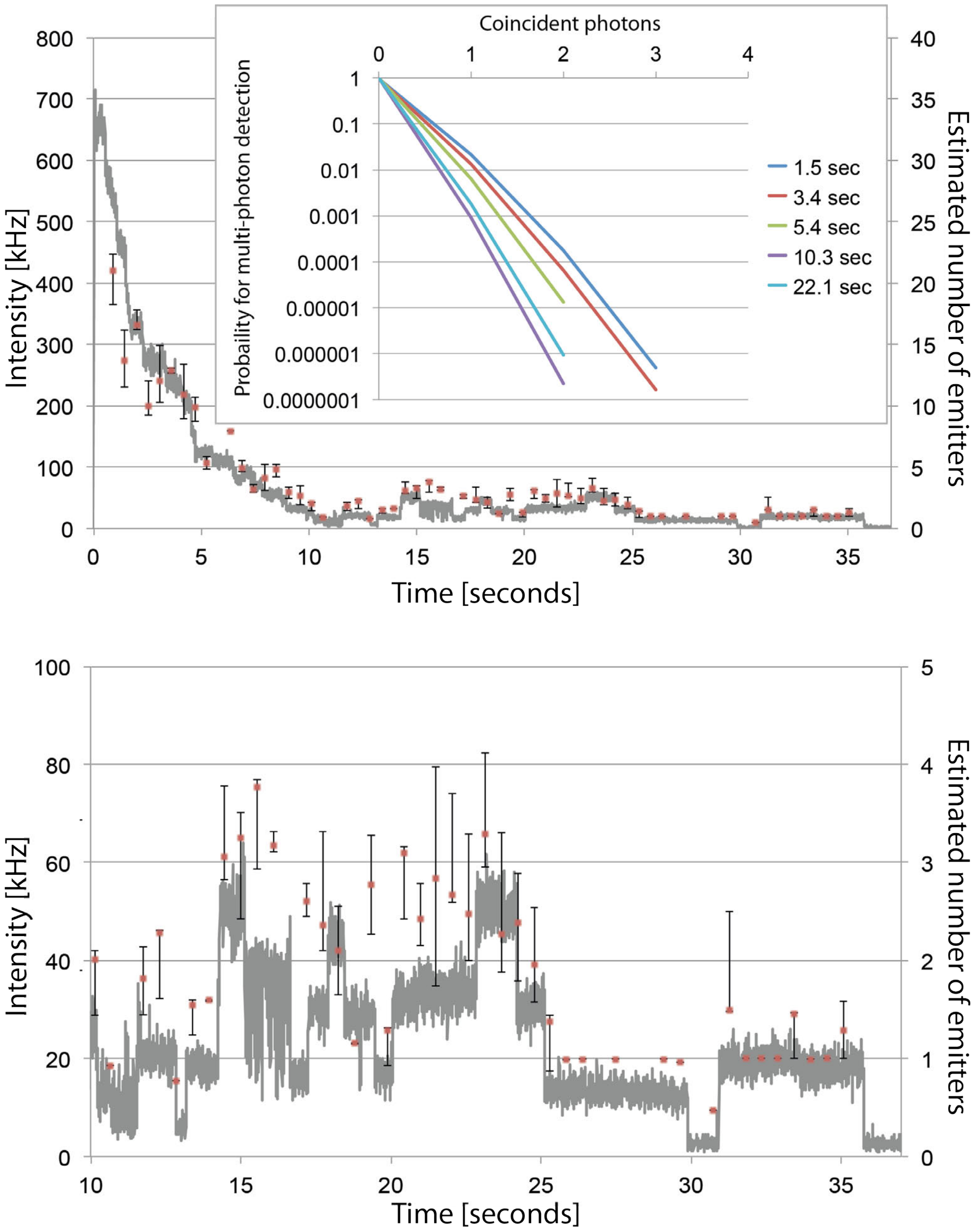

Figure 4.3.: Regular CCA Top: Fluorescence intensity (grey line, 10000 laser cycles binning) and estimated number of molecules by CCA (red squares, 0.54 seconds intervals) of a DNA origami conjugated with 36 ATTO647N labels by confocal microscopy plotted against time. Bleaching occurs until background level is reached. Inset: Multi-photon probability distribution for five different 0.98 seconds intervals centred around the time indicated in the legend. Bottom: Zoomed region showing bleach (and blinking) steps in the intensity as well as estimated number of emitters.

tion[1]. Although ROXS buffer already provides good reduction in photobleaching, more work is still necessary in order to reduce bleaching to a level where the collecting of sufficient photons in STED-CCA is possible.

4.3.2 Solution

Dye in solution was recorded next in a FCS-like manner (constantly exchanging dyes) in order to exemplify the difference between STED-CCA and confocal CCA. Figure 4.5 shows the combined signal as well as the average number of estimated emitters recorded by the four detectors using excitation only (zero STED intensity) or STED nanoscopy. The measurements were performed at a dye concentration of 10 nM, excitation power of 51 µW in the BFP and varying STED lasing powers. A clear reduction in overall signal is observed for STED-CCA compared to regular CCA as expected by the modified Abbe formula in equation 2.3. Exciation by the STED beam alone could be neglected even for relatively high powers (data not shown). Analogously, the estimated number of emitters shows a reduction for increasing STED powers up to 12 mW. At higher values (23.5 mW) an unexpected increase in estimated numbers was observed. This observation could be attributed to either low signal, increased excitation by the STED laser or the non-confocalised detection, which all lead to variations in the multi-photon distribution. Despite giving arguable quantitative result[2], this measurements should act a a proof of principle that the reduced number of emitters in the (reduced) fluorescent STED volume can be counted by CCA.

---

[1] The indicated errors for the estimated number of molecules are derived using the bootstrapping method to evaluate the robustness of the fitting algorithm.

[2] Due to the lack of confocalisation, substantial signal could actually originate from out-of-focus.

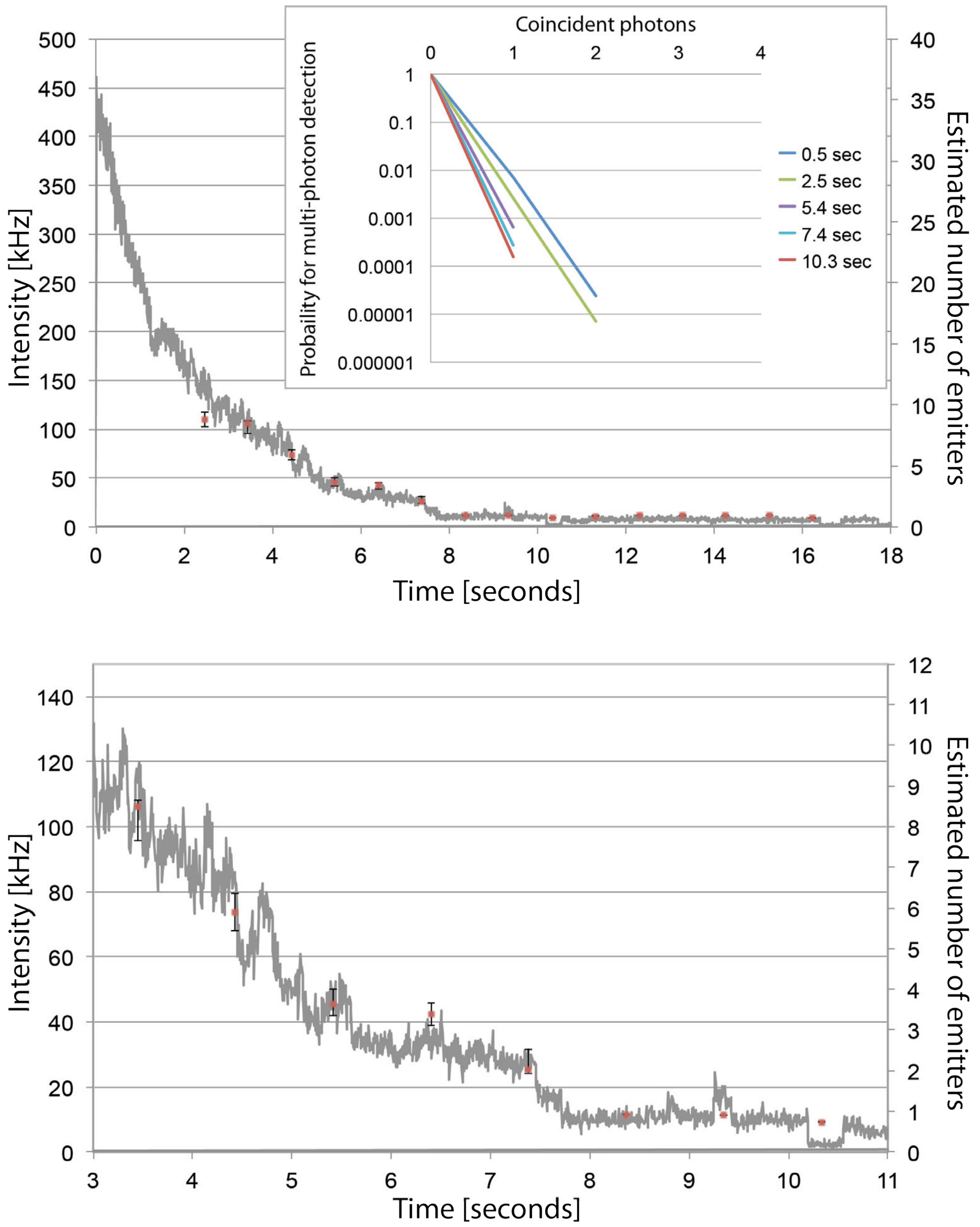

Figure 4.4.: STED-CCA Top: Fluorescence intensity (grey line, 10000 laser cycles binning) and estimated number of molecules by CCA (red squares, 0.98 seconds interval) of a DNA origami conjugated with 36 ATTO647N labels by STED nanoscopy plotted against time. Bleaching occurs until background level is reached. Inset: Multi-photon probability distribution for five different 0.98 seconds intervals centred around the time indicated in the legend. Bottom: Zoomed region showing bleach (and blinking) steps in the intensity as well as estimated number of emitters.

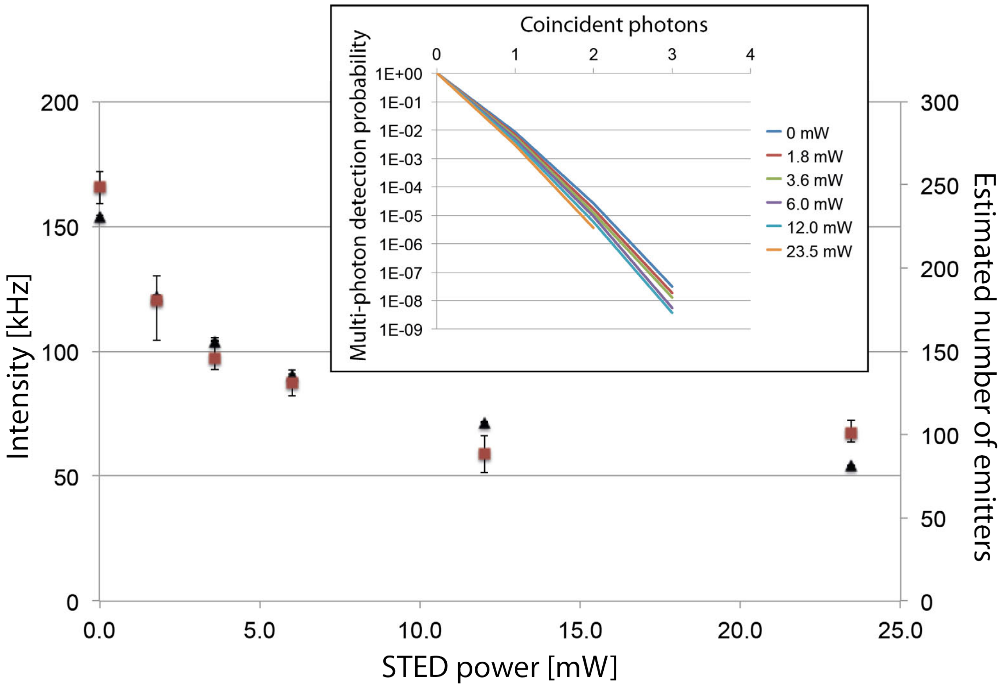

Figure 4.5.: Solution STED-CCA: Fluorescence intensity (black triangles) and estimated number of molecules by CCA (red squares) of a 10 nM ATTO647N solution STED nanoscopy plotted against varying STED powers (values indicated in the back focal plane). Time intervals of 29.3 seconds were used number estimation and intensity. Inset: Multi-photon probability distribution for varying STED intensities. Signal and estimation follow a similar trend up to $I_{STED} = 12$ mW and as expected by equation 2.3 but deviate at 23.5 mW. Possible explanations are low signal, increased excitation by the STED laser or non-confocal detection (leading to substantial out-of-focus signal), which can all lead to variations in the multi-photon distribution. Detection was adapted for best signal rather than confocalisation.

4.3.3 Scanning STED-CCA

Finally position-resolved STED-CCA traces of DNA origami were recorded by accumulating photon statistics over hundreds of scanning cycles at a pixel size of 25 nm (STED-CCA) and 50 nm (CCA), and a pixel dwell time of 1000 µs. The advantage over a single slow scan is the reduced bleaching in each scanning cycle. At very slow scanning speeds, a molecule could for instance bleach before the laser beam is centred at this positions. Fast scanning can potentially reduce such effects and even decrease overall

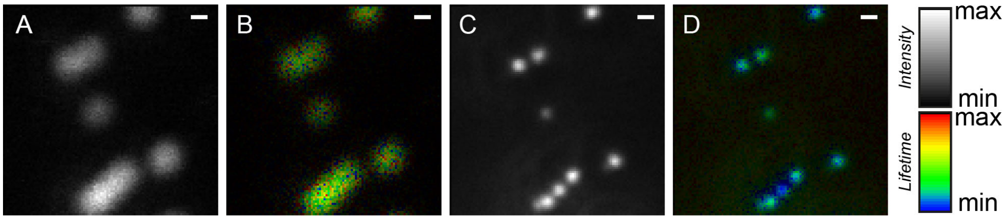

Figure 4.6.: Scanning CCA of DNA origami using the setup described in figure 4.1 for both confocal (A,B) and STED recordings (C,D). Because the arrival time of each photon is recorded with respect to excitation pulse, line clock and frame clock, it allows both counting of coincident photon events and image reconstruction. Both the intensity distribution (A,C) and lifetime (B,D) are shown demonstrating that indeed spatial and time information can be determined. Confocal recording show a single overview scan whereas STED recordings are accumulated over $\gg$ 50 scans until most signal was photobleached. Similar to PnD recordings, photon statistics can only be accumulated over time intervals where no bleaching is observed. Lifetime (min–max): $0 - 7.54$ ns (B) and $0 - 6.55$ ns (D). Intensity (min–max): $0 - 390$ counts (A), $8 - 2396$ counts (C). Scale bars: 200 nm

bleaching by allowing the relaxation from long-lived dark states [19]. Because the recorded signal is now both space- and time-resolved, it can be binned in both space- and time-domains in order to increase the accumulated photon statistics at the expense of losing of space- or time-resolution respectively. Figure 4.6 shows a confocal and STED image of DNA origami recorded with scanning CCA. The colour scale thereby represents the lifetime information obtained from the HydraHarp TCSPC module of the accumulated signal. It should demonstrate that scanning STED-CCA is feasible because both the photon time information (life-time) and location-information (2D image) can be extracted from all 4 detection channels. Analysis of this data was not possible within the time-frame of this work, but is intended in upcoming work.

5

Discussion and Outlook

Parallelised multifocal STED microscopy requires two main tasks: the generation of multiple co-aligned beam pairs (excitation/STED) and the separation of the fluorescence originating from each generated separable fluorescent volume. The wavefronts need to be controlled such that the generated focal intensity fields are diffraction-limited spots for the excitation and doughnut-shaped with central zeros for the STED wavelengths. STED/RESOLFT nanoscopy further requires stable spatial and temporal alignment between the wavelengths in each of the beam-pairs and the control of the beamlets' individual laser intensities. The stability of such a parallelised microscope mainly depends on the compactness and number of optical components. These requirements and the limited laser power in mind were the main guidelines for the design of this first parallelised STED setup. Furthermore since the recent appearance of the inherently aligned easySTED, the single-fibre design (for all involved illumination wavelengths) is considered an aim for all future developments in the field. This section will recapitulate and discuss the limitations of the different tasks mentioned above, before giving an outlook about future developments and fundamental limits of parallelisation in RESOLFT.

5.1 Beam splitting and shaping

In wide-field microscopy parallelised imaging is inherently given by using an extended illumination source and a CCD camera. In confocal disk scanners or other multifocal microscopes, microlenses are used to produce multiple spots. These are then scanned with respect to the sample and detected in parallel by the camera. The implementation of these techniques is more challenging in STED, which requires multiple wavelengths, beam-shaping and high quality beam profiles.

Rigorously speaking, in order to displace a beam in the focal plane one needs to tilt the plane wave in the Fourier plane, which corresponds to a linear phase change across the pupil. The superposition required for creating two spots, which are separated in the focal plane and generated by a single laser, is equivalent to placing a $(1 + \cos x)/2$ transmission mask in the Fourier plane (backfocal or conjugated backfocal plane) of an imaging system. The distance of the two foci is determined by the frequency of the modulation. This can by achieved by designing such a mask or using a spatial light modulator. It would inevitably include 50% transmission or reflection losses in the best case and depending on the type of device. A different approach involves splitting the beam using either polarising or non-polarising optical beam-splitters. In the most general case a cascade of beam-splitters could generate a series of beamlets. Polarisation, power, alignment and beam-shaping can then be individually adjusted in each beam and all beams be recombined, *e.g.* using sharp-edged mirrors or polarising beam-splitters. The flexibility of such an approach would come at the price of dozens of optical components to create two or more parallelised beams.

A simpler scheme uses birefringent Wollaston-type prisms, such as used in this work. The beam-splitting is directly determined by the prisms' geometry and the intensities of the individual beams can be evenly distributed by rotating the incident polarisation. Unfortunately such created beamlets exhibit mutually orthogonal polarisations and vortex phase plates are no longer usable. This vortex phase mask or helical phase ramp (from 0 to 2π) was the preferred phase mask in the past decade for creating doughnut-shaped STED beams. They require a circular polarisation that matches the helicity of the phase ramp. Combining Wollaston-type beam-splitters with vortex phase plates was thus not possible without throwing away 50% of the available (and limited) laser power[1]. Additionally a second such arrangement would be required for the corresponding excitation wavelength and the corresponding excitation/STED beam-pairs would require co-alignment[2].

Fortunately in 2010, two approaches have been reported to simplify STED nanoscopy by making excitation and STED beams pass through a common beam-shaping device: the *Aligned by design* and *easySTED* concepts [68, 91]. Both configurations leave the wavefront of the excitation wavelength largely unaltered and cause the STED beam to create the desired doughnut shape. Only the easySTED beam-shaping device proposed by Reuss *et al.*, consisting of a chromatic segmented wave plate (SWP) that alters the polarisation of individual beam segments in the aperture, was polarisation-independent with respect to keeping the central intensity null of the doughnut as low as possible. Non-circular components only led

---

[1] After the beam-splitting the beamlets would require to be linearly polarised in the same orientation by a common polarising element.

[2] This co-alignment usually necessary on a daily basis.

to asymmetry effects induced by the random orientation of the molecules. Such effects can be avoided by providing a uniform distribution of polarisation directions, *e.g.* circular polarisation. The handedness of the circular polarisation is here of no importance, which make SWPs compatible with the above-mentioned birefringent Wollaston prisms. In addition, perfect circularity is not necessary because non-circular field components do not fill up the central intensity minimum in contrast to the helical phase ramp.

The polarisation-independence of the beam-shaping device is crucial for implementing a single fibre as a common source for STED and excitation light using Wollaston prisms, because a stack of N Wollaston prisms generates 2^N beams where 2^{N-1} beams have left-handed and the other 2^{N-1} beams right-handed circular polarisation after passing a quarter wave plate. In order to produce the desired auto-aligned spots of light, the SWP is simply placed centrally close to a plane that is optically conjugated to the back focal plane. It can be placed right after the objective lens, because fluorescence can pass without major alterations, which in turn makes the preceding pupil plane accessible for the beam-splitting elements. A single fibre source including excitation and STED wavelengths could now be used to generate inherently aligned multispots, each of which consists of a doughnut-shaped STED beam and a point-like excitation. Powers can be tuned by rotation of the incident polarisation and individual prisms, and the temporal alignment of all pulses can be adjusted before the fibre coupling. More versatile optical devices such as spatial light modulators (SLM) exist, but so far these do not allow for simultaneous and individual control of the different wavelengths originating from a common source.

In chapter 3 of this work is demonstrated the first $m = 4$ parallelisation of STED using a stack of two Wollaston prisms in combination with an easySTED segmented waveplate designed for a wavelength of $\lambda = 750$ nm. Similar resolution increment could be obtained for both left- and right-handed circular polarised STED beams than in a single-spot STED setup, using fourfold total laser intensities[1]. This experimentally demonstrates that the zero intensity of the doughnut produced by the SWP proposed by REUSS is indeed polarisation independent. The chromatic birefringence of the segmented waveplate further ensures that the excitation wavelength exhibits a 3λ retardation between ordinary and extraordinary polarisation, and is essentially not disturbed by the prism. While this positive feature of chromatic birefringence is appreciated for beam-shaping, the birefringence dispersion of quartz Wollaston prisms induces an undesired difference in splitting angle as shown in figure 3.12. For small angles and small differences in splitting angle, this property can be neglected as in

---

[1] Fourfold parallelisation ideally requires fourfold total (excitation and STED) laser intensities in a loss-free setup.

the case of combining 633 nm excitation with 745 nm STED and a separation of $\sim$ 5.8 µm. For larger splitting angles and wavelength differences, the dispersion in Wollaston prisms would, however, be prohibiting parallelised easySTED. Similarly to the achromatisation of lenses, achromatisation of polarising beam-splitting prisms is feasible by a combination of materials (appendix B.1). When using a single-fibre approach for parallelisation, potential dispersion effects of all elements should therefore be considered when designing an optical arrangement. The optical setup presented in this work exhibited a lateral chromatic aberration restricting the FOV to 22×22 µm^2 when combing 510 nm excitation with 745 nm STED as demonstrated in figure 3.13. The objective, tube and scan lenses should be corrected for the entire spectrum of wavelengths and emission wavelengths used in the system to reduce such lateral (and axial) chromatic aberrations[1].

Using the spectrally recursive SWP feature of doughnut and point-like illumination as calculated and measured in figure 3.10, the extension of easySTED to multicolour imaging was demonstrated using excitation multiplexing and mega-Stokes shifts dyes. It was shown that a resolution increment can be obtained by exciting Dyomics521XL with 510 nm, exciting Atto647N (and related dyes) with 633 nm, and depleting the peripheral molecules using the same 745 nm STED laser. An increment in resolution was observed for both spectrally separable dyes, although Atto647N-type dyes proved to be better adapted to this setup. Currently mega-Stokes shift dyes still have inferior brightness and resistance to bleaching compared to conventional dyes. Relatively long excitation pulses ($150 - 600$ ps for 510 nm) and relatively short STED pulses ($\sim$ 77 ps) could also have decreased the contrast for Dyomics521XL. Due to the various restrictions for multicolour imaging, *e.g.* single-band bandpass filter used in reflection and the SWP designed for a wavelength of 750 nm, more suitable dyes for multicolour STED could not be used in the present scheme.

5.2 Detection and Scanning schemes

Excitation and detection geometries are generally both influencing image contrast, resolution and sectioning capabilities in microscopy and nanoscopy. Confocal microscopy, where excitation and detection PSFs are focused down to the same diffraction-limited volume, is hereby the prominent example. In multifocal microscopy setups, such as the present parallelised STED scheme, an array of excitation foci (overlaid with doughnut-

---

[1] The tube/objective lenses, used in this work, lead to a 0.43% lateral chromatic aberration and a $\sim$175 nm offset in axial direction for the 510/745 nm beam combination. They were therefore insufficiently corrected for in the NIR spectral range for recording larger FOV than 22×22 µm^2

shaped STED beams) leads to independent fluorescent sources at well-defined positions in the focal plane. The fluorescence is usually recollected by the same objective lens used for illumination (in a single-objective lens system) and needs to be decoupled from the illumination beam path, preferably undistorted. Depending on whether a descanned or non-descanned approach is selected, the fluorescence either returns across the scanner or is previously decoupled from the illumination beam path. Either way targeted super-resolution techniques require that the signal from each fluorescent volume is individually registered at each scanning step[1]. For this purpose the separation of the signal requires a so-called optical cross-section converter, whose function is to isolate the individual channel signals from the collective signal and which is commonly placed in a conjugated image plane[2]. The most simple cross-section converter is a grid detector, *e.g.* CCD camera, in which every single pixel detects the signal from a different volume in the sample, as given by equation 2.2. For using point detectors (that enable the fast recording times required for STED), the optical cross-section converter needs to both isolate the beams and guide them towards the point detectors. A fibre bundle shown in appendix B.6 could fulfil these tasks simultaneously for a specific geometry of excitation/detection volumes. The size of the fibre cores would thereby act as pinholes. A more flexible solution was presented in this work, consisting of a silver-coated pyramid and placed in the conjugated image plane (Fig. B.2). In combination with the point-detector area (which acted as pinhole) this solution provided a tuneable cross-section converter for $m = 4$ parallelisation. Eventually, (currently commercially unavailable) fast and single-photon sensitive grid detectors will be the optimal solution for further parallelising RESOLFT.

Scanning schemes

Different imaging approaches can now be taken regarding scanning and recombination of detection channels. Regardless of the approach, parallelisation aims at increasing the overall acquisition rate as illustrated in figure 3.1. The most straightforward approach is to scan non-overlapping areas and to recombine the individual frames by stitching them together in a mosaic-like pattern (stitching scheme, Fig. 3.8). For FOVs larger than

---

[1] Non-descanning combined with signal integration over an entire scanning cycle, such as used in multifocal multiphoton microscopy or confocal spinning disc microscopy [9] [42] are incompatible with STED/RESOLFT-type nanoscopy. The high spatial frequencies would, in this case, be smearing out due to diffraction-limited detection. The signal could, however, be read out at each scanning position in a non-descanned setup. This would increase the complexity of post-processing without delivering any significant advantage.

[2] A temporal distinction is also possible as demonstrated by Andresen et al. [3].

the inter-focal distances, one needs an array of scanning positions in order to avoid multiple scanning of the same positions (Fig. B.7). Another approach consists of scanning larger areas (than the inter-focal distances) and adding the overlapping regions of the full-scale frames (overlay scheme, Fig 3.9). Besides reducing the recording time, the advantage of such an approach could be a bleaching-reducing effect by reducing the deposited energy dose imposed by each of the individual beams and allowing the relaxation of the molecules from long-lived dark states back into the ground state [19]. Smaller FOVs here lead to decreased overlapping, which in turn gradually reduces the parallelised area (Fig. 1.1)[1].

A common property of all optical nanoscopy methods is the need for time-sequential recordings. During an image recording cycle the sample or optical setup can be subjected to drift of the sample or other fluctuations present in the setup. Stochastic super-resolution techniques for this purpose often include bright non-bleaching probes, *e.g.* quantum dots, that act as references during post-processing. Single-spot targeted techniques are generally less prone to drift for recording a single image provided that drift evolves on longer timescales than scanning[2]. The timescales on which stability needs to be provided in parallelised nanoscopy additionally depend on inter-focal distances: (i) in the overlay scheme the time required for all multispots to raster-scan the same position in the focal plane or (ii) in the stitching scheme the time required for scanning bordering but non-overlapping regions. For large scale (nonlinear) structured-illumination microscopy (NL-SIM) stability needs to be guaranteed during the entire acquisition procedure because the entire recording sequence (all scanning orientations) is evaluated to obtain 2D resolution [28]. Drift can therefore lead to processing artefacts, *e.g.* negative copies, and represent an additional source for misinterpretation. In contrast to NL-SIM, each channel in multifocal microscopy (MM) already offers 2D resolution and post-processing only requires calibrated offsets (even if drift is present).

The offsets can be directly determined from the cross-correlation between individual recorded channels as described in appendix B.3. This procedure requires large overlapping (scanned) areas and can therefore only be adaptively implemented in the overlay scheme. A good result relies on intensive and identical signal in each of the channel. Low signal, bleaching, drifts and differences in resolution therefore deteriorate the accuracy and quality of the offsets and eventually the merged images. The stitching scheme on the other hand relies on fixed offsets previously determined using cross-correlation or by manually stitching the channels. The

---

[1] Still another option would be a comb-like scanning pattern with a line of spots, easily produced with a different prism arrangement.

[2] In two- or three-dimensional recordings drift should always be slower than the slowest axis.

contrast of the final image is, in this case, not compromised by the merging of the individual channels and the (recombination) errors are only restricted to the (overlapping) bordering regions. These regions are then subject to increased illumination and thus potential bleaching or exhibit gaps as shown in appendix B.5. In the SIM scheme the full recording sequence can induce artefacts spread across the entire FOV. Recapitulating, all scanning schemes require calibration and post-processing to recombine all channels to a single two-dimensional image (or three-dimensional image stack). When looking at how errors and artefacts are spread over the final image after post-processing, the differences between the scanning schemes become noticeable.

Mathematical treatment is inevitable in parallelised nanoscopy. While the inherently parallelised stochastic switching and readout methods require mathematical processing for both breaking the diffraction limit and generating the image, targeted switching methods such as STED require no post-processing for regular single spot laser scanning microscopy. Parallelised easySTED nanoscopy in this matter requires relatively simple post-processing for combining the parallelised signals into a single image. For large distances between parallelised volumes, the main problems are of technical nature such as stability and drift. One-dimensional NL-SIM, on the other hand, represents a faster (and therefore more stable) scanning scheme, but relies on deconvolution algorithms more vulnerable to artefacts[1]. The simple operations mentioned above are, however, sufficient for the distances of the $m = 4$ parallelised multispot setup used in this work. Other problem that arise for MM at shorter distances are discussed in section 5.3.

Coincidence analysis

An entirely different detection method was presented in the second part of this thesis. Coincidence analysis (CCA) applied to targeted super-resolution microscopy enables direct counting of the number of emitters inside a sub-diffractional volume. Being essentially an ensemble technique, targeted nanoscopy is often criticised for not being able to procure quantitative results. In RESOLFT nanoscopy, molecular brightness can be influenced by laser powers, the local environment of the dyes and the modulation of the switching beam, *i.e.* doughnut beam zero. Hence, the signal intensity is by itself not a reliable quantity for estimating the number of emitters. Stochastic nanoscopy using PALM on the other hand often

---

[1] The striped pattern only needs to be shifted by $\lambda/2$ in each scanning direction for scanning the entire FOV. Denser multispot arrangements increased cross-talks between detection channels.

claims that, being a single-molecule technique, it can provide quantitative information [4]. However, in order to reliably determine the number of emitters in the sample, exact knowledge about the photophysical behaviour and photochemical microenvironment of the dyes is required as well as confidence that the majority of molecules has been localised (only once)[1].

CCA offers a quantitative solution for STED/RESOLFT nanoscopy, solely based on the quantum mechanical phenomenon of photon antibunching and the statistical analysis of coincident photons. By splitting the fluorescence onto four detectors using three neutral 50/50 beam-splitters as described in figure 4.1, up to four coincident events can be recorded per switching cycle[2]. By statistically evaluating the multi-photon distribution and fitting the model distribution given by equation 2.8, the number of emitters and normalised molecular brightness can be estimated. (A more detailed explanation is given in section 2.5.1).

In preliminary measurements, fluorescence time traces were recorded inside an effective sub-diffractional volume of 140 nm lateral extension and up to 9 molecules were estimated by STED-CCA of DNA origami conjugated with 36 ATTO647N labels at a time resolution of 1 second (Fig. 4.4). Higher number of emitters could not yet be determined. Strong bleaching of the sample and a low normalised molecular brightness p (compared to previous results [83]), currently prevented higher estimations with STED. As an alternative to CCA, bleach step analysis can count low number of surface-bound emitters and can act as control for evaluating the method. By scanning the beam across a sample, space-resolved STED-CCA offers a possibility of resolving both the structure with sub-diffractional resolution as well as count the absolute number of emitting (fluorescent) molecules at each position (Section 4.3.3). The number of molecules (inside the effective fluorescent volume) can be actively controlled by varying the switching (STED) intensity and therefore theoretically extend CCA to higher densities than previously possible for diffraction-limited CCA (Section 4.3.2).

The main challenge of the method remains the acquisition of good photon statistics, *i.e.* many (coincident) photons, and is mainly hindered by

---

[1] This includes dipole orientation, the presence of dark states from which the molecule can spontaneously recover (i.e. blinking) and varying brightnesses, spectra and fluorescence lifetimes induced by the photochemical micro-environment.

[2] A $\sim$ 30 ns dead time after each detection event (of the commonly used avalanche photodiodes) is still limiting the detection to one event per laser cycle and detector, because the dead time exceeds the fluorescent lifetime of most common fluorophores. Extending the splitting to even more detectors is possible but may not result in a significant improvement over a four detector design because additional beam-splitters also further reduce the signal as given by equation 2.8.

(still) poor collection efficiency and brightness, photobleaching and blinking (*e.g.* due to transient dark states). In the future bright and non-bleaching (fluorescent) probes, such as RESOLFT-compatible and single-photon emitting quantum dots, might provide the mandatory properties. The recent development of fast hybrid photodetectors (HPDs) further have the potential to detect coincident photons with a single detector and would thereby make a *Hanbury-Brown–Twiss* setup design obsolete [81]. Very recently SCHWARTZ *et al.* even derived the concept of *Fluorescence antibunching microscopy*, which could theoretically provide a resolution enhancement by evaluating the space-resolved PAB signal[1] [73]. This is closely related to the concept of increasing resolution using mutliphoton detection, proposed by STEFAN HELL in 1995 [36].

5.3 Inherent limits of multifocal microscopy for RESOLFT

An important condition for obtaining parallelised STED nanoscopy without compromising its features (such as axial or lateral resolution, detection efficiency, S/N) is to avoid spatial overlap between the parallelised excitation or detection PSFs, both in- and out-of-focus. Overlap directly leads to cross-talk between the signals detected in the individual detection volumes/channels.

In regular multifocal microscopy (MM), *e.g.* Nipkow Spinning disc microscopes, individual illumination and detection PSFs usually coincide by using the same pinhole for illumination and detection [42]. Recalling section 2.2 each MM-pinhole generates an illumination pattern h_{exc} and each excited molecule is detected with a similar probability given by the effective detection PSF $h_{det}(r) \otimes \rho(r)$. ($h_{exc}$ and h_{det} have dimensions given by equation 2.1.) Placing the pinholes closer together increases the probability of one detection PSF overlapping with an adjacent illumination PSF and thus enhance cross-talk. Furthermore, the commonly used coherent laser light in fluorescence microscopy can interfere both in- and out-of-focus and thus create regions of increased excitation and detection. Especially the out-of-focus interference increases dramatically with the degree of parallelisation because more and more illumination cones overlap. Finally the size of the pinholes is important for obtaining a good sectioning depth and reduce cross-talks. The exact geometry of illumination and detection therefore plays a crucial role in MM in order to avoid cross-talk and excessive photobleaching while conserving resolution, sectioning depth and detection efficiency. Nevertheless, this is a common problem

---

[1] Whereas the intensity of two very close emitters is highest at the centre, the photon antibunching dip depth is the most shallow at this position.

to all parallelised 3D microscopy techniques and has already been studied extensively [21, 60].

STED-MM now introduces an additional illumination field critically relying on a perfect zero intensity at the centre of each of its multispots. Placing the parallelised beams closer together will inevitably increase interference among them and hence influence the field at this null position. One should, however, carefully distinguish between coherent and incoherent interference. While incoherent superposition leads to simple addition of intensity distributions, coherent interference has to consider amplitude, phase and polarisation before adding the electric field components of the beamlets. Consequently coherent multispot generation for STED illumination can have an entirely different response than incoherent superposition. Lastly, the resultant effective fluorescence response of the system is dependent on excitation and detection PSFs, OFF-switching pattern and dipole orientation of the fluorescent molecules (which can have a fixed orientation) [22]. Because both excitation and depletion fields have such different shapes and tasks, one cannot *a priori* tell what the optimal distance between beamlets is in order to obtain the most compact excitation and depletion pattern for MM-STED. Out-of-focus interference of multiple STED beams could for example provide additional axial depletion fields as calculated in appendix B.4 (for a doughnut separation of 1500 nm and $\lambda_{STED} = 750$ nm). For all these reasons thorough calculations of excitation, STED and the resulting effective STED point-spread functions are necessary to determine the limits of parallised STED nanoscopy.

In this work the multispots were placed at a distance of ~ 5.8 µm for allowing their separation in the detection. In order to check whether neighbouring doughnuts can degrade each others central null by interference, the central zero intensity dependence on the nearest neighbour distance is calculated for two coherent field (both right-circular (rc) or right- and left circular (lc)) and for incoherent superposition in figure 5.1. Regardless of coherence or circularity the presence of a neighbouring STED ($\lambda_{STED} = 750$ nm) beam fills the null by less than 0.1% of the maximal focal intensity for distances > 1.25 µm. Differentiation between different superposition modes becomes more pronounced at smaller separations. Coherent (rc+rc) interference here provides a much lower minimum intensity than the incoherent case for specific separations. For coherent superposition it is expected that the vicinity of another STED beam would only shift the zero intensity laterally instead of filling it. When investigating on what vector components fill the zero (at a separation of 750 nm for $\lambda_{STED} = 750$ nm) in figure 5.2, one finds that the z–field component is the main contributor to the unwanted intensity in the central null, similar to the helical

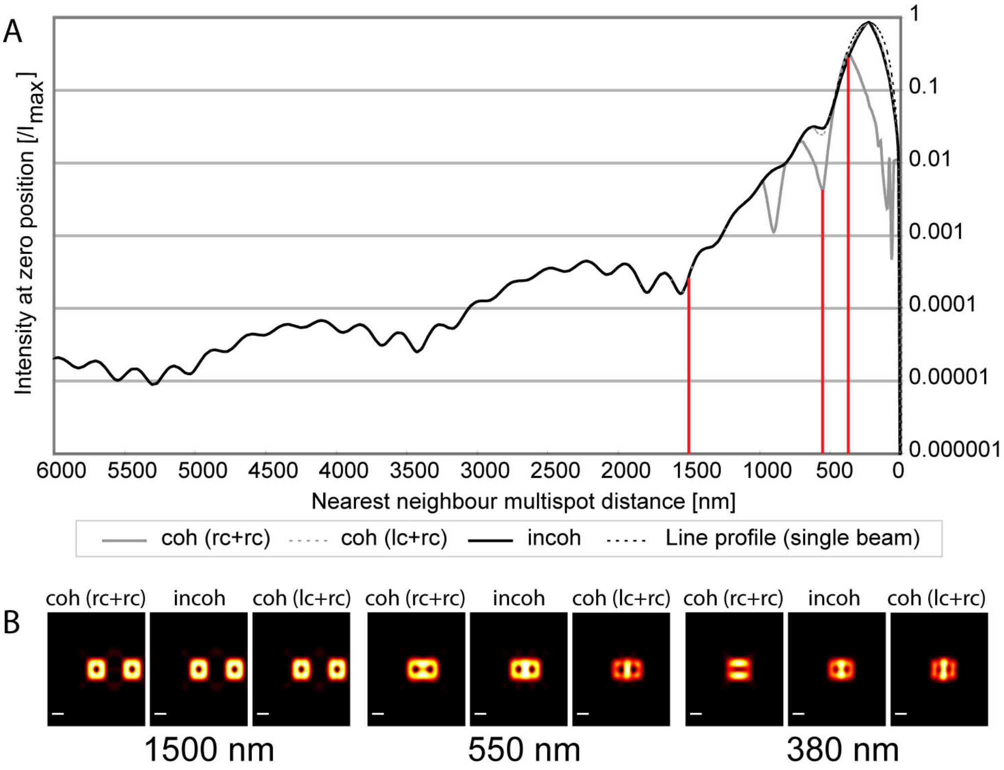

Figure 5.1.: (A) Central zero doughnut intensity in the focal plane, using SWP as beam shaping device, with respect to the nearest neighbour distance of a second doughnut. The central intensity is calculated for coherent superposition of identical circular polarisations (grey), counter-rotating (grey striped) circular polarisations or incoherent superposition (black) by selecting the lowest value within a $330 \times 330\ \mathrm{nm}^2$ area around the initial null position of a single doughnut for accounting for expected shifting of the zero position. For comparison the intensity profile of a single doughnut (black striped) is shown. The calculated values for interference of neighbouring doughnuts show that above 1.2 μm (scaling with wavelength λ) for $\lambda = 750$ nm , the filling of the central zero intensity due to a second doughnut remains below 0.1%, which is commonly an acceptable value. Even down to a separation of $\sim$ 1 μm the three possible scenarios do not result in different filling of the central zero. (B) At short separations one needs to consider how interference influences the shape of neighbouring doughnuts. The calculated focal intensities for the three interference scenarios mentioned in (A) are shown for separations 1500 nm, 550 nm and 380 nm also indicated by red lines in (A). Strong variations of the different modes of interference can be observed for coherent superposition of two right-circular polarisation (coh(rc+rc)), right and left-circular polarisation (coh(lc+rc)) and incoherent addition (incoh). Intermediate scenarios, *e.g.* partially-coherent, are also possible. Scale bars: 500 nm.

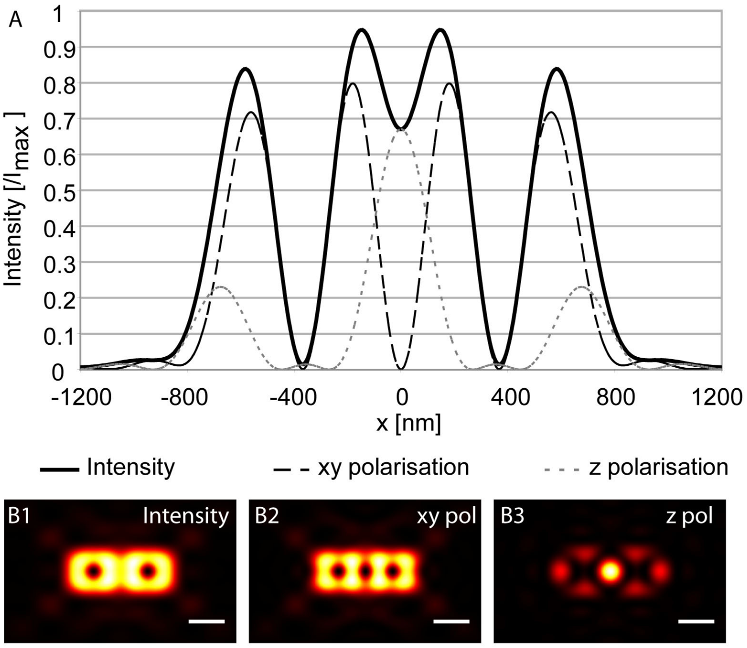

Figure 5.2.: (A) Horizontal line profiles across images B1-3 showing the total (black, B1), lateral (black striped, B2) and axial (grey dotted, B3) polarisation components of the intensity distribution of two identically circular polarised STED beams laterally displaced by 750 nm. One can clearly observe in (A) that the zero intensities of the doughnuts are filled up partially by the z-polarisation component of the intensity. Scale bars: 500 nm.

phase ramp mask when using the wrong circular polarisation.

The goal for parallelisation in RESOLFT should ultimately be to generate the densest and largest array of zero intensity positions that can be distinguished in the far-field detection. The most compact parallelisation of two- and three-dimensional STED pattern has been calculated in the work of Jan Keller for generating beams using spatial light modulators (SLMs) [46]. Although SLMs combine the tasks of beam-shaping and beam-splitting, they currently cannot simultaneously and individually do this for both excitation and STED pattern. Each wavelength would still require its own optical path, which would reduce the stability of such a system. The high laser powers required for STED, high losses induced by the SLMs and their elaborate calibration made this approach currently unfeasible. Switching schemes that require less laser power (such as fluorescent switchable proteins) may make the illumination pattern proposed by Jan Keller or structured-illumination approaches possible for large-scale parallelisation [96]. RESOLFT by structured-illumination has recently been achieved with the reversibly-switchable fluorescent proteins asFP595 and Dronpa, but was still limited by their limited number of switching cycles [66, 75]. As stated earlier, (nonlinear)-SIM further relies on deconvolution algorithms that are more vulnerable to artificially produced artefacts. This leads to the general uncertainty about whether the generated image represents the actual distribution of the recorded structure.

Future multispot easySTED can be optimised for multicolour STED measurements by carefully screening available laser wavelengths, dyes suitable for STED and designing improved beam shaping devices. The SWP proposed by Reuss *et al.* was only the first generation of such beam shaping devices providing the crucial properties for parallelised easySTED nanoscopy. Future easySTED (and generalised easyRESOLFT) devices could include three-dimensional resolution improvement, as already demonstrated by Matthias Reuss [67], and provide broader (or tunable) wavelength regions for generating the desired switching/excitation illumination pattern, while guaranteeing quasi-undisturbed transmission for the respective fluorescence. One should therefore also investigate the variety of optical material and designs (segmentation, stacking) for producing the desired devices. Development of new dyes for STED/RESOLFT and developments in the laser industry will further widen the possibilities for parallelised multicolour easySTED/easyRESOLFT. For large scale parallelisation, a structured-illumination approach in combination with low-power RESOLFT may eventually provide a simpler solution for parallelisation than the easySTED concept. The low powers required in RESOLFT with slow-switchable dyes offer the possibility of using slow but large area single-photon sensitive detectors (*e.g.* EMCCD). Furthermore structured switching illumination can be combined with wide-field excitation, which makes alignment similarly obsolete as in this work. Other advantages of both the (multi-focal) easy-concept and STED will remain, such as the superior axial resolution of multispot microscopy (compared to wide-field illumination/detection), more effective lateral resolution enhancement of circular polarised doughnut beams (compared to one-dimensional depletion pattern)[1], and the faster switching and recording of STED (compared to RESOLFT with slow-switchable dyes). It is therefore believed that easySTED and future easyRESOLFT will become and remain prominent schemes in (parallelised) targeted optical nanoscopy.

---

[1] Depletion with a doughnut-shaped beam is more effective because structured-illumination illumination requires polarised depletion, which in turn only affects a subset of molecules with preferred dipole moment (,which are not entirely freely rotating) [22].

A

Sample preparation

Technical samples

Technical samples were prepared by first cleaning the cover slips with ethanol (70%) and air-dried, followed by immersion in poly-L-lysine (Sigma Aldrich, USA) for 10 minutes, following careful rinsing with ddH$_2$O. The treatment of poly-L-lysine is thereby forming a positively charged layer. Then, either an aqueous solution of gold beads ($\approx 0.2 - 0.3$ ml^{-1}) was allowed to passively absorb to the coated cover slip for 10 minutes, again followed by rinsing with ddH$_2$O. Alternatively, fluorescent beads (FluoSpheres, Invitrogen, USA) diluted $1 : 10000 - 1 : 10000$ in ddH$_2$O were applied in the same manner. In either case, the cover slip was placed on an objective slide, embedded in Mowiol with DABCO (1, 4-diazabicyclo-[2.2.2] octane) and let dry.

Biological samples

Biological samples were mammalian PtK2 cells which were stained using an immunofluorescence protocol involving various primary antibodies (single colour staining: anti-alpha-tubulin mouse IgG (Sigma, T6074), anti-vimentin mouse IgG (Sigma V6389), dual colour staining: anti-alpha-tubulin (Abcam Plc., ab15246)) and various labelled secondary antibodies (Jackson Immuno Research, West Grove, USA). The used dyes were ATTO 647N (ATTO-TEC GmbH, Siegen, Germany), KK114 and KK9445 (Abberior GmbH, Göttingen, Germany), and Dyomics521XL (Dyomics GmbH, Jena, Germany), respectively. Samples were fixated using methanol, and embedded again in Mowiol with DABCO as an antifading agent.

B

Supplementary information

B.1 Dispersion of Quartz

The dispersion of silicon dioxide or more commonly known as quartz is given by the Sellmeier equation,

$$n_{o,e}^2 = A_{o,e} + \frac{B_{o,e}\lambda^2}{\lambda^2 - C_{o,e}} + \frac{D_{o,e}\lambda^2}{\lambda^2 - F_{o,e}}. \tag{B.1}$$

A, B, C, and D hereby represent the Sellmeier coefficients given in table B.1 [25]. The coefficients for ordinary and extraordinary polarisation of quartz were experimentally measured by Ghosh [25] and are given in table B.1. Based on these coefficients the chromatic birefringence, $b(\lambda) = n_o - n_e$, was calculated for the wavelength used in this system are $8.93657 \cdot 10^{-3}$ (745 nm), $9.04236 \cdot 10^{-3}$ (633 nm) and $9.23391 \cdot 10^{-3}$ (510 nm).

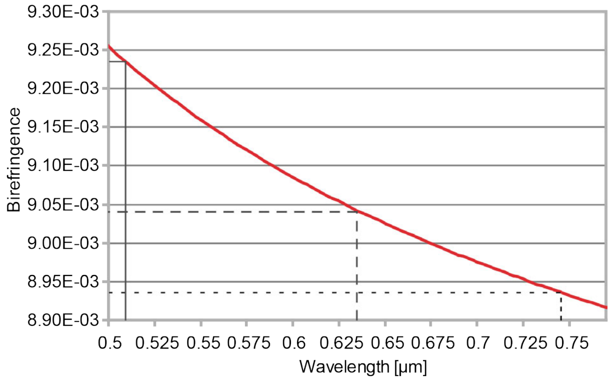

Figure B.1.: Chromatic birefringence of quartz. Wavelength indicated are 510 nm (black, continuous), 633 nm (black, striped) and 745 nm (black, dotted).

	A	B	C (10^{-2})	D	F
o	1.28604141	1.07044083	1.00585997	1.10202242	100
e	1.28851804	1.09509924	1.02101864	1.15662475	100

Table B.1.: Quartz dispersion coefficient for ordinary (*o*) and extraordinary (*e*) polarisations.

Quartz was used throughout this work for the Wollaston prisms. Alternatively an achromatic Wollaston prism can be constructed for the visible range with a combination of MgF_2 and SiO_2 as shown in figure B.2.

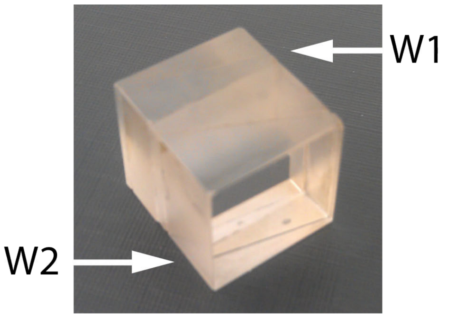

Figure B.2.: Achromatic Wollaston prism can be constructed for the visible range with a combination of two Wollaston prism (W1, W2) made out of MgF_2 and SiO_2.

B.2 Setup for m=4 parallelised easySTED – Photographs

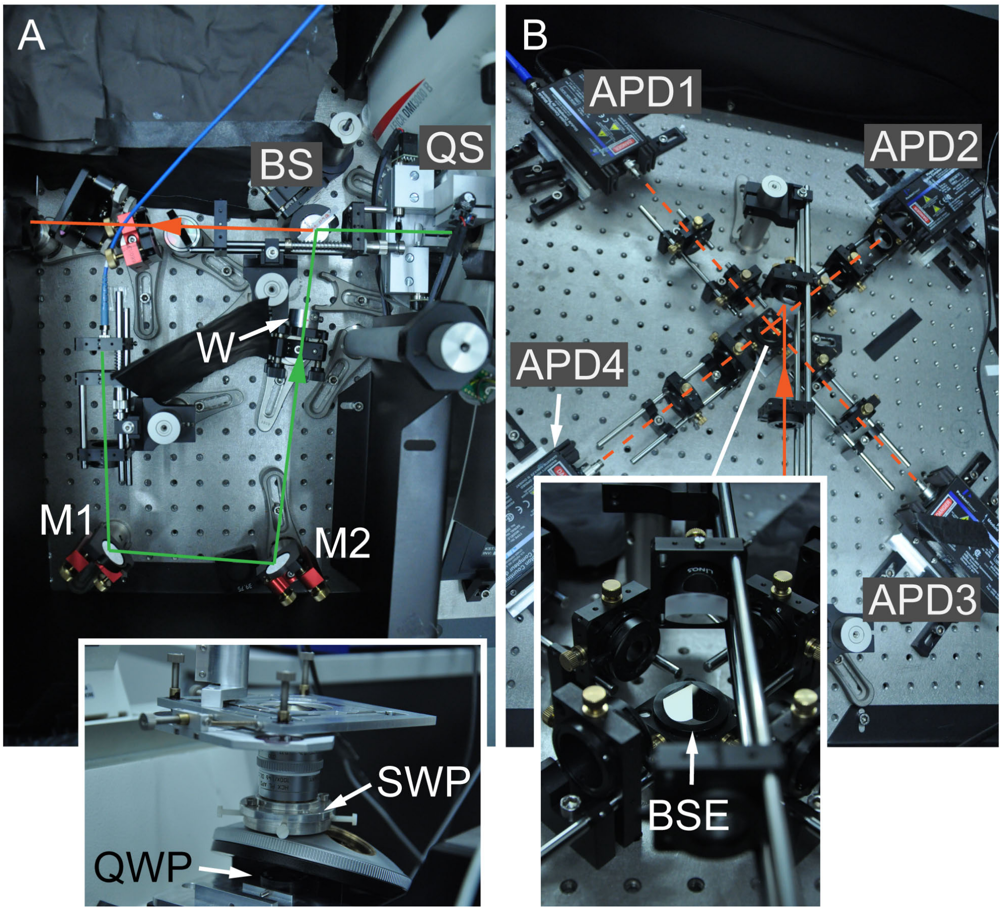

Figure B.3.: (A) Excitation and STED wavelengths (green), originating from the same fibre (blue), are collimated and transmitted over two mirrors (M1,M2) across the stack of two wollaston prisms (W) and focused into the beam scanner (QuadScanner, QS) after being reflected by the custom-made beam-splitter (BS). Inset (A): After the QS, the light is passing a tube lens (not shown), quarter wave plate (QWP), and segmented (easySTED) wave plate (SWP) before being focused into the sample by the objective lens. (B) The fluorescence (orange) is transmitted by the beam-splitter and focused onto the tip of a silver-coated pyramid acting as beam-separating element (BSE, inset: magnification). Each of the four parallelised channels is then refocused onto a separate avalanche photodiode (APD1–4).

B.3 Offset calculation by cross-correlation

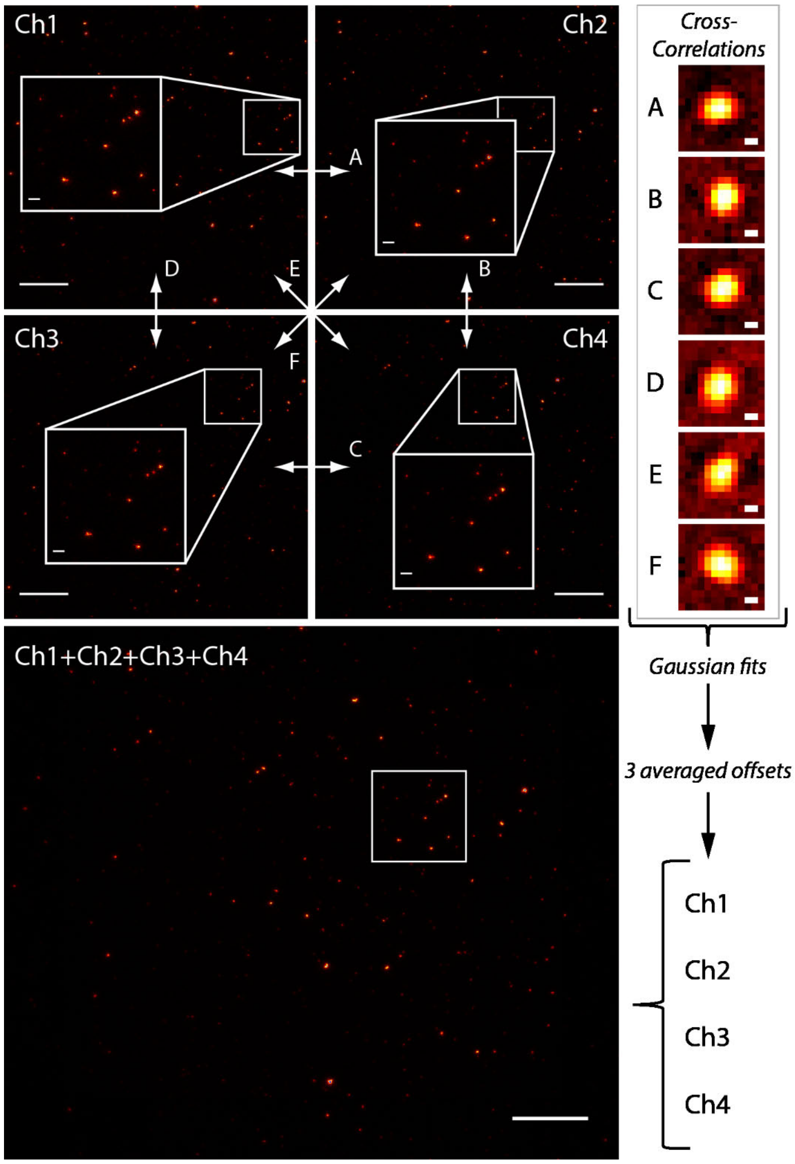

Figure B.4.: Procedure for calculating the offsets between $m = 4$ detection channels (Ch1–4) of multifocal STED microscopy and recombination (Ch1+Ch2+Ch3+Ch4) to a single image shown exemplarily for a sparse layer of Crimson beads. Zooms indicate the same sample region in Ch1–4. The six cross-correlation (A-F) combination between channels 1–4 are calculated by equation 3.2 and the zooms around their peak values shown (*Cross-Correlations*, right). Two-dimensional gaussians are fitting for determining the most accurate offset between two channels. For increasing the accuracy of the offsets, the fitted values are averaged such as to extract three offsets from the six fits: e.g. $\vec{d}^{a}_{12} = \frac{1}{3}\left(\vec{d}_{12} + (\vec{d}_{13} + \vec{d}_{32}) + (\vec{d}_{14} + \vec{d}_{41})\right)$, where $\vec{d}_{12}$ denotes a offset vector of channel 2 with respect to channel 1, and ^{a} represents the averaged offset vector. Scale bars: 5 µm (Ch1-4, $\sum \mathrm{Ch}1-4$), 40 nm (A-F).

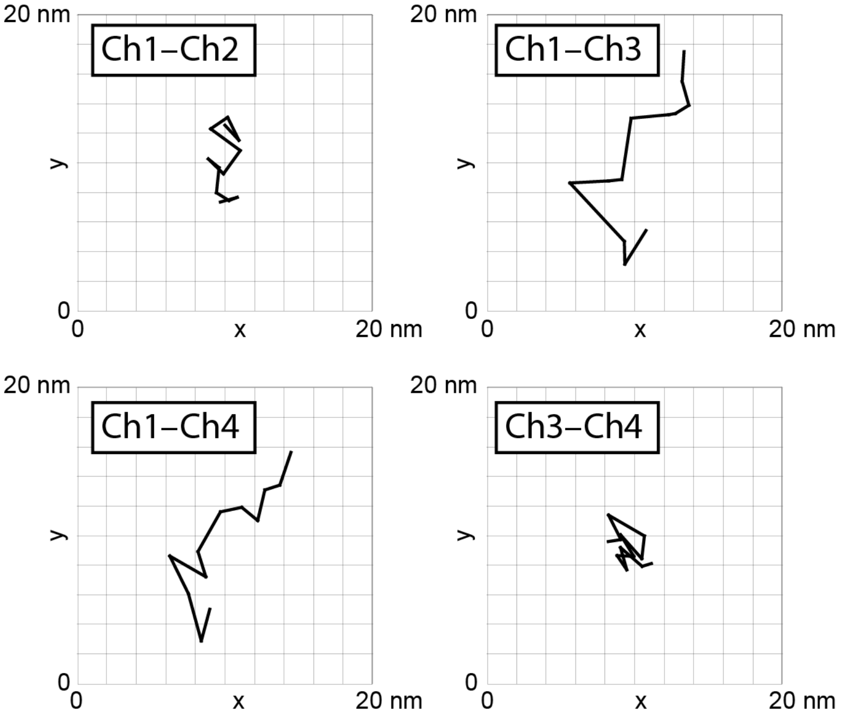

Figure B.5.: Stability of offsets between parallelised detection channels of the Crimson bead sample recorded with a pixel size of 20 nm and a pixel dwell time of 50 µsec in figure B.4. The offsets were determine by averaging of the gaussian fits of the cross-correlation (A-F) every 5 minutes for a duration of 1 h. For better comparison zooms of 20 × 20 nm around the average offsets were shown. The average value for $x - y$ of 5764 − 135 nm (Ch1-Ch2), 3821 − 4109 nm (Ch1–Ch2), 9588 − 4238 nm (Ch1–Ch3) and 5757 − 119 nm (Ch3–Ch4) need to be added for getting the actual offset values. The graph clearly show that the offsets are vulnerable to drift because channels 1–2 and 3–4 correlate more accurately than the other combination. This conclusion is drawn from the fact that the channels 1–2 and 3–4 probe the same features in the focal plane within a very short time interval while a longer interval exists between pairs 1–2 and 3–4. Nevertheless, provided that stability is guaranteed, this $m = 4$ multispot setup can provide a stability of < 5 nm.

B.4 Multispot in axial directorion

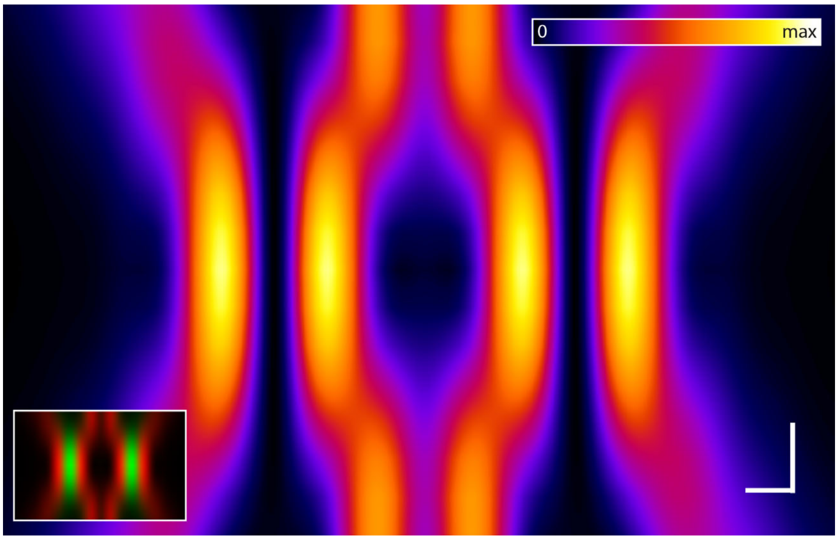

Figure B.6.: Axial (*xz*) profile of two right-circular polarised doughnuts generated by a easySTED segmented waveplate at $\lambda = 750$ nm and a separation of 1500 nm. This simulation should illustrate the possible out-of-focus constructive interference (seen above and below the focal plane at the centre of both doughnuts) arising when reducing the separation between multispots. For excitation at 635 nm only (inset, green) this separation does not lead to important out-of-focus interference. Out-of-focus interference, however, increases with degree of parallelisation, arising from purely geometrical considerations. Such calculations and simulations therefore represent an essential tool for testing new parallelisation geometries. Scale bars: 200 nm.

B.5 Stitching of large field of views

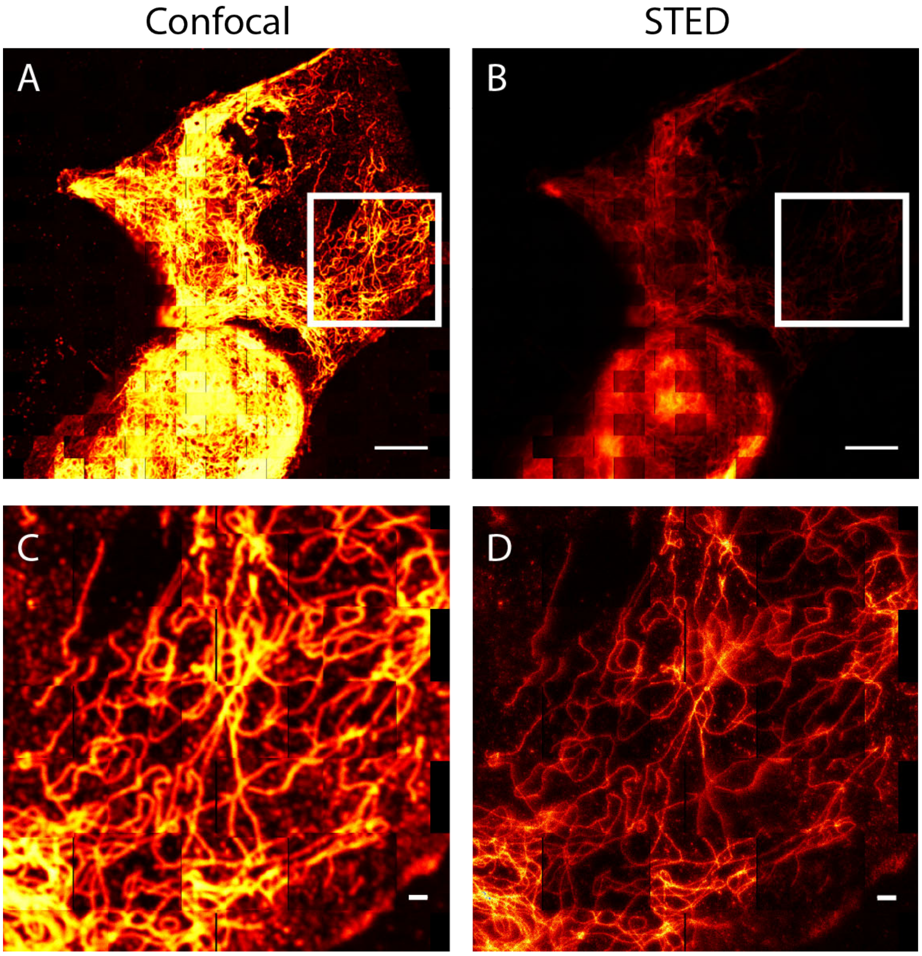

Figure B.7.: Parallelised $m = 4$ easySTED nanoscopy is extended to large field of views by addressing an array of scanning positions as shown for confocal (A, C) and STED (B, D) recordings of KK9445 labelled vimentin in PtK2 cells. Zooms at selected regions (white squares in A,B) clearly show that individual vimentin strands can be followed across multiple channels. Some bordering regions exhibit black gaps, different intensities on both sides or displacement. Besides demonstrating the potential of large scale paralellisation by stitching, this example also demonstrates the drawbacks and necessary calibration for avoiding these scanning artifacts. Scale bars: 10 µm (A, B), 1 µm (C, D).

B.6 Fibre bundles for parallelised easySTED detection

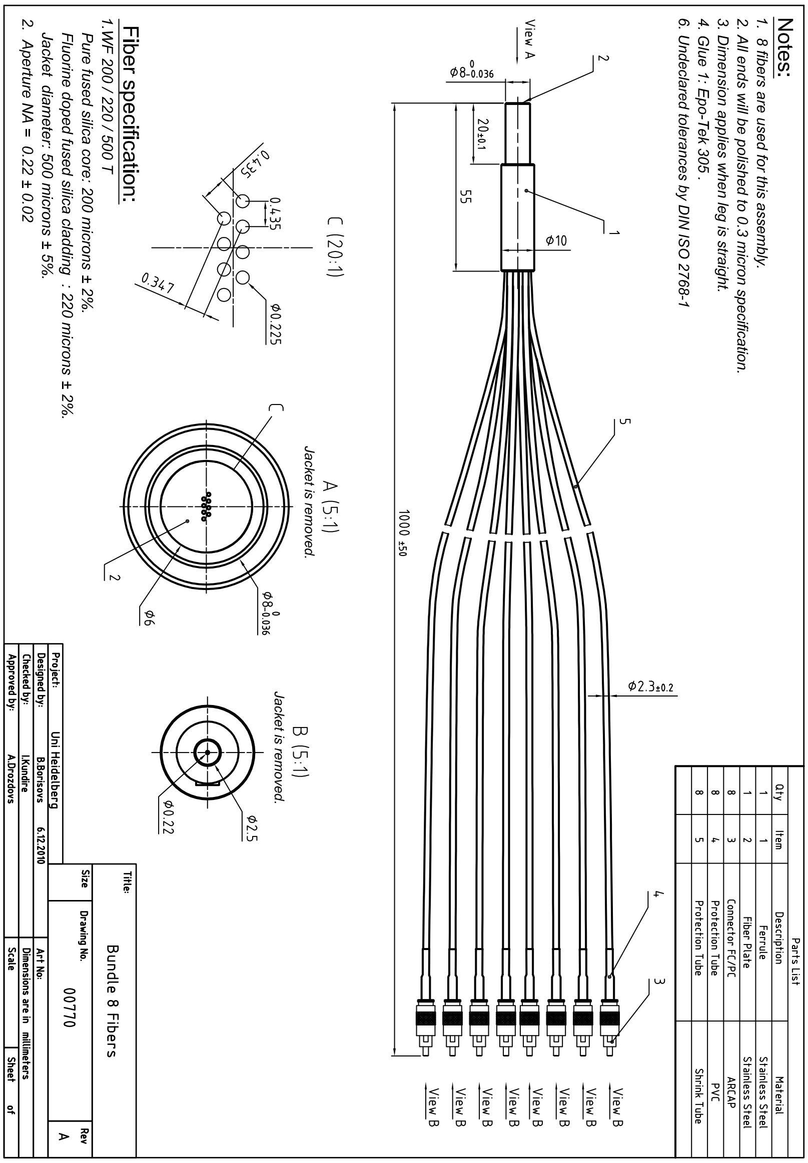

Figure B.8.: Technical drawing of a fibre bundle consisting of eight multimode fibres arranged in a rhombus like arrangement on one side (A,C) and splitting to individual fibres on the other side. The construction can act as optical cross-section converter for eightfold parallelisation of easySTED or easyRESOLFT nanoscopy by polarisation-based beam-splitting. The rhombus shape is due to the 45° by which the Wollaston prisms are rotated with respect to each other.

C

Publications and conference contributions

P. Bingen, T. M. Staudt, C. Kempf, H. Horstmann, J. Engelhardt, T. Kuner, S. W. Hell, Poster: *Calyx of Held: STED nanoscopy of a glutamatergic terminal*, European Biophysics Associations meeting, Genova, Italy, 2009

Poster prize

J. Engelhardt, P. Bingen, Gebrauchsmuster (Utility Model): *Optischen Anordnung zur hochfrequenten Pulsmodulation von Dauerstrichlasern*, Nr. 20 2009 008 281.4, German Patent Office, 2009

P. Bingen, J. Chojnacki, T. Staudt, J. Engelhardt, H.-G. Kräusslich, S. W. Hell, Poster: *Fab Fragments Versus Full IgGs in Stimulated Emission Depletion (STED) Nanoscopy*, Biophysical Society – 54th annual meeting, 2010

F. Persson, P. Bingen, T. Staudt, J. Engelhardt, J. O. Tegenfeldt, S. W. Hell, *Fluorescence Nanoscopy of Single DNA Molecules by Using Stimulated Emission Depletion (STED)*, Angewandte Chemie International Edition 50 (24), 5581-5583, 2011
Fluoreszenznanoskopie einzelner DNA-Moleküle mit Fluoreszenzverhinderung durch stimulierte Emission (STED), Angewandte Chemie 123 (24), 5696-5698, 2011

P. Bingen, F. Persson, T. Staudt, J. Engelhardt, J.O. Tegenfeldt, S.W. Hell, Lecture: *STED nanoscopy of DNA*, Focus on microscopy, Konstanz, Germany, 2011

P. Bingen, M. Reuss, J. Engelhardt, S.W. Hell, *Parallelized STED fluorescence nanoscopy*, Optics Express 19 (24), 23716-23726, 2011

Selected for Virtual Journal for Biomedical Optics, Vol. 7, Iss. 1, 2011

In preparation

J. Chojnacki, T. Staudt, B. Glass, P. Bingen, J. Engelhardt, B. Müller, S. W. Hell, and H.-G. Kräusslich, *Virus Inside-Out Signaling: Maturation dependent redistribution of HIV-1 surface glycoproteins*, Science, 2012

C. Kempf, T. Staudt, P. Bingen, J. Kappes, H. Horstmann, J. Engelhardt, S. W. Hell and T. Kuner, *Multicolor tissue STED-nanoscopy of presynaptic protein distribution in a glutamatergic terminal at 38 nm focal plane resolution*, Frontiers in Neuroanatomy

C. Kempf, K. Reuter, P. Bingen, D. Barzan, T. Staudt, C. Körber, H. Horstmann, J. Engelhardt, D.-P. Herten, S.W. Hell, and T. Kuner, *Optical nanoscopy of presynaptic vesicle pools in a mammalian glutamatergic terminal using genetically encoded AGT-tag coupled with fluorescent quenched substrates*

STED on single strands of DNA

The following *first-author* publication was not in the main thrust of this thesis and the results were therefore not include therein.

In short, stimulated emission depletion (STED) nanoscopy on single DNA strands was demonstrated, revealing details with an up to five- to six-fold improved resolution over confocal microscopy. STED nanoscopy allowed features to be distinguished down to the persistence length of DNA ($\sim$ 50 nm) without promoting any significant additional photodamage, such as photobleaching or photonicking.

This short communication was submitted in both English and German.

Fluorescence Nanoscopy

DOI: 10.1002/anie.201100371

Fluorescence Nanoscopy of Single DNA Molecules by Using Stimulated Emission Depletion (STED)**

*F. Persson, P. Bingen, T. Staudt, J. Engelhardt, J. O. Tegenfeldt, and Stefan W. Hell**

Lens-based (far-field) fluorescence microscopy has played a key role in the life sciences, but for most of the time the resolution has been limited to about $\Delta r = \lambda/(2\text{NA}) > 200$ nm, with λ denoting the wavelength of light and NA the numerical aperture of the lens. However, since the 1990s microscopy concepts have emerged providing diffraction-unlimited resolution by inhibiting the fluorescence of the dye such that features closer than the diffraction limit Δr are forced to fluoresce sequentially.[1,2] Depending on how this fluorescence inhibition is implemented, the techniques broadly fall into two groups. In the group encompassing stimulated emission depletion (STED) microscopy,[2] the coordinate where the fluorophores are allowed to fluorescence is predetermined by a pattern of light in which the intensity reaches zero at a controllable position in space; in STED microscopy this light pattern typically has a doughnut shape. The second group of techniques enables the emission of fluorophores stochastically in space, such that just a single fluorophore is able to emit within a region of diameter $\Delta r = \lambda/(2\text{NA})$; the random emission coordinate is found by imaging the fluorescence with a camera, and then performing a centroid calculation.[3,4] In both groups, images below the diffraction limit are obtained by consecutively allowing a representative number of dye molecules to fluoresce.[1]

While most of these techniques have been applied to biological systems including DNA, high quality nanoscopy of DNA molecules has remained elusive.[5–7] This situation is unfortunate because many of DNA's functions, such as gene expression, are known to be regulated by bending, looping, supercoiling, and other conformational changes at subdiffraction length scales.[8] Many conformational changes of DNA appear in the range of 100–1000 basepairs, approximately 35–350 nm, with the persistence length of DNA (typically around 50 nm) defining a fundamental length scale. Additionally, to study the conformational changes and variations present in DNA, the given structure has to be not only uniformly labeled but also uniformly recorded. In particular, it is essential to be able to distinguish integral single strands of DNA from a strand that has been broken up into pieces or from multiple overlaid strands.[9]

These requirements for far-field optical nanoscopy of DNA strands stained with standard intercalating dyes, such as YOYO-1 (YOYO), suggest that the deterministic nature of STED nanoscopy may have an inherent advantage over the stochastic approach termed stochastic ground-state depletion followed by individual molecular return (GSDIM, later also called dSTORM).[10–12] Whereas stochastic techniques rely quadratically on the number of photons to localize an emitter with increased resolution, in STED nanoscopy a few photons from the sample are sufficient to identify a molecule. Also, for the stochastic methods, the localization accuracy decreases for slightly defocused dyes with fixed dipole moment,[13] which could be relevant for YOYO molecules, the transition dipole moment of which is linked to the helical pitch of the DNA by intercalation.[14] Moreover, the depletion of the ground state underlying GSDIM entails pumping the dye to a more reactive state,[10–12] potentially harming or breaking the DNA strand (e.g. through electron transfer).[5–7] In contrast, STED is designed to disallow excited states, thus protecting the molecule from photoreactions.[15] Last but not least, to ensure that all but one of the fluorophores are transferred to a dark state within a diffraction limited volume in GSDIM, the dye concentration has to be matched to the lifetime of the dark-state. Fulfilling this condition is challenging because the dye can assume a wide range of dark states along the DNA strand, featuring a broad spectrum of lifetimes.[5–7] Not matching them, results in discontinuously imaged DNA strands and hence in unreliable information about DNA conformation. This problem is especially true for DNA bending and looping points, where nanoscale resolution is critical. For all these reasons, we decided to explore STED nanoscopy for imaging single DNA molecules.

STED nanoscopy was performed by overlaying a pulsed excitation beam with a doughnut-shaped STED beam thus prohibiting the fluorescence of all the dye molecules exposed to the excitation light, except those lying within the center of the doughnut. Scanning the interlocked beams across the sample makes the object details fluoresce sequentially. Images were taken using two different pulsed wavelengths (568 nm and 647 nm) for STED. The asymmetrical dimeric cyanine dye, YOYO, is often used for single-molecule DNA

---

[*] Dr. F. Persson,[+] Prof. J. O. Tegenfeldt
Department of Physics, University of Gothenburg
Fysikgränd 3, 412 96 Gothenburg (Sweden)
P. Bingen,[+] Dr. T. Staudt, Dr. J. Engelhardt, Prof. S. W. Hell
Optical Nanoscopy Division, German Cancer Research Center (DKFZ)
Im Neuenheimer Feld 280, 69120 Heidelberg (Germany)
Fax: (+49) 6221-54-51210
E-mail: shell@gwdg.de

[+] These authors contributed equally.

[**] This work was supported by the EU's 7th Framework Programme (7RP/2007-2013) under grant agreement No. 201418 (READNA), the Swedish Research Council grants 2007-584 and 2007-4454, a Young Investigators' Grant from HSFP (RGY0078/2007-C) and a AFR PhD grant from the National Research Fund, Luxembourg (TR-PHD BFR08-059) and we thank Christoph Muus for preparing DNA samples.

Supporting information for this article is available on the WWW under http://dx.doi.org/10.1002/anie.201100371.

studies owing to its brightness and its fluorescence enhancement (ca. 500-fold) upon DNA binding. On the other hand, intercalating cyanines tend to promote photodamage of the DNA–dye complex, manifested by elevated bleaching and breaking (photonicking) of the DNA. Photonicking can be drastically reduced by removing oxygen in the buffer but the effect of oxygen on photobleaching remains unclear, although oxidation of DNA basepairs is believed to contribute to the observed bleaching.[16] We found that adding β-mercaptoethanol (BME) was effective in preventing both photonicking and bleaching. In the STED recordings, photostability was found to be highest for 20–50 photon counts per pixel (pixel size ca. 25 nm) at a pixel dwell time of 100 μs.

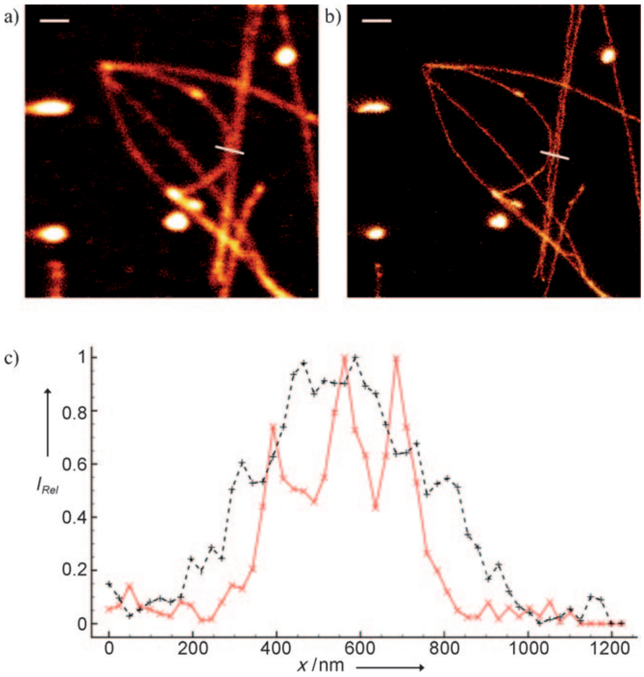

Figure 1. a) Confocal image of YOYO stained λ-DNA (basepair:dye 5:1). b) The corresponding STED image taken with $\lambda_{\text{STED}}=568$ nm (raw data). The STED image was acquired before the confocal counterpart. Scale bars: 1 μm. c) Average of three line profiles from the STED (solid red line) and confocal (dotted black line) images. Line profiles extracted along the white lines in (a) and (b). The three distinct peaks belonging to different DNA molecules are only resolved by STED.

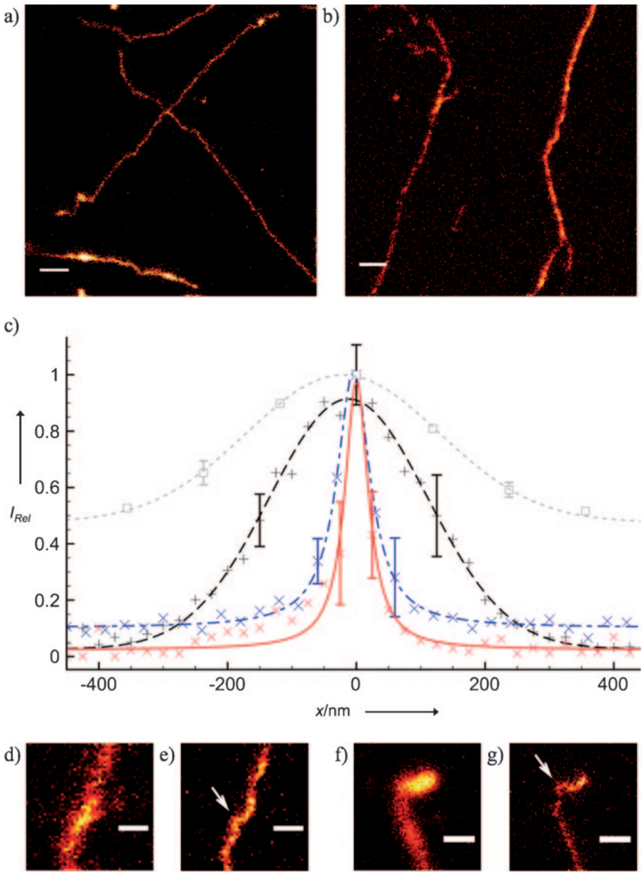

Figure 2. Typical raw STED images of YOYO stained λ-DNA (basepair:dye 5:1) using a) $\lambda_{\text{STED}}=568$ nm and b) $\lambda_{\text{STED}}=647$ nm. Scale bars in (a) and (b): 1 μm. c) Graph showing the average of 11 line profiles of a single DNA strand, with fits, for standard epifluorescence (dotted light gray line), confocal (dashed black line), and STED nanoscopy with $\lambda_{\text{STED}}=647$ nm (dash-dotted blue line) and 568 nm (solid red line); the corresponding full width at half maximum (FWHM) were found to be (300 ± 11) nm (Gaussian), (238 ± 5) nm (Gaussian), (62 ± 2) nm (Lorentzian), and (42 ± 3) nm (Lorentzian), respectively. The error bars correspond to one standard deviation. d)–g) Examples of DNA segments with bends and kinks visible (indicated by white arrows) in a STED image using e) $\lambda_{\text{STED}}=647$ nm and g) $\lambda_{\text{STED}}=568$ nm but not resolvable in the corresponding confocal images (d) and (f). Scale bars in (d)–(g): 500 nm.

Using STED at 568 nm we obtain a five- to sixfold improvement in resolution over standard confocal microscopy (Figure 1) that in turn already provides a marked improvement in contrast and resolution over epifluorescence microscopy (Figure 2c). In Figure 1, note the excellent correspondence of the variation in intensity along the DNA strands between the STED and confocal images. To explore the range of STED wavelengths that can be applied in our system we also used STED at 647 nm where the YOYO emission is a mere 3% of its maximum. The result is a three- to fourfold improvement in resolution over standard confocal microscopy (Figure 2), thus demonstrating the applicability of STED over a range of over 80 nm. Kinks occur along DNA and can be sequence specific or due to the binding of proteins or small molecules. Figure 2 shows how STED, but not confocal microscopy can readily be used to identify these subtle structures along the DNA.

To investigate the photodamage inflicted by the STED beam on the DNA–dye complex (basepair:dye 5:1), a confocal image, an STED image ($\lambda_{\text{STED}}=568$ nm), and then a confocal image were acquired one after another. While the second confocal image displayed a (50 ± 9) % lower fluorescence level because of bleaching, photonicking was not observed, neither in the STED nor in the second confocal recording. Another series with three consecutive confocal images revealed a reduction of the fluorescence level by (34 ± 16) %. Thus with STED the difference to photobleaching from standard confocal imaging is not significant. For details regarding imaging using a lower dye ratio (compatible with single-molecule investigations of DNA–enzyme interactions) see Supporting Information.

In conclusion, we have demonstrated STED nanoscopy for DNA imaging at a resolution of approximately 45 nm, which is comparable to the persistence length, the fundamental length scale of the polymer physics of DNA. The variation in fluorescence signal over the DNA molecule corresponds well with that obtained by confocal microscopy, demonstrating the viability of STED for imaging single DNA molecules and a future potential use for comparison of signal variations caused by sequence specific dye binding or partial melting. The demonstrated combination of resolution and uniformity of imaging along the DNA strand is critical for visualizing small conformational changes as well as for optical mapping of DNA.[9] Importantly, STED can be applied over a relatively large wavelength range (at least 80 nm), with longer wavelengths being generally less prone to inducing photodamage, while still providing a marked resolution improvement. By employing molecular transitions between the two most basic states of a fluorophore, that is, the ground and the first electronically excited state, we anticipate STED will become the preferred optical pathway to exploring DNA at the molecular level.

Experimental Section

λ-bacteriophage DNA (Amersham Biosciences, UK) was stained with YOYO-1 (Invitrogen, USA) to obtain the basepair:dye ratios of 5:1 and 20:1. Prior to experiments the stained DNA was diluted to 1 μg mL^{-1} using degassed 0.5 × tris-borate-EDTA (TBE) buffer containing 5 v/v % β-mercaptoethanol (Sigma Aldrich Corp., USA) and stretched on poly-L-lysine coated glass slides. For more details see Supporting Information.

Excitation of DNA was performed using a pulsed laser diode (Picoquant, Germany) emitting at $\lambda_{exc} = 470$ nm, with a peak irradiation of 15–65 kW cm^{-2} in the focal plane (time-average power of 1–4 μW), synchronized with a STED-laser at $\lambda_{STED} = 568$ nm and 647 nm by a fast photodiode (OCF-401, Becker & Hickl GmbH, Germany). STED was performed using an actively mode-locked (APE, Germany) krypton laser (Coherent Inc., USA) creating pulse widths of 1.5 ns (568 nm) and 300 ps (647 nm) at a repetition rate of 71.25 MHz and peak irradiations of 20–30 MW cm^{-2} (568 nm) and 210–360 MW cm^{-2} (647 nm) in the focal plane (time-average power of 45–70 mW (568 nm) and 130–220 mW (647 nm)). A vortex phase plate (RPC Photonics, USA) was used to generate a doughnut-shaped focal spot for STED. The excitation and STED beams were combined using acousto-optical tunable filters (Crystal Technologies, USA) and coupled into a microscope stand (DMI 4000B, Leica Microsystems GmbH, Germany) equipped with a 63 × (NA 1.30, Leica) oil immersion objective and a three-axis piezo stage-scanner (PI, Germany). The emitted fluorescence passed through a band-pass filter (HQ510/40M, Chroma, USA) and was detected confocally with an avalanche photo diode (SPCM-AQR-13-FC, PerkinElmer Inc., USA) using a data acquisition software (Imspector, MPI Göttingen, Germany). Pixel sizes of 25 nm for $\lambda_{STED} = 568$ nm and 40 nm for $\lambda_{STED} = 647$ nm were chosen at a pixel dwell time of 100 μs. The corresponding confocal images were recorded using the same parameters.

Received: January 15, 2011

Keywords: DNA · dyes/pigments · fluorescence · single-molecule studies · stimulated emission depletion (STED)

---

[1] S. W. Hell, *Science* **2007**, *316*, 1153 – 1158.
[2] S. W. Hell, J. Wichmann, *Opt. Lett.* **1994**, *19*, 780 – 782.
[3] M. J. Rust, M. Bates, X. W. Zhuang, *Nat. Methods* **2006**, *3*, 793 – 795.
[4] E. Betzig, G. H. Patterson, R. Sougrat, O. W. Lindwasser, S. Olenych, J. S. Bonifacino, M. W. Davidson, J. Lippincott-Schwartz, H. F. Hess, *Science* **2006**, *313*, 1642 – 1645.
[5] C. Flors, N. J. Ravarani, D. T. F. Dryden, *ChemPhysChem* **2009**, *10*, 2201 – 2204.
[6] C. Flors, *Biopolymers* **2011**, *95*, 290 – 297.
[7] C. Flors, *Photochem. Photobiol. Sci.* **2010**, *9*, 643 – 648.
[8] J. M. G. Vilar, L. Saiz, *Curr. Opin. Genet. Dev.* **2005**, *15*, 136 – 144.
[9] E. T. Dimalanta, A. Lim, R. Runnheim, C. Lamers, C. Churas, D. K. Forrest, J. J. de Pablo, M. D. Graham, S. N. Coppersmith, S. Goldstein, D. C. Schwartz, *Anal. Chem.* **2004**, *76*, 5293 – 5301.
[10] H. Bock, C. Geisler, C. A. Wurm, C. Von Middendorff, S. Jakobs, A. Schonle, A. Egner, S. W. Hell, C. Eggeling, *Appl. Phys. B* **2007**, *88*, 161 – 165.
[11] J. Fölling, M. Bossi, H. Bock, R. Medda, C. A. Wurm, B. Hein, S. Jakobs, C. Eggeling, S. W. Hell, *Nat. Methods* **2008**, *5*, 943 – 945.
[12] M. Heilemann, S. van de Linde, M. Schuttpelz, R. Kasper, B. Seefeldt, A. Mukherjee, P. Tinnefeld, M. Sauer, *Angew. Chem.* **2008**, *120*, 6266 – 6271; *Angew. Chem. Int. Ed.* **2008**, *47*, 6172 – 6176.
[13] J. Engelhardt, J. Keller, P. Hoyer, M. Reuss, T. Staudt, S. W. Hell, *Nano Lett.* **2011**, *11*, 209 – 213.
[14] F. Persson, F. Westerlund, J. O. Tegenfeldt, A. Kristensen, *Small* **2009**, *5*, 190 – 193.
[15] J. Hotta, E. Fron, P. Dedecker, D. P. F. Janssen, C. Li, K. Müllen, B. Harke, J. Bückers, S. W. Hell, J. Hofkens, *J. Am. Chem. Soc.* **2010**, *132*, 5021 – 5023.
[16] C. Kanony, B. Akerman, E. Tuite, *J. Am. Chem. Soc.* **2001**, *123*, 7985 – 7995.

DOI: 10.1002/ange.201100371

Fluoreszenznanoskopie einzelner DNA-Moleküle mit Fluoreszenzverhinderung durch stimulierte Emission (STED)**

*F. Persson, P. Bingen, T. Staudt, J. Engelhardt, J. O. Tegenfeldt und Stefan W. Hell**

Für die Lebenswissenschaften spielt die Fluoreszenzmikroskopie eine wichtige Rolle, obwohl ihre Auflösung lange auf $\Delta r = \lambda/(2\text{NA}) > 200$ nm begrenzt war. (λ ist die Wellenlänge des Lichtes und NA die numerische Apertur des Objektivs.) Mitte der 1990er Jahre entstanden neue Mikroskopiekonzepte, die Auflösungen jenseits dieser Beugungsgrenze ermöglichen. Diesen Konzepten folgend schaltet man die Fluoreszenz des Farbstoffes so aus, dass Objekte, die näher als Δr zusammenliegen, gezwungen werden, nacheinander zu fluoreszieren.[1,2] Je nachdem, wie dieses Ausschalten umgesetzt wird, unterscheidet man zwei Gruppen: Die erste Gruppe umfasst unter anderem die STED-Mikroskopie (STED = Stimulated Emission Depletion, stimulierte Emissionslöschung);[2] hier ist die Koordinate, an der Fluoreszenz erlaubt ist, durch ein Lichtmuster vorgegeben, das eine Intensitätsverteilung mit einer kontrollierbaren Nullstelle aufweist, z. B. ein Doughnut-Muster. Die zweite Gruppe ermöglicht Fluorophoren stochastisches Emittieren im Raum in der Weise, dass innerhalb eines Durchmessers von $\lambda/(2\text{NA})$ nur ein einzelner Fluorophor leuchtet. Die Emissionskoordinate wird dann bestimmt, indem man die Fluoreszenz auf eine Kamera abbildet, gefolgt von einer Schwerpunktsberechnung.[3,4] In beiden Gruppen sind Abbildungen unterhalb der Beugungsgrenze möglich, indem man nacheinander eine repräsentative Zahl von Farbstoffmolekülen des Objekts fluoreszieren lässt und nachweist.[1]

Während einige dieser Techniken bereits auf DNA-Systeme angewendet wurden, gelang bisher noch keine qualitativ hochwertige Nanoskopie an DNA-Molekülen.[5–7] Dies ist bedauerlich, da viele Funktionen (wie die Genexpression) dafür bekannt sind, durch Biegen, Schleifenbildung, Supercoiling und anderen Konformationsänderungen reguliert zu werden, und zwar auf Längenskalen unterhalb der Beugungsgrenze.[8] Viele Konformationsänderungen der DNA geschehen im Bereich von 100 bis 1000 Basenpaaren, entsprechend 35 bis 350 nm, mit der Persistenzlänge von DNA (normalerweise ca. 50 nm) als grundlegender Längenskala. Um Konformationsänderungen und Variationen der DNA zu untersuchen, muss man sicherstellen, dass die vorgegebene Struktur nicht nur durchgehend gefärbt, sondern auch durchgehend detektiert wird. Insbesondere muss zwischen zusammenhängenden DNA-Strängen, in mehrere Teilstücke zerbrochenen Strängen und Anordnungen aus mehreren überlagerten Strängen unterschieden werden können.[9]

Diese Anforderungen an die optische Nanoskopie von DNA-Strängen, die mit handelsüblichen interkalierenden Farbstoffen wie YOYO-1 (YOYO) gefärbt sind, lassen vermuten, dass die deterministische Natur der STED-Nanoskopie einen grundlegenden Vorteil gegenüber dem stochastischen Ansatz, der „stochastic ground state depletion followed by individual molecule return“ (GSDIM, später auch dSTORM genannt), hat.[10–12] Während bei der STED-Nanoskopie wenige Photonen aus der Probe ausreichen, um ein Molekül zu identifizieren, hängt die Auflösung stochastischer Techniken im Wesentlichen quadratisch von der Zahl der Photonen ab. Die Genauigkeit wird weiter verringert, wenn Farbstoffmoleküle mit festem Dipolmoment nicht genau im Fokus liegen;[13] für YOYO-Moleküle ist dies nicht unwahrscheinlich, da ihr Übergangsdipolmoment durch Interkalation an helikale DNA gekoppelt ist.[14] Zudem führt eine Grundzustandsentvölkerung dazu, dass der Farbstoff in einen reaktiveren Zustand gepumpt wird.[10–12] Dies hat möglicherweise Schädigungen oder Brüche der DNA-Stränge zur Folge (z. B. durch Elektronentransfer),[5–7] liegt aber der GSDIM-Methode zugrunde. Im Unterschied dazu ist STED so konzipiert, dass das Molekül in den Grundzustand gepumpt wird und so vor Photoreaktionen geschützt sein sollte.[15] Um sicherzustellen, dass bei GSDIM nur ein Fluorophor von einem dunklen in einen hellen Zustand innerhalb eines beugungsbegrenzten Volumens übergeht, muss man letztlich die Farbstoffkonzentration an die Lebensdauer des Dunkelzustandes anpassen. Dies ist schwierig, weil der Farbstoff-DNA-Komplex viele Dunkelzustände entlang des DNA-Stranges annehmen kann.[5–7] Wenn diese Bedingung aber nicht erfüllt ist, erfolgt die Abbildung der DNA-Stränge und -Konformationen nicht durchgehend bzw. unzuverlässig. Dies gilt besonders für Punkte, an denen Biegungen und Schleifenbildung auftreten; hier ist eine nanoskalige Auflösung besonders wichtig. Aus all diesen Gründen haben wir uns dazu

---

[*] Dr. F. Persson,[+] Prof. J. O. Tegenfeldt
Fakultät für Physik, Universität Göteborg
Fysikgränd 3, 412 96 Göteborg (Schweden)
P. Bingen,[+] Dr. T. Staudt, Dr. J. Engelhardt, Prof. S. W. Hell
Abteilung Optische Nanoskopie,
Deutsches Krebsforschungszentrum (DKFZ)
Im Neuenheimer Feld 280, 69120 Heidelberg (Deutschland)
Fax: (+49) 6221-54-51210
E-Mail: shell@gwdg.de

[+] Diese Autoren haben zu gleichen Teilen zu dieser Arbeit beigetragen.

[**] Diese Arbeit wurde durch das 7. EU-Rahmenprogramm (7RP/2007-2013; Fördernummer 201418 (READNA)), Fördermittel des schwedischen Forschungsrates (2007-584 und 2007-4454), eine Young-Investigators-Förderung vom HSFP (RGY0078/2007-C) und ein AFR-PhD-Stipendium vom Nationalen Forschungsfonds, Luxemburg (TR-PHD BFR08-059) unterstützt. Wir danken Christoph Muus für das Vorbereiten von DNA-Proben sowie Patrick Hoyer und Matthias Reuss für die kritische Durchsicht der Übersetzung.

Hintergrundinformationen zu diesem Beitrag sind im WWW unter http://dx.doi.org/10.1002/ange.201100371 zu finden.

entschlossen, einzelne DNA-Moleküle mit STED-Nanoskopie zu untersuchen.

Bei der von uns eingesetzten STED-Nanoskopie wird ein gepulster Anregungsstrahl mit einem Doughnut-förmigen STED-Strahl überlagert. Dieser verbietet es allen Farbstoffmolekülen, die dem Anregungslicht ausgesetzt sind, zu fluoreszieren, mit Ausnahme derjenigen, die im Zentrum des Doughnuts liegen. Durch Rastern der zeitlich gekoppelten Strahlen über die Probe werden die Details des fluoreszierenden Objekts zeitlich nacheinander aufgenommen.

Die Bilder wurden mit zwei unterschiedlichen, gepulsten STED-Wellenlängen (568 und 647 nm) aufgenommen. Der asymmetrische, dimere Cyaninfarbstoff YOYO wird wegen seiner Helligkeit und der 500fachen Fluorenszenzerhöhung nach Interkalation häufig für Einzelmolekül-DNA-Studien verwendet. Allerdings neigen interkalierende Cyaninfarbstoffe dazu, Lichtschäden an DNA-Farbstoff-Komplexen zu fördern, was sich in erhöhtem Bleichen und Brechen der DNA (Photonicking) bemerkbar macht. Photonicking kann drastisch reduziert werden, indem Sauerstoff aus dem Puffer entfernt wird. Die Wirkung von Sauerstoff auf das Bleichen bleibt bislang jedoch unklar; die Oxidation der DNA-Basenpaare trägt vermutlich zur Bleichwirkung bei.[16] Wir fanden heraus, dass die Zugabe von β-Mercaptoethanol (BME) sowohl Photonicking als auch Bleichen reduziert. In den STED-Aufnahmen wurde festgestellt, dass die höchste Photostabilität bei Aufnahmen mit 20–50 Photonen pro Pixel (mit einer Pixelgröße von ca. 25 nm) bei einer Pixelintegrationszeit von 100 µs erreicht wurde.

Mit einem STED-Strahl bei 568 nm erhalten wir eine 5–6-mal bessere Auflösung gegenüber derjenigen von normaler, konfokaler Mikroskopie (Abbildung 1), die ihrerseits bereits eine deutliche Verbesserung bezüglich Kontrast und Auflösung gegenüber der Epifluoreszenzmikroskopie (Abbildung 2c) bietet. Man beachte die Übereinstimmung in der Variation der Intensität entlang der DNA-Stränge zwischen den STED- und den konfokalen Bildern (Abbildung 1). Um zu untersuchen, über welchen Wellenlängenbereich STED noch wirksam ist, wurde STED an DNA auch bei 647 nm gemessen, wo die Emissionsintensität von YOYO nur noch 3 % des Maximums beträgt. Dennoch ist die DNA 3–4-mal besser aufgelöst als bei herkömmlicher konfokaler Mikroskopie (Abbildung 2). Dies belegt die Anwendbarkeit von STED über einen Bereich von 80 nm. Knicke entlang der DNA können durch eine spezifische DNA-Sequenz oder durch die Bindung von Proteinen oder kleinen Molekülen auftreten. Abbildung 2 zeigt, dass STED diese feinen Strukturen auflösen kann, die konfokaler Mikroskopie verborgen bleiben.

Zur Untersuchung der komplexen Lichtschäden, die der DNA durch den STED-Strahl zugefügt werden (Basenpaar/Farbstoff 5:1), wurden nacheinander ein konfokales Bild, ein STED-Bild und ein weiteres konfokales Bild aufgenommen ($\lambda_{\mathrm{STED}} = 568$ nm). Während das zweite konfokale Bild eine (50 ± 9) % niedrigere Fluoreszenz durch Bleichen aufweist, wurde weder im STED noch in der zweiten konfokalen Aufnahme Photonicking beobachtet. Eine weitere Serie mit drei aufeinander folgenden konfokalen Bildern zeigte eine Verringerung des Fluoreszenzsignals um (34 ± 16) %. STED hat zwar eine Bleichwirkung, die sich aber kaum von der bei einer gewöhnlichen, konfokalen Messung unterscheidet. Weitere Einzelheiten bezüglich STED-Messungen mit einem niedrigeren Farbstoff/DNA-Verhältnis (kompatibel mit Einzelmolekülstudien von DNA-Protein-Interaktionen) finden sich in den Hintergrundinformationen.

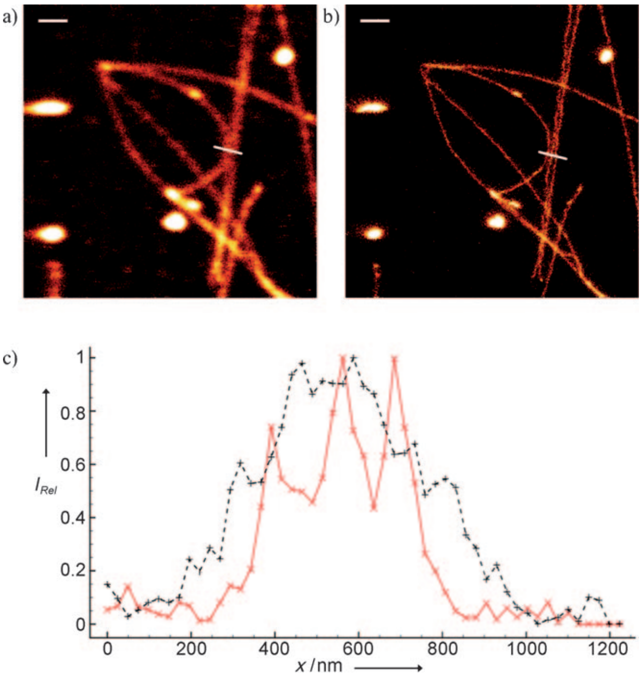

Abbildung 1. a) Konfokale Abbildung von mit YOYO gefärbter λ-DNA (Basenpaar/Farbstoff 5:1) mit b) dem entsprechenden STED-Bild (Rohdaten). Das STED-Bild ist vor dem konfokalen aufgenommen worden. Maßstab: 1 µm. c) Durchschnitt dreier Linienprofile aus dem STED- (durchgezogene, rote Linie) und dem konfokalen Bild (gestrichelte, schwarze Linie). Die Linienprofile entstammen der Position der weißen Linien in den obigen Bildern. Die drei deutlichen Spitzen mit unterschiedlichen DNA-Molekülen werden nur mit STED aufgelöst.

Wir haben hier gezeigt, dass STED-Nanoskopie Aufnahmen von DNA bei einer Auflösung von ca. 45 nm ermöglicht. Dieser Wert ist vergleichbar mit der Persistenzlänge freier DNA, einer grundlegenden Längenskala der Polymerphysik. Die Variation des Fluoreszenzsignals entlang des DNA-Moleküls stimmt gut mit der von konfokaler Mikroskopie überein. Dies belegt die Anwendbarkeit von STED auf die Bildgebung einzelner DNA-Moleküle und eine künftige mögliche Verwendung für die Untersuchung von Signalvariationen, die aus sequenzspezifischer Farbstoffbindung oder teilweises Schmelzen der DNA resultieren. Die von uns gezeigte Kombination von Hochauflösung und Durchgängigkeit des Signals ist von entscheidender Bedeutung für die Visualisierung kleiner Konformationsänderungen sowie für die optische Abbildung von DNA.[9] Außerdem konnten wir zeigen, dass STED über einen relativ breiten Wellenlängenbereich (mindestens 80 nm) angewendet werden kann. Bei größeren Wellenlängen werden in der Regel weniger Lichtschäden induziert, die Auflösungsverbesserung ist gleichwohl noch deutlich. Da die STED-Technik auf molekularen Übergängen zwischen den beiden grundlegenden Zuständen eines Fluo-

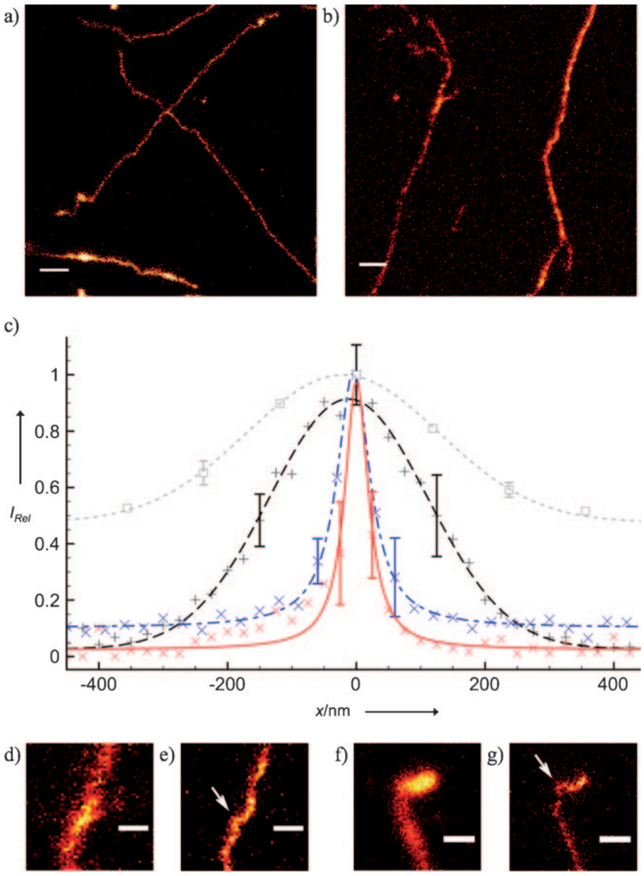

Abbildung 2. Typische STED-Rohdaten-Bilder von mit YOYO gefärbter λ-DNA (Basenpaar/Farbstoff 5:1) unter Anwendung von a) $\lambda_{STED} = 568$ nm und b) $\lambda_{STED} = 647$ nm. Maßstab in (a) und (b): 1 µm. c) Eine Kurve zeigt den Durchschnitt von elf Linienprofilen eines einzigen DNA-Strangs, mit zugehörigen Profilen der Epifluoreszenz (gepunktete, hellgraue Linie), konfokalen (gestrichelte, schwarze Linie) und STED-Nanoskopie mit $\lambda_{STED} = 647$ nm (strichgepunktete, blaue Linie) und 568 nm (durchgezogene, rote Linie); die entsprechenden Halbwertsbreiten wurden durch Anlegen von Ausgleichskurven zu (300 ± 11) nm (Gauß), (238 ± 5) nm (Gauß), (62 ± 2) nm (Lorentz) bzw. (42 ± 3) nm (Lorentz) bestimmt. Die Fehlerbalken entsprechen einer Standardabweichung. Beispiele von DNA-Segmenten mit Biegungen und Knicken, die sichtbar im STED-Bild unter Anwendung von e) $\lambda_{STED} = 647$ nm und g) $\lambda_{STED} = 568$ nm, jeweils aber nicht auflösbar in den entsprechenden konfokalen Bildern (d) und (f) sind. Maßstab in (d)–(g): 500 nm.

rophors, d. h. dem Grundzustand und dem ersten elektronisch angeregten Zustand, beruht, erwarten wir, dass sie sich zur bevorzugten Methode für die optische Erforschung der DNA auf molekularer Ebene entwickeln wird.

Experimentelles

λ-Bakteriophagen-DNA (Amersham Biosciences) wurde mit YOYO-1 (Invitrogen) gefärbt, mit einem Basenpaar/Farbstoff-Verhältnis von 5:1 und 20:1. Vor den Experimenten wurde die gefärbte DNA auf 1 µg mL^{-1} mit entgastem 0.5 × Tris-Borat-EDTA(TBE)-Puffer und 5% (v/v) β-Mercaptoethanol (Sigma Aldrich) verdünnt und auf mit Poly-L-Lysin beschichteten Deckgläschen gestreckt. Details siehe Hintergrundinformationen.

Die Anregung der DNA erfolgte mit einer gepulsten Laserdiode (PicoQuant) mit Emission bei $\lambda_{Anregung} = 470$ nm mit einem Spitzenbestrahlungswert von 15–65 kW cm^{-2} in der Probe (durchschnittliche Leistung von 1–4 µW), synchronisiert mit einem STED-Laser bei $\lambda_{STED} = 568$ und 647 nm über eine schnelle Photodiode (OCF-401; Becker & Hickl GmbH). Der STED-Strahl wurde mit einem aktiv modengekoppelten (APE) Krypton-Laser (Coherent Inc.) erzeugt, mit Pulsbreiten von 1.5 ns (568 nm) und 300 ps (647 nm) bei einer Wiederholrate von 71.25 MHz und Höchstbestrahlungen von 20–30 MW cm^{-2} (568 nm) und 210–360 cm^{-2} MW (647 nm) in der Probe (Durchschnittsleistung von 45–70 mW (568 nm) oder 130–220 mW (647 nm)). Eine Vortex-Phasenplatte (RPC Photonics) wurde verwendet, um den für STED notwendigen Doughnut zu generieren. Die Anregungs-und STED-Strahlen wurden mit akustooptischen Filtern (Crystal Technologies) kombiniert und in ein Stativ (DMI 4000B; Leica Microsystems GmbH) eingekoppelt, das mit einem 63 × (NA 1.30, Leica)-Ölimmersionsobjektiv und einem Drei-Achsen-Piezo-Scanner (PI) ausgestattet ist. Die emittierte Fluoreszenz wurde durch einen Band-Pass-Filter (HQ510/40M; Chroma) gefiltert und konfokal mit einer Avalanche Photodiode (SPCM-AQR-13-FC; PerkinElmer) und einer Datenerfassungs-Software (ImSpector, MPI Biophysikalische Chemie Göttingen) detektiert. Die Pixelgrößen betrugen 25 und 40 nm für $\lambda_{STED} = 568$ bzw. 647 nm bei einer Pixelintegrationszeit von 100 µs. Die entsprechenden konfokalen Bilder wurden mit den gleichen Parametern aufgenommen.

Eingegangen am 15. Januar 2011

Stichwörter: DNA · Einzelmoleküluntersuchungen · Farbstoffe/Pigmente · Fluoreszenz · Stimulierte Emissionslöschung

[1] S. W. Hell, *Science* **2007**, *316*, 1153–1158.
[2] S. W. Hell, J. Wichmann, *Opt. Lett.* **1994**, *19*, 780–782.
[3] M. J. Rust, M. Bates, X. W. Zhuang, *Nat. Methods* **2006**, *3*, 793–795.
[4] E. Betzig, G. H. Patterson, R. Sougrat, O. W. Lindwasser, S. Olenych, J. S. Bonifacino, M. W. Davidson, J. Lippincott-Schwartz, H. F. Hess, *Science* **2006**, *313*, 1642–1645.
[5] C. Flors, N. J. Ravarani, D. T. F. Dryden, *ChemPhysChem* **2009**, *10*, 2201–2204.
[6] C. Flors, *Biopolymers* **2011**, *95*, 290–297.
[7] C. Flors, *Photochem. Photobiol. Sci.* **2010**, *9*, 643–648.
[8] J. M. G. Vilar, L. Saiz, *Curr. Opin. Genet. Dev.* **2005**, *15*, 136–144.
[9] E. T. Dimalanta, A. Lim, R. Runnheim, C. Lamers, C. Churas, D. K. Forrest, J. J. de Pablo, M. D. Graham, S. N. Coppersmith, S. Goldstein, D. C. Schwartz, *Anal. Chem.* **2004**, *76*, 5293–5301.
[10] H. Bock, C. Geisler, C. A. Wurm, C. Von Middendorff, S. Jakobs, A. Schonle, A. Egner, S. W. Hell, C. Eggeling, *Appl. Phys. B* **2007**, *88*, 161–165.
[11] J. Fölling, M. Bossi, H. Bock, R. Medda, C. A. Wurm, B. Hein, S. Jakobs, C. Eggeling, S. W. Hell, *Nat. Methods* **2008**, *5*, 943–945.
[12] M. Heilemann, S. van de Linde, M. Schuttpelz, R. Kasper, B. Seefeldt, A. Mukherjee, P. Tinnefeld, M. Sauer, *Angew. Chem.* **2008**, *120*, 6266–6271; *Angew. Chem. Int. Ed.* **2008**, *47*, 6172–6176.
[13] J. Engelhardt, J. Keller, P. Hoyer, M. Reuss, T. Staudt, S. W. Hell, *Nano Lett.* **2011**, *11*, 209–213.
[14] F. Persson, F. Westerlund, J. O. Tegenfeldt, A. Kristensen, *Small* **2009**, *5*, 190–193.
[15] J. Hotta, E. Fron, P. Dedecker, D. P. F. Janssen, C. Li, K. Müllen, B. Harke, J. Bückers, S. W. Hell, J. Hofkens, *J. Am. Chem. Soc.* **2010**, *132*, 5021–5023.
[16] C. Kanony, B. Akerman, E. Tuite, *J. Am. Chem. Soc.* **2001**, *123*, 7985–7995.

Bibliography

[1] E. Abbe. Beiträge zur Theorie des Mikroskops und der mikroskopischen Wahrnehmung. *Archiv für Mikroskopische Anatomie*, 9:413–468, 1873.

[2] P. W. Ambrose, P. M. Goodwin, J. Enderlein, D. J. Semin, J. C. Martin, and R. A. Keller. Fluorescence photon antibunching from single molecules on a surface. *Chemical Physics Letters*, 269(3–4):365–370, 1997.

[3] V. Andresen, A. Egner, and S. W. Hell. Time-multiplexed multifocal multiphoton microscope. *Optics Letters*, 26(2):75–77, 2001.

[4] P. Annibale, S. Vanni, M. Scarselli, U. Rothlisberger, and A. Radenovic. Quantitative photo activated localization microscopy: Unraveling the effects of photoblinking. *PLoS ONE*, 6(7):e22678, 2011.

[5] D. Aquino, A. Schönle, C. Geisler, C. v. Middendorff, C. A. Wurm, Y. Okamura, T. Lang, S. W. Hell, and A. Egner. Two-color nanoscopy of three-dimensional volumes by 4pi detection of stochastically switched fluorophores. *Nature Methods*, 8(4):353 – 359, 2011.

[6] E. Auksorius, B. R. Boruah, C. Dunsby, P. M. P. Lanigan, G. Kennedy, M. A. A. Neil, and P. M. W. French. Stimulated emission depletion microscopy with a supercontinuum source and fluorescence lifetime imaging. *Optics Letters*, 33(2):113–115, 2008.

[7] T. Basche, W. E. Moerner, M. Orrit, and H. Talon. Photon antibunching in the fluorescence of a single molecule trapped in a solid. *Physical Review Letters*, 69(10):1516–1519, 1992.

[8] E. Betzig, G. H. Patterson, R. Sougrat, O. W. Lindwasser, S. Olenych, J. S. Bonifacino, M. W. Davidson, J. Lippincott-Schwartz, and H. F. Hess. Imaging intracellular fluorescent proteins at nanometer resolution. *Science*, 313(5793):1642–1645, 2006.

[9] J. Bewersdorf, R. Pick, and S. W. Hell. Multifocal multiphoton microscopy. *Optics Letters*, 23:655–657, 1998.

[10] G. Binnig, C. F. Quate, and C. Gerber. Atomic force microscope. *Physical Review Letters*, 56:930–933, 1986.

[11] M. Born and E. Wolf. *Principles of Optics*. Cambridge University Press, Cambridge, New York, Melbourne, Madrid, Cape Town, 7th edition, 2002.

[12] T. Brakemann, A. C. Stiel, G. Weber, M. Andresen, I. Testa, T. Grotjohann, M. Leutenegger, U. Plessmann, H. Urlaub, C. Eggeling, M. C. Wahl, S. W. Hell, and S. Jakobs. A reversibly photoswitchable gfp-like protein with fluorescence excitation decoupled from switching. *Nature Biotechnology*, 29(10):942–7, 2011.

[13] J. Bückers, D. Wildanger, G. Vicidomini, L. Kastrup, and S. W. Hell. Simultaneous multi-lifetime multi-color sted imaging for colocalization analyses. *Optics Express*, 19(4):3130 – 3143, 2011.

[14] M. Chalfie, Y. Tu, G. Euskirchen, W. W. Ward, and D. C. Prasher. Green fluorescent protein as a marker for gene-expression. *Science*, 263:802–805, 1994.

[15] A. H. Coons, H. J. Creech, R. N. Jones, and E. Berliner. The demonstration of pneumococcal antigen in tissues by the use of fluorescent antibody. *The Journal of Immunology*, 45(3):159–170, 1942.

[16] A. H. Coons and M. H. Kaplan. Localization of antigen in tissue cells. *The Journal of Experimental Medicine*, 91(1):1–13, 1950.

[17] W. Denk, J. H. Strickler, and W. W. Webb. 2-photon laser scanning fluorescence microscopy. *Science*, 248:73–76, 1990.

[18] T. Dertinger, V. Pacheco, I. von der Hocht, R. Hartmann, I. Gregor, and J. Enderlein. Two-focus fluorescence correlation spectroscopy: A new tool for accurate and absolute diffusion measurements. *ChemPhysChem*, 8(3):433 – 443, 2007.

[19] G. Donnert, C. Eggeling, and S. W. Hell. Major signal increase in fluorescence microscopy through dark-state relaxation. *Nature Methods*, 4(1):81–86, 2007.

[20] R. C. Dunn. Near-field scanning optical microscopy. *Chemistry Reviews*, 99:2891–2927, 1999.

[21] A. Egner and S. W. Hell. Time multiplexing and parallelization in multifocal multiphoton microscopy. *Optical Society of America. Journal A: Optics, Image Science, and Vision*, 17:1192–1201, 2000.

[22] J. Engelhardt, J. Keller, P. Hoyer, M. Reuss, T. Staudt, and S. W. Hell. Molecular orientation affects localization accuracy in superresolution far-field fluorescence microscopy. *Nano Letters*, 11(209-213), 2010.

[23] J. Fischer, G. Freymann, and M. Wegener. The materials challenge in diffraction-unlimited direct-laser-writing optical lithography. *Advanced Materials*, 22(32):3578–3582, 2010.

[24] W. Flemming. *Zellsubstanz, Kern und Zelltheilung*. Vogel, 1882.

[25] G. Ghosh. Dispersion-equation coefficients for the refractive index and birefringence of calcite and quartz crystals. *Optics Communications*, 163(1–3):95–102, 1999.

[26] T. Grotjohann, I. Testa, M. Leutenegger, H. Bock, N. T. Urban, F. Lavoie-Cardinal, K. I. Willig, C. Eggeling, S. Jakobs, and S. W. Hell. Diffraction-unlimited all-optical imaging and writing with a photochromic gfp. *Nature*, 478(7368):204–208, 2011.

[27] M. Gu. *Advanced Optical Imaging Theory*. Springer-Verlag, 2000.

[28] M. G. L. Gustafsson. Nonlinear structured-illumination microscopy: Wide-field fluorescence imaging with theoretically unlimited resolution. *Proceedings of the National Academy of Sciences of the United States of America*, 102(37):13081–13086, 2005.

[29] R. Hanbury Brown and R. Q. Twiss. Correlation between photons in two coherent beams of light. *Nature*, 177(4497):27–29, 1956.

[30] R. Hein and R. Y. Tsien. Engineering green fluorescent protein for improved brightness, longer wavelengths and fluorescence resonance energy transfer. *Current Biology*, 6:178–182, 1996.

[31] T. Heinlein, P. Schlueter, D. P. Herten, M. Sauer, and J. Wolfrum. Counting single molecules in living cells at high resolution by spectrally resolved fluorescence lifetime imaging microscopy (sflim) and coincidence analysis. *SPIE: Imaging, Manipulation, and Analysis of Biomolecules and Cells: Fundamentals and Applications III*, 5699:141–148, 2005.

[32] R. Heintzmann, T. M. Jovin, and C. Cremer. Saturated patterned excitation microscopy - a concept for optical resolution improvement. *Optical Society of America. Journal A: Optics, Image Science, and Vision*, 19(8):1599–1609, 2002.

[33] S. W. Hell. Far-field optical nanoscopy. *Science*, 316(5828):1153–1158, 2007.

[34] S. W. Hell and M. Kroug. Ground-state depletion fluorescence microscopy, a concept for breaking the diffraction resolution limit. *Applied Physics B: Lasers and Optics*, 60:495–497, 1995.

[35] S. W. Hell, R. Schmidt, and A. Egner. Diffraction-unlimited three-dimensional optical nanoscopy with opposing lenses. *Nature Photonics*, 3:381–387, 2009.

[36] S. W. Hell, J. Soukka, and P. E. Haenninen. Two- and multiphoton detection as an imaging mode and means of increasing the resolution in far-field light microscopy. *Bioimaging*, 3:65–69, 1995.

[37] S. W. Hell and E. H. K. Stelzer. Properties of a 4pi confocal fluorescence microscope. *Optical Society of America. Journal A: Optics, Image Science, and Vision*, 9:2159–2166, 1992.

[38] S. W. Hell and J. Wichmann. Breaking the diffraction resolution limit by stimulated-emission - stimulated-emission-depletion fluorescence microscopy. *Optics Letters*, 19(11):780–782, 1994.

[39] S. T. Hess, T. P. K. Girirajan, and M. D. Mason. Ultra-high resolution imaging by fluorescence photoactivation localization microscopy. *Biophysical Journal*, 91(11):4258–4272, 2006.

[40] C. W. Hollars, S. M. Lane, and T. Huser. Controlled non-classical photon emission from single conjugated polymer molecules. *Chemical Physics Letters*, 370(3–4):393–398, 2003.

[41] C. D. Hu, Y. Chinenov, and T. K. Kerppola. Visualization of interactions among bzip and rel family proteins in living cells using bimolecular fluorescence complementation. *Molecular Cell*, 9(4):789–798, 2002.

[42] A. Ichihara, T. Tanaami, K. Isozaki, Y. Sugiyama, Y. Kosugi, K. Mikuriya, M. Abe, and I. Uemura. High-speed confocal fluorescence microscopy using a nipkow scanner with microlenses for 3d-imaging of single fluorescent molecule in real time. *Bioimaging*, 4(2):52–62, 1996.

[43] E. A. Jares-Erijman and T. M. Jovin. Fret imaging. *Nature Biotechnology*, 21(11):1387–1395, 2003.

[44] R. Kasper, B. Harke, C. Forthmann, P. Tinnefeld, S. W. Hell, and M. Sauer. Single-molecule sted microscopy with photostable organic fluorophores. *Small*, 6(13):1379 – 1384, 2010.

[45] L. Kastrup, H. Blom, C. Eggeling, and S. W. Hell. Fluorescence fluctuation spectroscopy in subdiffraction focal volumes. *Physical Review Letters*, 94:178104, 2005.

[46] J. Keller. *Optimal de-excitation patterns for RESOLFT-Microscopy*. PhD thesis, University of Heidelberg, Germany, 2006.

[47] H. J. Kimble, M. Dagenais, and L. Mandel. Photon antibunching in resonance fluorescence. *Physical Review Letters*, 39(11):691–695, 1977.

[48] T. A. Klar and S. W. Hell. Subdiffraction resolution in far-field fluorescence microscopy. *Optics Letters*, 24(14):954–956, 1999.

[49] K. Kolmakov, V. Belov, J. Bierwagen, C. Ringemann, V. Müller, C. Eggeling, and S. Hell. Red-emitting rhodamine dyes for fluorescence microscopy and nanoscopy. *Chemistry: A European Journal*, 16(1):158 – 166, 2010.

[50] M. A. Lauterbach, J. Keller, A. Schönle, D. Kamin, V. Westphal, S. O. Rizzoli, and S. W. Hell. Comparing video-rate sted nanoscopy and confocal microscopy of living neurons. *Journal of Biophotonics*, 3(7):417 – 424, 2010.

[51] M. C. Leake, J. H. Chandler, G. H. Wadhams, F. Bai, R. M. Berry, and J. P. Armitage. Stoichiometry and turnover in single, functioning membrane protein complexes. *Nature*, 443(7109):355–358, 2006.

[52] M. Leutenegger, C. Eggeling, and S.W. Hell. Analytical description of sted microscopy performance. *Optics Express*, 18(25):26417–26429, 2010.

[53] M. Leutenegger, C. Ringemann, T. Lasser, S. W. Hell, and C. Eggeling. Fluorescence correlation spectroscopy with a total internal reflection fluorescence sted microscope (tirf-sted-fcs). *Optics Express*, 20(5):5243–5263, 2012.

[54] L. Li, R. R. Gattass, E. Gershgoren, H. Hwang, and J. T. Fourkas. Achieving l/20 resolution by one-color initiation and deactivation of polymerization. *Science*, 324(5929):910–913, 2009.

[55] B. Lounis and W. E. Moerner. Single photons on demand from a single molecule at room temperature. *Nature*, 407:491–493, 2000.

[56] D. Magde, W. W. Webb, and E. Elson. Thermodynamic fluctuations in a reacting system - measurement by fluorescence correlation spectroscopy. *Physical Review Letters*, 29(11):705–708, 1972.

[57] L. Mandel. Sub-poissonian photon statistics in resonance fluorescence. *Optics Letters*, 4(7):205–207, 1979.

[58] S. Manley, J. M. Gillette, G. H. Patterson, H. Shroff, H. F. Hess, E. Betzig, and J. Lippincott-Schwartz. High-density mapping of single-molecule trajectories with photoactivated localization microscopy. *Nature Methods*, 5(2):155–157, 2008.

[59] M. Mansuripur. Distribution of light at and near the focus of high-numerical-aperture objectives. *Optical Society of America. Journal A: Optics, Image Science, and Vision*, 3(12):2086–2093, 1986.

[60] E. M. McCabe, D. T. Fewer, A. C. Ottewill, S. J. Hewlett, and J. Hegarty. Direct-view microscopy: optical sectioning strength for finite-sized, multiple-pinhole arrays. *Journal of Microscopy*, 184(2):95–105, 1996.

[61] J. R. Moffitt, C. Osseforth, and J. Michaelis. Time-gating improves the spatial resolution of sted microscopy. *Optics Express*, 19(5):4242–4254, 2011.

[62] J. B. Pawley. *Handbook of biological confocal microscopy*. Springer, New York, 3rd edition, 2006.

[63] J. B. Pendry. Negative refraction makes a perfect lens. *Physical Review Letters*, 85(18):3966–3969, 2000.

[64] A. P. Ralston. *Discoverer of the Unseen World: A Biography of Antoni van Leeuwenhoek*. World Publishing Company, 1966.

[65] B. R. Rankin, R. R. Kellner, and S. W. Hell. Stimulated-emission-depletion microscopy with a multicolor stimulated-raman-scattering light source. *Optics Letters*, 33(21):2491–2493, 2008.

[66] E. H. Rego, L. Shao, J. J. Macklin, L. Winoto, G. A. Johansson, N. Kamps-Hughes, M. W. Davidson, and M. G. L. Gustafsson. Nonlinear structured-illumination microscopy with a photoswitchable protein reveals cellular structures at 50-nm resolution. *Proceedings of the National Academy of Sciences*, 109(3):E135–E143, 2012.

[67] M. Reuss. *Simpler STED setups*. PhD thesis, Universitätsbibliothek der Universität Heidelberg, 2011.

[68] M. Reuss, J. Engelhardt, and S. W. Hell. Birefringent device converts a standard scanning microscope into a sted microscope that also maps molecular orientation. *Optics Express*, 18(2):1049 – 1058, 2010.

[69] P. W. K. Rothemund. Folding dna to create nanoscale shapes and patterns. *Nature*, 440(7082):297–302, 2006.

[70] M. J. Rust, M. Bates, and X. W. Zhuang. Sub-diffraction-limit imaging by stochastic optical reconstruction microscopy (storm). *Nature Methods*, 3:793–795, 2006.

[71] S. J. Sahl, M. Leutenegger, M. Hilbert, S. W. Hell, and C. Eggeling. Fast molecular tracking maps nanoscale dynamics of plasma membrane lipids. *Proceedings of the National Academy of Sciences of the United States of America*, 107(15):6829 – 6834, 2010.

[72] B. E. A. Saleh and M. C. Teich. *Fundamentals of photonics*. John Wiley & Sons, 2 edition, 2007.

[73] O. Schwartz, J. M. Levitt, and D. Oron. Fluorescence antibunching microscopy. *Proceedings SPIE*, 8228(02), 2012.

[74] M. A. Schwentker. *Parallelized Ground State Depletion*. PhD thesis, Universitätsbibliothek der Universität Heidelberg, 2007.

[75] M. A. Schwentker, H. Bock, M. Hofmann, S. Jakobs, J. Bewersdorf, C. Eggeling, and S. W. Hell. Wide-field subdiffraction resolft microscopy using fluorescent protein photoswitching. *Microscopy Research and Technique*, 70(3):269–280, 2007.

[76] P. Schwille, F. J. MeyerAlmes, and R. Rigler. Dual-color fluorescence cross-correlation spectroscopy for multicomponent diffusional analysis in solution. *Biophysical Journal*, 72(4):1878–1886, 1997.

[77] T. F. Scott, B. A. Kowalski, A. C. Sullivan, C. N. Bowman, and R. R. McLeod. Two-color single-photon photoinitiation and photoinhibition for subdiffraction photolithography. *Science*, 324(5929):913–917, 2009.

[78] O. Shimomura, F. H. Johnson, and Y. Saiga. Extraction, purification and properties of aequorin, a bioluminescent protein from the luminous hydromedusan, aequorea. *Journal of Cellular and Comparative Physiology*, 59(3):223–239, 1962.

[79] M. C. Simon. Wollaston prism with large split angle. *Applied Optics*, 25(3):369–376, 1986.

[80] C. Steinhauer, R. Jungmann, T. Sobey, F. Simmel, and P. Tinnefeld. Dna origami as a nanoscopic ruler for super-resolution microscopy. *Angewandte Chemie International Edition*, 48(47):8870–8873, 2009.

[81] M. Suyama, Y. Kawai, S. Kimura, N. Asakura, K. Hirano, Y. Hasegawa, T. Saito, T. Morita, M. Muramatsu, and K. Yamamoto. A compact hybrid photodetector (hpd). *Nuclear Science, IEEE Transactions on*, 44(3):985–989, 1997.

[82] J. Sykora, K. Kaiser, I. Gregor, W. Bonigk, G. Schmalzing, and J. Enderlein. Exploring fluorescence antibunching in solution to determine the stoichiometry of molecular complexes. *Analytical Chemistry*, 79(11):4040–4049, 2007.

[83] H. Ta, A. Kiel, M. Wahl, and D.-P. Herten. Experimental approach to extend the range for counting fluorescent molecules based on photon-antibunching. *Physical Chemistry Chemical Physics*, 12(35), 2010.

[84] H. Ta, J. Wolfrum, and D.-P. Herten. An extended scheme for counting fluorescent molecules by photon-antibunching. *Laser Physics*, 20(1):119–124, 2010.

[85] P. Tinnefeld, C. Muller, and M. Sauer. Time-varying photon probability distribution of individual molecules at room temperature. *Chemical Physics Letters*, 345:252–258, 2001.

[86] M. H. Ulbrich and E. Y. Isacoff. Subunit counting in membrane-bound proteins. *Nature Methods*, 4(4):319–321, 2007.

[87] G. Vicidomini, G. Moneron, K. Y. Han, V. Westphal, H. Ta, M. Reuss, J. Engelhardt, C. Eggeling, and S. W. Hell. Sharper low-power sted nanoscopy by time gating. *Nature Methods*, 8(7):571 – 573, 2011.

[88] J. Vogelsang, R. Kasper, C. Steinhauer, B. Person, M. Heilemann, M. Sauer, and P. Tinnefeld. A reducing and oxidizing system minimizes photobleaching and blinking of fluorescent dyes. *Angewandte Chemie International Edition*, 47(29):5465–5469, 2008.

[89] K. D. Weston, M. Dyck, P. Tinnefeld, C. Muller, D. P. Herten, and M. Sauer. Measuring the number of independent emitters in single-molecule fluorescence images and trajectories using coincident photons. *Analytical Chemistry*, 74(20):5342–5349, 2002.

[90] V. Westphal and S. W. Hell. Nanoscale resolution in the focal plane of an optical microscope. *Physical Review Letters*, 94:143903, 2005.

[91] D. Wildanger, J. Bückers, V. Westphal, S. W. Hell, and L. Kastrup. A sted microscope aligned by design. *Optics Express*, 17(18):16100–16110, 2009.

[92] D. Wildanger, J. R. Maze, and S. W. Hell. Diffraction unlimited all-optical recording of electron spin resonances. *Physical Review Letters*, 107(1):017601, 2011.

[93] K. I. Willig, B. Harke, R. Medda, and S. W. Hell. Sted microscopy with continuous wave beams. *Nature Methods*, 4(11):915–918, 2007.

[94] S. Wischnitzer. *Introduction to electron microscopy*. Pergamon, Oxford, 1981.

[95] E. Wolf and Y. Li. Conditions for the validity of the debye integral representation of focused fields. *Optics Communications*, 39(4):205–210, 1981.

[96] H. Zhang, M. Zhao, and L. Peng. Nonlinear structured illumination microscopy by surface plasmon enhanced stimulated emission depletion. *Optics Express*, 19(24):24783–24794, 2011.

[97] X. Zhang and Z. Liu. Superlenses to overcome the diffraction limit. *Nature Materials*, 7(6):435–441, 2008.

Acknowledgements

I would like to thank all the people that supported me during my time in Heidelberg, while working at the group of *Optical Nanoscopy* and writing this thesis. First and foremost, I would like to express my gratitude to Prof. Dr. Stefan Hell for giving me the opportunity to work in his group, doing research at the forefront of optical microscopy and in an exceptional working environment. His ideas and advices were very valuable and made this work possible. I further want to thank Dr. Johann Engelhardt for supervising my work and sharing his knowledge about microscopy in all of its aspects. Special thanks also go to Thorsten Staudt, who was a great mentor at the initial stages of my doctorate, enjoyable colleague and good friend.

I want to thank my parents Bernadette and Georges Bingen, and my sister Lis for supporting me throughout these years and motivating me with their enthusiasm for my work.

Furthermore, many thanks go to Prof. Dr. Rainer Fink for agreeing to be the second referee, and to Prof. Dr. Ulrich Schwarz and Prof. Dr. Karlheinz Meier for being members of the examining board.

I thank the Luxembourg national research fund for funding me the program of *Aides à la Formation-Recherche* and allowing me to attend the American Biophysical Society Meeting in San Francisco, the Euroscience Open Forum in Torino and the Nobel Laureates Meeting in Lindau.

My stay in Heidelberg would not have been the same without my friends, who made Heidelberg a nice and fun place to live. Listed in no preferred order, I want to thank the members of my Lacrosse Team, who made me discover a great new sport, my neighbours Peter Schichtel, Vanessa Nußbaum and Manon Laviolette, my friends Anna-Lena Samm, Annemarie Hallier, Arnaud Bregnard, Katrin Thanner, Nils Müller, Peter Unger, Anne Seefeld, Christina Spassova, Alex Hentschke, Sarah Lindenmeier, Lisa Frilling, Charlotte Schwesinger, Caroline Krenkel, Peter Welinder, Jamie Hyde, Nikolaus Von Bose, and Tobias Kumpf.

A valuable addition to the work life, both in terms of scientific output as well as making work less boring and lonely, are the numerous collaborations I had the chance to be working with over the years. For this, I would like to thank :

> Anton Kurz, Single-molecule spectroscopy, BioQuant, University of Heidelberg, as well as his supervisor Dirk Herten for a fruitful collaboration on the subject of coincidence analysis,
>
> Fredrik Persson, Department of Physics, University of Gothenburg, for a tremendous international collaboration with lots of fun while measuring single strands of DNA (libegodaf!!!), as well as Joachim Fritzsche and Jonas Tegenfeldt also involved in the project,
>
> Jakub Chojnacki, Department of Infectious Diseases, Virology, University of Heidelberg, Heidelberg, Germany, for not giving up working with the dinosaur of STED microscopes, and for producing amazing results on HIV,
>
> Christian Kempf, Department of Anatomy and Cell Biology, University of Heidelberg, Heidelberg, Germany, for his hard work on the calyx of Held and allowing me to present our work at the European Biophysics conference,
>
> Yan Yu, Bading group, Department of Neurobiology IZN, University of Heidelberg, for a first successful biological application of my own setup, studying the nuclear morphology of neurons,
>
> the mechanics workshop (Wolfram Stroh and Heinrich Rühle), John Hazin, Tiho Georgiev, Margarete Poppelreuther, and Johanna Berndt.

Last but not least, I would like to thank following people for proof-reading my thesis and giving valuable input: Dorothy Guy-Ohlson, and again Johann Engelhardt, Matthias Henrich, Fredrik Persson, Peter Welinder, Thorsten Staudt and Anton Kurz. I want to especially thank Matthias Reuss for providing the nice XeLaTex template and further proof-reading.

I would finally like to mention the remaining members of my group Andy Engler, Dorothee Sauter, Eva Rittweger, Matthias Reuss, Matthias Henrich, Patrick Hoyer, Jale Schneider, Niko Dimitriadis, Franziska Curdt and Jasmin Zahn, for creating a comfortable working environment. A special thanks goes to Christoph Muus, Fanny Georgi and Weronika Kurowski, who did a great job during their short time in our group and helped me a lot.